Surface Integral Equation Methods for Multi-Scale and Wideband Problems

Dissertation

Presented in Partial Fulfillment of the Requirements for the Degree
Doctor of Philosophy in the Graduate School of
The Ohio State University

By

Jiangong Wei, B.Eng., M.S.

Graduate Program in the
Department of Electrical and Computer Engineering

The Ohio State University

2014

Dissertation Committee:

Prof. Jin-Fa Lee, Advisor

Prof. Fernando L. Teixeira

Prof. Robert Lee

© Copyright by

Jiangong Wei

2014

Abstract

This dissertation presents approaches to solve the multi-scale and wideband problems using surface integral equation methods based on the skeletonalization technique, which in essence identifies the numerically independent elements from a larger set of unknowns. In the low frequency or multi-scale scenario, overly dense mesh is generated in a global or local scale. The method is extended to composite material through the integral equation discontinuous Galerkkin method via enhanced enforcement of transmission conditions.

Conventional multi-level fast multipole method(MLFMM) faces low frequency breakdown since a large number of basis functions are concentrated within the leaf level groups, whose size is typically larger than $\lambda/4$. The computational complexity rapidly approaches that of conventional MoM, which is $O(N^2)$ for both CPU time and memory consumption for iterative solvers. In this dissertation a hierarchical multi-level fast multipole method (H-MLFMM) is proposed to accelerate the matrix-vector multiplication for low frequency and multi-scale problems. Two different types of basis functions are proposed to address these two different natures of physics corresponding to the electrical size of the elements. Moreover, the proposed H-MLFMM unifies the procedures to account for the couplings using these two distinct types of basis functions. $O(N)$ complexity is observed for both memory and CPU time from a set of numerical examples with fixed mesh sizes. Numerical results are included

to demonstrate that H-MLFMM is error controllable and robust for a wide range of applications.

On the other hand, condition number of the system matrix deteriorates due to the overly dense mesh. This would greatly affect the convergence of iterative solvers, if convergence can ever be attained. Direct solver This thesis proposes an algorithm exploits the smoothness of the far field and computes a low rank decomposition of the off-diagonal coupling blocks of the matrices through a set of skeletonalization processes. Moreover, an artificial surface (the Huygens' surface) is introduced for each clustering group to efficiently account for the couplings between well-separated groups. Furthermore, a recursive multi-level version of the algorithm is developed subsequently. Through numerical examples, we found that the proposed multi-level direct solver can scale as good as $O(N^{1.3})$ in memory consumption and $O(N^{1.8})$ in CPU time, for moderate-sized EM problems as the electrical size grows.

An novel IEDG method with enhanced enforcement of transmission conditions is proposed based on the IEDG algorithm scheme, this makes it possible to solve surface integral equation without being confined to conformal mesh and basis functions with inter-element continuity. Basis functions with different definitions and polynomial orders can be mixed flexibly to form a robust surface integral equation solver for multi-scale structures. IEDG algorithm allows local mesh refinement and greatly facilitates wideband analysis. This algorithm is then enhanced by improved enforcement of the transmission conditions, particularly for highly resonant structures. Finally, infinite ground plane effect is integrated into the algorithm for some more practical problems. Numerical results demonstrated the robustness of the algorithm.

Dedicated to the ones that I love

Acknowledgments

First I need to thank my advisor Prof. Jin-Fa Lee, for his excellent academic guidance, patience and support. His careful academic attitude in the pursue of science has enormous influence on me. I also want to thank Prof. Fernando L. Teixeira, Prof. Robert Lee and Prof. Kubilay Sertel for being the committee member for my dissertation and candidacy exam.

I am grateful to Dr. Zhen Peng for his effort and patience to help me during his stay in the group. His academic insight and meticulous attitude toward research has helped me enormously.

I also want to thank Caleb Walts for the fruitful discussions. I thank Dr. Matthew Stephenson, Dr. Xiaochuan Wang Dr. Stylianos Dosopoulos and Joshua Mahaffey for the beneficial discussion and technical matters. Throughout my time at the Electroscience Lab, I thank Jue Wang, Dongwei Li, Feiran Lei and Yuanhong Zhao for the beneficial discussion, I am immensely gratitude for their friendship.

Lastly, I want to thank my family, without whose support this work would not be possible. I thank them for their patience, tolerance and support during my Ph.D. studies.

Vita

August 19, 1983	Born - Shanxi, China
2006	B.Eng. School of Electronic Engineering, UESTC, China
2009	M.S. School of Electronic Engineering, UESTC, China
2009-present	Graduate Research Associate, The Ohio State University.

Publications

Research Publications

J.G. Wei, Z. Peng and J.F. Lee "Multi-Scale Electromagnetic Computations using a Hierarchical Multi-Level Fast Multipole Algorithm". *Radio Science*, 2014.

J.G. Wei, Z. Peng and J.F. Lee "A Fast Direct Matrix Solver for Surface Integral Equation Methods for Electromagnetic Wave Scattering from Non-penetratable Targets". *Radio Science*, 47(5), 2012.

Fields of Study

Major Field: Electrical and Computer Engineering

Table of Contents

Page

Abstract ii

Dedication iv

Acknowledgments v

Vita vi

List of Tables xi

List of Figures xii

Chapter 1. Introduction 1

1.1 Surface Integral Equation 1
1.2 Multi-scale and Low Frequency Problems 2
1.3 Sub-wavelength Breakdown 5
1.4 Previous Efforts on the Overly Dense Mesh Issue 7
1.5 Direct Solver for Integral Equation Methods 9

Chapter 2. A Fast Direct Matrix Solver for Surface Integral Equation Methods for Electromagnetic Wave Scattering from Non-penetratable Targets 12

2.1 Problem Statement 13
2.2 Theory of Direct Solver 15
2.2.1 Single-level Direct Solver 15
2.2.2 Skeletons & Skeletonalization 21
2.2.3 Multi-level Direct Solver 22
2.2.4 Skeletonalization Using A Huygen's Surface 24
2.3 Numerical Results 26
2.3.1 Sphere 26

2.3.2 Complexity and Error Studies 27
2.3.3 Machine Gun 30
2.3.4 Mock-up Aircraft 32
2.4 Conclusion 33

Chapter 3. Hierarchial Multi-level Fast Multipole Method 35

3.1 Problem Statement 37
3.2 An Overview of the Hierarchical MLFMM 38
3.3 Propagating Wave Physics 40
3.3.1 Revisit the MLFMM 40
3.3.2 Far Field Skeleton Basis for Aggregation/Disaggregation Matrix 46
3.4 Evanescent Modes Spectrum 47
3.4.1 Near Field Skeletons For Huygens' Couplings 47
3.4.2 Hierarchical Skeletonalization 50
3.4.3 Acceleration of $\mathcal{S}_{ij}$ Assembly via Adaptive Cross Approximation 51
3.4.4 Block-diagonal Pre-conditioner based on Skeletonalization Algorithm 51
3.5 Implementation of Skeletonalization Algorithm 52
3.5.1 Skeletonalization based on Huygens' Principle 53
3.6 Numerical Results 57
3.6.1 Error Controllability Study 57
3.6.2 Scalability Study 58
3.6.3 Mock-up aircraft 71
3.6.4 Circuit Board 71
3.6.5 Monopole antenna radiation problem in the presence of mock-up aircraft 72
3.7 Conclusion 78

Chapter 4. Multi-trace Integral Equation Discontinuous Galerkin Method . . 79

4.1 General Galerkin Weak Statement 81
4.1.1 Electric Field Integral Equation and Penalty Terms 82
4.1.2 Magnetic Field Integral Equation 83
4.1.3 Boundary Contour Integral Penalty Term 84
4.1.4 Galerkin Weak Formulation 85
4.2 Multi-trace IEDG for composite targets 86
4.2.1 Residual Definition 87
4.2.2 Finite Dimensional Discretization 89

4.3 Multi-trace IEDG with Enhanced Enforcement of Transmission Conditions . . . 90
4.3.1 Issues with the Enforcement of Transmission Conditions . . 91
4.3.2 Proposed Solution . . . 93
4.3.3 Numerical Results . . . 95
4.4 Multi-trace IEDG with Infinite PEC Ground Plane . . . 100
4.4.1 Boundary Value Problem . . . 100
4.4.2 Multi-trace IEDG with Infinite PEC Ground Plane . . . 102
4.5 Numerical Results . . . 103
4.5.1 Tank example . . . 103
4.5.2 Monopole Antenna . . . 104
4.5.3 NGC Wideband Antenna Array . . . 107
4.6 Conclusion . . . 112

Chapter 5. Conclusion . . . 114

Bibliography . . . 117

List of Tables

Table		Page
2.1	Computational Statistics for Fixed Mesh Size Study	29
2.2	Computational Statistics for Fixed Frequency Study	29
3.1	MVM Error	59
3.2	Computational statistics for fixed mesh size problems	60
3.3	Computational Parameters	63
3.4	Memory Statistics	65
3.5	CPU Time Statistics from 1GHz to 8GHz	65
3.6	CPU Time Statistics from 1MHz to 500MHz	66
3.7	Memory Statistics of H-MLFMM with ACA	66
3.8	CPU Statistics of H-MLFMM with ACA	67
3.9	Problem Configuration	74
3.10	S21 Results	77
3.11	Computational Statistics for Sub-domain Solvers	77
3.12	Memory requirement comparison of MLFMM and H-MLFMM	78

List of Figures

Figure		Page
1.1	Multipole antenna mounted on a mock up aircraft and a battleship .	2
1.2	Problems with drastically different mesh densities	3
1.3	Mesh with sharp triangular elements	4
1.4	Coarse mesh with inferior quality	5
2.1	Illustration of the boundary value problem	13
2.2	Partitioning of the problem geometry into 3 groups.	17
2.3	Skeletonalization	21
2.4	Multi-level Skeltonalization	23
2.5	Matrix representation of the direct solver process. Gray blocks represents matrices that are updated, dark blocks represents matrices that are not changed beyond row and column permutation.	24
2.6	Near field and far field region of group i	25
2.7	Artificial boundary of group i	26
2.8	Computed RCS of a 4 λ radius sphere compared against the Mie Series results	27
2.9	current distribution on a free-standing gun	31
2.10	current distribution of a gun mounted on a tank	32

2.11 current distribution of a mock up platform at 75MHz 33

2.12 mono-static far field pattern of a mock up platform at 75MHz, observation plane $\phi = 0^o$ 34

3.1 Propagation and evanescent wave physics 39

3.2 Matrix representation corresponding to level 1 (a), level 2 (b) and level 3 (c) binary partition of conventional MLFMM. 41

3.3 Matrix representation corresponding to level 0 (a), level 1 (b) and level 2 (c) binary paritition of H-MLFMM. 48

3.4 (a) Γ_i (red triangulations) as the support of group i and $\Gamma_{i,B}$ (green triangulations) as the support of its secondary neighbors (b) Γ_i and $\Gamma_{i,B}$ with the Huygens' surface Γ_a (blue triangulations) (c) Γ_i and Γ_a only 55

3.5 Part of a mock-up aircraft 59

3.6 Complexity of memory consumption for fixed mesh size problems . . 60

3.7 Complexity of CPU time for fixed mesh size problems 61

3.8 Front, top and bottom view of central fuselage part of an aircraft model 62

3.9 Complexity comparison of memory consumption, H-MLFMM vs. MLFMM. 1MHz–1GHz, N is constant. 1GHz– 8GHz, $N \propto f$ 64

3.10 Complexity comparison of CPU time per MVM, H-MLFMM vs. MLFMM. 1MHz–1GHz, N is constant. 1GHz – 8GHz, $N \propto f$ 64

3.11 Far field of H-MLFMM vs. MLFMM on $\phi = 0^o$ plane at 1000MHz . . 68

3.12 Real part of current at 1GHz (a)H-MLFMM (b)MLFMM 68

3.13 Far field of H-MLFMM vs. MLFMM on $\phi = 0^o$ plane at 8000MHz . . 68

3.14 Real part of current at 8GHz (a)H-MLFMM (b)MLFMM 69

3.15 Far field of H-MLFMM vs. MLFMM on $\phi = 0^o$ plane at 125MHz . . 69

3.16 Real part of current at 125MHz (a)H-MLFMM (b)MLFMM 69

3.17 Far field comparison of $hk = 0.003\pi$ using H-MLFMM and $hk = 0.01\pi$ using MLFMM on $\phi = 0^o$ plane at 15MHz 70

3.18 Imaginary part of current at 15MHz (a)$hk = 0.01\pi$ (b)$hk = 0.003\pi$. 70

3.19 A zoom-in view of Figure.3.18(b) 71

3.20 Real part of the electric current on a mock-up aircraft at 0.5MHz . . 72

3.21 Real part of the electric current on a circuit board at 10GHz in logarithmic scale 73

3.22 Mock-up aircraft partition 75

3.23 Real part of current for EMC simulation at 75MHz in log scale 75

3.24 Real part of current for EMC simulation at 75MHz in log scale 76

3.25 Real part of current for EMC simulation at 75MHz in log scale 76

4.1 Illustration of the boundary value problem 81

4.2 An electromagnetic scattering problem from composite targets 86

4.3 Error j and m on dielectric interface using $j_m^{\pm} = span\{\lambda'\}$ and $m_m^{\pm} = span\{\lambda'\}$ 90

4.4 Real part of magnetic current along the PEC-dielectric interface . . . 91

4.5 Current pattern of λ_0' 92

4.6 Error j and m on dielectric interface using $j_m^{\pm} = span\{\lambda'\}$ and $m_m^{\pm} = span\{\hat{n}^{\pm} \times \lambda'\}$ 93

4.7 Far field comparison with MIE series 94

4.8 Far field comparison against MIE series 96

4.9 Error j and m on dielectric interface using $j_m^{\pm} = span\{LB \times \hat{n}_m^{\pm}\}$ and $m_m^{\pm} = span\{LB\}$ 97

4.10 Geometry of a small slot example 97

4.11 Far field comparison of the small slot example 98

4.12 Error j and m in slot using $j_m^{\pm} = span\{\lambda'\}$ and $m_m^{\pm} = span\{\lambda'\}$ . . . 99

4.13 Error j and m in slot using $j_m^{\pm} = span\{LB \times \hat{n}_m^{\pm}\}$ and $m_m^{\pm} = span\{LB\}$ 99

4.14 Illustration of the boundary value problem with infinite PEC ground plane 100

4.15 Illustration of the updated boundary value problem with infinite PEC ground plane 101

4.16 Illustration of the problem with part of the geometry below the infinite PEC ground plane 103

4.17 Illustration of the equivalent problem with part of the geometry below the infinite PEC ground plane 103

4.18 Total far field electric field result for the tank example with and without infinite PEC ground plane 104

4.19 Top view of the real part of the electric current on a free standing tank without infinite PEC ground plane 105

4.20 Bottom view of the real part of the electric current on a free standing tank without infinite PEC ground plane 105

4.21 Top view of the real part of the electric current on a tank in the presence of the infinite PEC ground plane 106

4.22 Bottom view of the real part of the electric current on a tank in the presence of the infinite PEC ground plane 106

4.23 Radiation pattern for the monopole antenna with and without infinite PEC ground plane 107

4.24 Top view of the real part of the electric current on the free standing monopole antenna 108

4.25 Top view of the real part of the electric current on the monopole antenna mounted on infinite PEC ground 108

4.26 NGC 8x8 antenna array 109

4.27 S_{11} distribution of NGC 8x8 antenna array scanning 60^o toward positive Y direction 110

4.28 3D far field of theta polarization, NGC 8x8 antenna array scanning 60^o toward positive Y direction 110

4.29 Far field of theta polarization on E plane, NGC 8x8 antenna array scanning 60^o toward positive Y direction 111

4.30 Comparison of normalized far field on E plane with measurement, NGC 8x8 antenna array scanning 60^o toward positive Y direction 111

4.31 Comparison of far field on E plane with finite ground plane, NGC 8x8 antenna array scanning 60^o toward positive Y direction 112

Chapter 1: Introduction

1.1 Surface Integral Equation

Surface integral equation (SIE) methods have been widely employed to solve electromagnetic wave scattering and radiation problems. Particularly, they are most effective in dealing with electromagnetic (EM) wave radiation and scattering in the presence of non-penetrable and homogeneous or stratified targets. It is mainly due to the fact that only the surface of the target needs to be discretized, and subsequently requiring much less number of unknowns by orders of magnitude compared to the volume discretization counterparts. Additionally, in recent years, we have witnessed quite a few *fast* integral equation methods developed and successfully applied to reduce the computational resources needed for computations involving electrically large structures. Among them, we mention the adaptive integral method (AIM) [1], and the multi-level fast multipole method (MLFMM) [2]. Above all, the MLFMM is arguably the most successful and most widely embraced for addressing electrically large EM problems [3] [4]. However, conventional MLFMM encounters great difficulty addressing the multi-scale and low frequency problems efficiently, even for problems with moderate number of DoFs.

1.2 Multi-scale and Low Frequency Problems

Integral equation methods usually discretize the geometries into piecewise elements whose size is typically 0.1λ. Trial functions are later on assigned to these elements to represent the electric and magnetic sources that resides on. Testing functions are selected, typically from the dual space of the trial functions, and matrix equations can be established from numerical procedures, e.g., method of moment[5].

Real-life simulations involves calculation of complicated structures across a wide band spectrum as demonstrated by Figure.1.1. While the mesh size is dependent on the calculating frequency, the physical configuration of the geometry is not. For the components that contain intricate structures such as antennas and microwave instruments, dense meshes have to be adopted to maintain the integrity of the geometry, regardless of the frequency of interest. Consequently, large number of unknowns may resides within certain leaf level groups from conventional multi-level fast multipole method (MLFMM) and this would lead rapid increase of computation complexity in terms of both memory and CPU consumption, destroying the $O(NlogN)$ complexity.

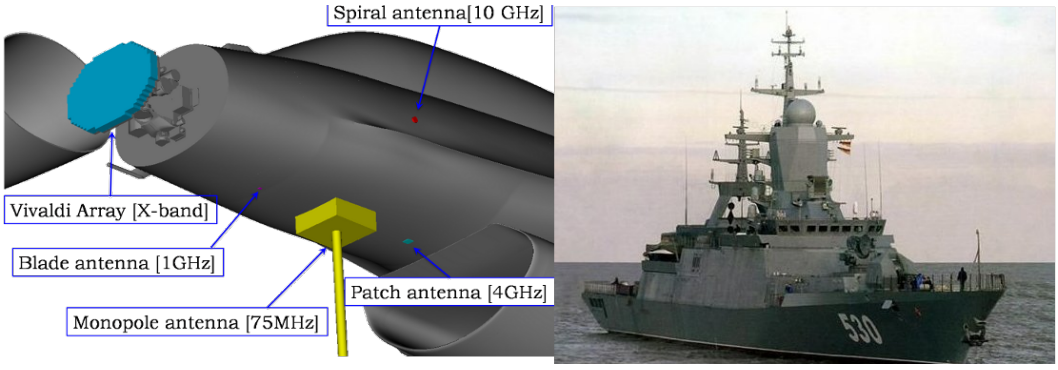

Figure 1.1: Multipole antenna mounted on a mock up aircraft and a battleship

Moreover, practical antennas are almost always mounted on certain platforms such as the fuselage of aircraft, which could be smooth and contain less geometry details as shown in Figure.1.1. In this figure, the smooth forward fuselage of the aircraft are meshed using 0.1λ at 3GHz while the spiral antenna is discretized using 0.015λ to maintain its geometry. Compared with the antennas, coarser meshes can be applied to these platforms to help reduce the total number of unknowns. These mesh densities that range across several orders pose the so-called "multi-scale" problem. It results in system matrices with deteriorated condition number, especially for the electric field integral equation(EFIE)[6]. Not only does this poses serious challenges for iterative solvers such as Krylov methods, it jeopardizes the accuracy of results from direct solvers as well [7].

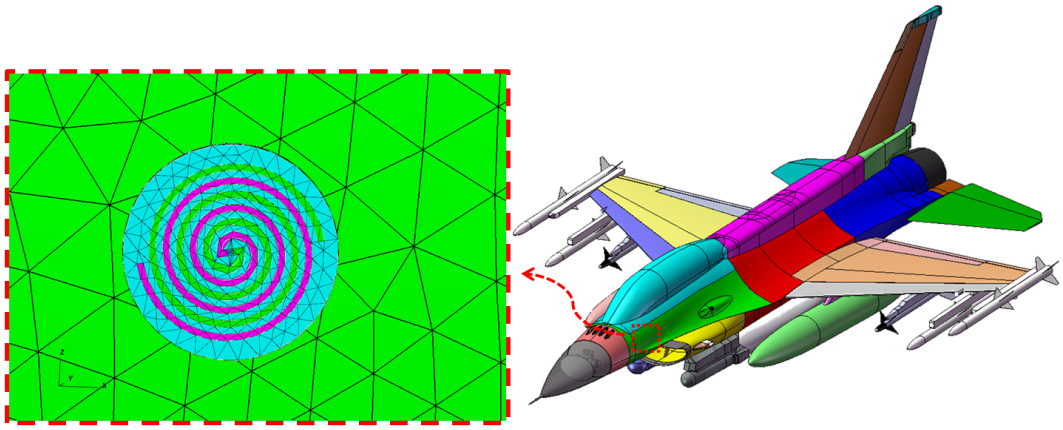

Figure 1.2: Problems with drastically different mesh densities

On the other hand, frequency responses from a wide spectrum range are usually desired for imaging purpose, etc.. One conventional approach divides the spectrum range into several frequency sections and discretizes the object for each particular

section. This helps to keep the computational complexity under control across the whole spectrum by limiting the number of DoFs within each 0.25λ sized group. However, generation of mesh with high fidelity from complicated geometry poses another practical challenge. Poor quality meshes with ill shaped elements, e.g. sharp triangulation shown in Figure.1.3, lead to escalation of numerical dependency among basis functions. Consequently, they jeopardize the condition number of the system matrices and result in inferior convergence or even non-physical results. Intense human intervention is usually required to maintain the quality of the mesh and thus making this process tedious and laborious. To make it worse, this difficulty is compounded when the responses from a wide frequency spectrum are desired, which requires a set of mesh for each frequency band of interest.

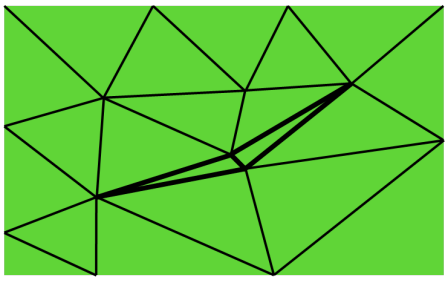

Figure 1.3: Mesh with sharp triangular elements

Another type of difficulty arises if the conventional 0.1λ mesh density cannot discretize the object without jeopardizing the integrity of the geometry. For instance, mesh size of $0.5m$ are supposed to be adopted at 60MHz to discretize the object based on the conventional requirement, consequently a $1m$ radius sphere would be discretized as shown in Figure.1.4a. Also, large amount of singular shaped elements

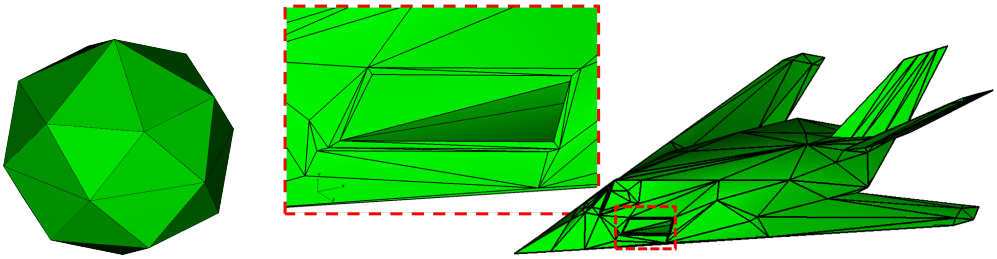

(a) Sphere (b) Mock-up aircraft

Figure 1.4: Coarse mesh with inferior quality

could be generated and cause the condition number of the system matrix to deteriorate severely. Take a mock-up aircraft geometry for example, it contains large smooth facets as well as certain detail structures, naive implementation of 0.1λ mesh size at 5MHz would result in a discretization shown in Figure.1.4b.

One potential solution to the two issues aforementioned is to recycle the mesh at higher frequencies for the calculation of lower frequencies. Human intervention can thus be reduced drastically and the mesh at higher frequencies is generally better in preserving the geometry as well. However, conventional MLFMM encounters the "sub-wavelength breakdown" since the mesh generated at higher frequencies would be overly dense for the calculation at lower frequencies. Consequently, the computational complexity escalates rapidly from $O(NlogN)$ towards $O(N^2)$ in terms of both CPU time and memory consumption, rendering conventional MLFMM inefficient in these scenarios.

1.3 Sub-wavelength Breakdown

Conventional MLFMM relies on the plane wave basis to accelerate matrix-vector product. It starts by partitioning the DoFs into a hierarchical set of groups until the

leaf level group is no less than 0.25λ [8][9]. Assume DoF i from group m and DoF j from group m' reside in each others far-region or secondary neighbors, the coupling between them can be expanded as follows [8],

$$\mathbf{Z}_{ij} = \left(\frac{k}{4\pi}\right)^2 \oint \mathbf{V}_{im}^{rev} \cdot T_{mm'}(\hat{k} \cdot \hat{r}_{mm'}) \cdot \mathbf{V}_{m'j}^{rad} d^2\hat{k} \tag{1.1}$$

where k is the wave propagation constant, $\mathbf{V}_{im}^{rev}$ is the aggregation matrix that serves as a radiation pattern. It projects the DoFs into plane wave basis. $\mathbf{V}_{m'j}^{rad}$ is the disaggregation matrix that maps the plane wave basis back to the original DoFs, it can be interpreted as a receiving pattern. $T_{1mm'}(\hat{k} \cdot \hat{r}_{mm'})$ is the translator and it is defined as,

$$T_{mm'}(\hat{k} \cdot \hat{r}_{mm'}) = \sum_{l=0}^{L} (-j)^l (2l+1) h_l^{(2)}(k \cdot r_{mm'}) P_l(\hat{r}_{mm'} \cdot \hat{k}) \tag{1.2}$$

where $h_l^{(2)}$ denotes the spherical Hankel functions of the second kind, P_l is the Legendre polynomial of degree l and L is the number of multipole expansion terms. The coupling between groups that reside in the near field region are accounted for through conventional MoM representation.

The near field complexity of MLFMM is expected to scale as $O(N)$ since the number of DoFs per leaf level group is less than a constant assuming conventional mesh density is adopted. Sub-wavelength breakdown issue emerges when the mesh is overly dense, either in a local scale in the multi-scale scenario shown in Figure.1.2 or in a global scale. In both cases, large number of DoFs still reside in certain leaf level groups since the size of the finest group cannot be less than 0.25λ [8]. Mathematically, this is due to the reason that the arguments of the spherical Hankel functions appearing in the translator expression equation(1.2) are very small. Due to the asymptotic

behaviors of the spherical Hankel functions with small arguments, the multipole amplitudes of the spherical waves are very singular. , i.e., they are either very large or very small at any level, resulting in large errors in equation(1.2)[10][11]. The expansion equation(1.1) is useless if the error aforementioned is not suppressed since the values of the elements in the translator can easily yield floating-point overflows and halting the computation. Consequently, the accumulation of DoFs in the leaf level groups leads to rapid escalation of near field complexity towards $O(N^2)$.

1.4 Previous Efforts on the Overly Dense Mesh Issue

A number of approaches have been attempted to tackle the dense mesh issue. One category of the methods utilize different formulations to expand the couplings between groups smaller than $\lambda/4$. In [10], Zhao and Chew introduced scaling factors to smooth the transition from Helmholtz FMM down to Laplace FMM. It assumes that the multipoles required at very low frequencies ($k \to 0$) for small structures ($k \cdot d \to 0$) are almost constant and one can afford to adopt an undiagonalized alternative of the translation operator. k is adopted as a normalized factor and the small argument approximation of the Hankel function constitutes the new undiagonalized translator. This new type of expansion allows further partition of the groups and this helps to brings the near field complexity under control once again. This methodology focuses on the extremely low frequencies approaching quasistatic spectrum, e.g. $h/\lambda < 1.e-6$ and extremely small structures such as circuits, etc., it is cumbersome for the scenario where h is between the range of conventional 0.1λ and quasistatic. However, it was pointed out that this approach is not suitable for problems with discretization sizes across multiple orders, i.e., multiscale problems[12]. This is due to the reason that a

connection between the two types of expansion adopted in the quasistatic region and radiation region is yet to be established, excluding the possibility of a non-uniform oct-tree[12] ,which allows the number of DoFs per level group to be approximately the same.

Another work conducted in [12] named accelerate Cartesian expansion (ACE) employed the Cartesian harmonics for multipole and local expansions for levels beneath the MLFMM leafs. ACE allows partitioning the DoFs into a non-uniform oct-tree such that the number of DoFs per each leaf cube at various level is approximately constant. A mapping procedure can be performed between accelerated Cartesian expansion and fast multipole expansion to accomplish the integration with the expansion adopted in equation(1.1). Mathematically, ACE mainly utilizes Taylor expansion of the MLFMM multipoles[12]. However, unlike the conventional MLFMM which establishes a close connection between the mathematics and the physics, ACE is still yet to suggest a physical interpretation of its mathematics, e.g. the relationship between the Cartesian basis and the underlying physics it is representing. Reference [13] expresses the spectral Green's function in terms of evanescent plane wave and propagating plane wave. It is applicable for both spatial and frequency scalings, however, an infinite integral has to be evaluated in the k-space.

The second category of the fast methods focuses on exploiting the rank deficiency property of the interaction matrices between two over populated groups. The kernel independent adaptive cross approximation (ACA) technique [14] belongs to this category. It decomposes the dense interaction between two well-separated groups, through simply applying algebraic maneuver, into the multiplications of two reduced dimension dense matrices. A hierarchical version of the ACA algorithm was introduced in

[15] to further reduce the computational resources. Nevertheless, the error controllability for the ACA algorithms remains yet elusive. Some other matrix compression methods include, but not limited to, the compressed block decomposition (CBD) [16], matrix decomposition algorithm (MDA) [17], etc.. Fast direct solver algorithms have been developed on top of these data sparsification techniques [18]. These fast methods based on data sparsification algorithms accomplish high efficiency for densely meshed problems of small or moderate electrical size, however, their efficiency for problems of large electrical size is yet to be comparable with that of MLFMM. This is mainly due to the reason that while these data sparsification algorithm can effectively represent the evanescent phenomenon in the near field, conventional MLFMM is more efficient to represent the propagation phenomenon.

The aforementioned methods seek alternative representations of the interaction process between a pair of groups and compress the coupling matrices in a pairwise manner. On the other hand, the skeletonalization algorithm proposed in [19] utilizes a low rank decomposition of the off-diagonal coupling blocks of the dense matrices using a single reduced set of the original DoFs for each group. This set of DoFs is named as skeletons since they are capable of representing all the interactions between this group and the other groups that are well separated from it.

1.5 Direct Solver for Integral Equation Methods

Although in recent years, we have witnessed significant advancements of fast integral equation methods, most of them mainly address the issue of speed-up the matrix-vector multiplications. Nonetheless, the overall success still relies on the availability of a robust and effective preconditioner for the integral equation methods. Even

though, there are many substantial developments in this regard [20], the existence of a preconditioner that guarantees the convergence in the iterative matrix solution process remains largely elusive. Direct solvers for integral equation methods are another important and interesting branch, they are sometimes favored compared to their iterative counterparts, especially in solving ill-conditioned matrices that may seriously challenge iterative solvers. Moreover, they often exhibit high efficiency in multiple right-hand-sides (RHSs) owing to the small constant in front of the complexity asymptotic when dealing with small or moderate electrical size problems. However, the conventional direct solver, based on the LU factorization, scales as $O(N^2)$, $O(N^3)$ for memory consumption and the factorization time, respectively. The inherent high complexities of the conventional LU direct solvers severely limit their application to solve practical EM problems. To circumvent these difficulties, in recent years, several fast direct solvers have been proposed in the literature. In reference [18], the author reported solving an one-million unknown problem using Multi-level Adaptive Cross Approximation (ML-ACA) algorithm. Also, in reference [7], a local-global solution method separates the radiating current from the non-radiating counterpart and reported to achieve $O(N^{1.3})$ complexity in terms of memory consumption for electrically large problems. Additionally, reference [21] discussed a compressed block decomposition (CBD) method and demonstrated a complexity of $O(N^{1.5})$ for the memory consumption. Another work conducted in [22] and [23] adopt the non-uniform grid (NG) based matrix compression method, it introduces a non-redundant coarse spherical non-uniform sampling grid to effectively skeletonalize the coupling process and compress the matrix using Schur's complement. [24] claimed to find the $\mathcal{H}^2$ representation of the inverse of the dense matrix in an error-controllable manner and reported

a linear complexity both in terms of CPU time and memory consumption. However, we disagree with the complexity analyses presented in [24] and remain unconvinced of the performance reported. One of the recently published works, [25] shares some similarities with the proposed algorithm in this dissertation. It also seeks for a unique mapping matrix for each group to represent the coupling.

We propose in this dissertation a fast direct solver, based on the algorithm outlined in [26], [19], is presented to solve matrix equations from 3D SIE methods for electrodynamic applications. This algorithm utilizes a low rank decomposition of the off-diagonal coupling blocks of the dense matrices [27]. Moreover, a multi-level version in-conjunction with a Huygen's surface to account for couplings between well-separated groups is also discussed in detail. Although, we believe that the algorithm will not alter the complexities of matrix solutions in SIEs in the worst case scenario for electrically large problems, $O(N^2)$ and $O(N^3)$ for memory and CPU time, the proposed algorithm can be fast and efficient for many practical numerical examples. Particularly, during the process of $h-refinement$, where the discretization size decreases to improve the accuracy, the complexities observed are $O(N)$ and $(N^{1.5})$ for memory and CPU time, respectively. The reported complexities agree well with the theoretical predictions in [19] for smooth integral kernels on general two-dimensional surfaces. A few numerical results are included to validate the algorithm. Additionally, numerical experiments are conducted for fixed mesh size, while the frequency increases, as well as for fixed frequency, while the mesh size decreases (the h-refinement).

Chapter 2: A Fast Direct Matrix Solver for Surface Integral Equation Methods for Electromagnetic Wave Scattering from Non-penetratable Targets

The implementation details of a fast direct solver is described herein for solving dense matrix equations from the application of surface integral equation methods for electromagnetic field scatterings from non-penetrable targets. The proposed algorithm exploits the smoothness of the far field and computes a low rank decomposition of the off-diagonal coupling blocks of the matrices through a set of skeletonalization processes. Moreover, an artificial surface (the Huygens' surface) is introduced for each clustering group to efficiently account for the couplings between well-separated groups. Furthermore, a recursive multi-level version of the algorithm has also been presented. Although asymptotically the algorithm would not alter the bleak outlook of the complexity of the worst case scenario, $O(N^3)$ for required CPU time with N denotes the number of unknowns, for electrically large electromagnetic (EM) problems; through numerical examples, we found that the proposed multi-level direct solver can scale as good as $O(N^{1.3})$ in memory consumption and $O(N^{1.8})$ in CPU time, for moderate-sized EM problems as the electrical size grows. Note that, our conclusions are drawn based on a few sample examples that we have conducted, and should not be taken as a true complexity analysis for general electrodynamic applications.

However, for the fixed frequency (*h-refinement*) scenario, where the discretization size decreases, the computational complexity observed agree well with the theoretical predictions. Namely, the algorithm exhibits $O(N)$ and $O(N^{1.5})$ complexities for memory consumption and CPU time, respectively.

2.1 Problem Statement

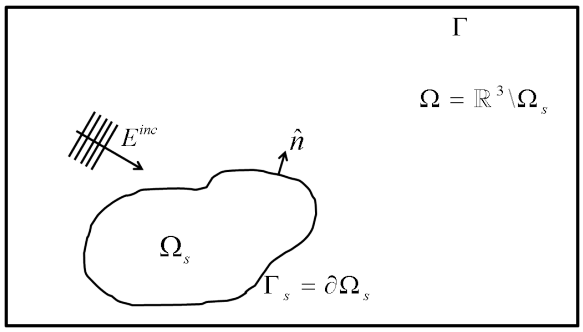

Figure 2.1: Illustration of the boundary value problem

For electromagnetic wave scattering from a non-penetrable target, we have the following boundary value problem statement. (with the factor $e^{i\omega t}$ suppressed, $i = \sqrt{-1}$)

$$\begin{cases} \nabla \times \nabla \times \mathbf{E} - k^2 \mathbf{E} = 0 & in \ \ \Omega \\ \hat{\mathbf{n}} \times \mathbf{E} = 0 & on \ \Gamma_s \\ \lim_{|\mathbf{r}| \rightharpoonup \infty} |\mathbf{r}| (\nabla \times \mathbf{E}^{sca} + ik\hat{\mathbf{r}} \times \mathbf{E}^{sca}) = 0 \end{cases} \tag{2.1}$$

As illustrated in Figure.2.1, an incident plane wave $\mathbf{E}^{inc}$ impinges on the boundary Γ_s of a PEC object Ω_s. The complement of the scatter is denoted by $\Omega \, (= \mathbb{R}^3 \setminus \Omega_s)$ and Γ_s is the bounding surface of Ω_s. The wavenumber is denoted by $k = \omega\sqrt{\mu_0 \varepsilon_0}$, with μ_0 and ε_0 being the permeability and the permittivity of the free space, respectively.

Subsequently, we have the following boundary condition to be satisfied:

$$\pi_t \mathbf{E} = 0 \qquad on\ \Gamma_s \tag{2.2}$$

where π_t denotes the tangential trace operator on the surface and it is defined as $\pi_t \mathbf{u} = \hat{\mathbf{n}} \times \mathbf{u} \times \hat{\mathbf{n}}$. Expanding the total field, $\mathbf{E} = \mathbf{E}^{inc} + \mathbf{E}^{sca}$, we have

$$-\pi_t \mathbf{E}^{inc} = \pi_t \mathbf{E}^{sca} \qquad on\ \Gamma_s \tag{2.3}$$

Moreover, both the electric $\mathbf{E}$ and the magnetic $\mathbf{H}$ fields in the exterior region, Ω, can be obtained through the Stratton-Chu representation formulae in terms of the surface electric current density, $\mathbf{J} = (\hat{\mathbf{n}} \times \mathbf{H}) \in \mathbf{H}^{-1/2}\left(div_\Gamma; \Gamma_s\right)$. Consequently, we write the electric field integral equation (EFIE) as:

$$\pi_t \mathbf{E}^{inc}(\mathbf{x}) = -\pi_t L(\mathbf{J})(\mathbf{x}) \qquad on\ \Gamma_s \tag{2.4}$$

where $L(\mathbf{J})(\mathbf{x}) = -\imath k\eta \int_{\Gamma_s} [\bar{\bar{\mathbf{I}}} + \frac{1}{k^2} \bigtriangledown_\Gamma^{(x)} \bigtriangledown_\Gamma^{(x)} \cdot] G(\mathbf{x},\mathbf{y}) \mathbf{J}(\mathbf{y}) d\mathbf{y}$. Note that, we denote $\bigtriangledown_\Gamma^{(x)}$ and $\bigtriangledown_\Gamma^{(y)}$ as the surface gradient operators operate on the observation and the source coordinates, respectively.

Magnetic field integral equation (MFIE) can also be derived for closed surface targets as:

$$\pi^{\times} \mathbf{H}^{inc} = \frac{1}{2}\mathbf{J} + K(\mathbf{J})(\mathbf{x}) \tag{2.5}$$

where $K(\mathbf{J})(\mathbf{x}) = -\hat{\mathbf{n}} \times p.v. \int_{\Gamma_s} \bigtriangledown_\Gamma^{(x)} G(\mathbf{x},\mathbf{y}) \times \mathbf{J}(\mathbf{y}) d\mathbf{y}$, $p.v.$ stands for principle value, $\pi^{\times}\mathbf{u} = \hat{\mathbf{n}} \times \mathbf{u}$ and $G(\mathbf{x},\mathbf{y}) = \frac{e^{-ik|\mathbf{x}-\mathbf{y}|}}{|\mathbf{x}-\mathbf{y}|}$ is the Green's function in free space. Note that the MFIE formulation, equation (3.5), is only applicable for closed-surfaced non-penetrable targets.

The combined field integral equation (CFIE) combines the EFIE and the MFIE to yield:

$$\alpha\pi_t\mathbf{E}^{inc} + (1-\alpha)\eta\pi^{\times}\mathbf{H}^{inc} = \frac{1-\alpha}{2}\eta\mathbf{J} - \alpha(\pi_t L(\mathbf{J})(\mathbf{x})) + (1-\alpha)\eta K(\mathbf{J})(\mathbf{x}) \quad (2.6)$$

where $\eta = \sqrt{\mu_0/\varepsilon_0}$ is the free space intrinsic impedance. The CFIE formulation mitigates the notorious internal resonances by treating Γ_s as an impedance surface [28], and thus renders the resonance frequencies complex so long as $\Re\alpha \neq 0$.

2.2 Theory of Direct Solver

2.2.1 Single-level Direct Solver

The fast algorithms of direct solution of integral equations are usually developed by exploiting the redundancy in the couplings between well-separated groups. This is mainly due to the fact that the discretization size employed in the SIEs is usually much higher than the Nyquist sampling rate in order to capture the near-field evanescent-mode phenomena. However, discretization thus employed will often be an overkill for computing the radiation between well-separated groups. Subsequently, this redundancy would manifest as the rank deficiency in the off-diagonal matrix blocks. Herein, we seek the inverse of the system matrix through exploitation of the rank deficiency of the coupling matrices hierarchically, both in terms of geometry partitions and matrix operations.

For the application of method of moments, one first discretizes the problem geometry, followed by choosing proper basis functions (commonly Rao-Wilton-Glisson (RWG) basis functions [29]), to span the unknown surface electric current density $\mathbf{J}$. Explicitly, we write $\mathbf{J} \approx \sum_{i=1}^{N} c_i\lambda_i$ with λ_i denotes i^{th} RWG basis function. In order

to take advantage of the rank deficiency of the couplings, a hierarchical decomposition of the original geometry would be desirable. For problems in 3D, a hierarchical oct-tree would be constructed and the RWG basis functions are sorted into separate boxes from each level of the oct-tree according to their coordinates. The oct-tree partitioning continues until the smallest boxes include no more than 100 unknowns. Subsequently, the RWG basis functions would be reordered such that the first n_1 unknowns belongs to the box number 1, the second n_2 unknowns belongs to box number 2, etc. By testing the EFIE and MFIE with proper testing functions [30], we obtain a dense linear matrix equation $Ax = b$. To assist our discussions, we assume that the unknowns are partitioned into three groups, see Figure.2.2. As a consequence, the impedance matrix can be written accordingly as:

$$\begin{pmatrix} A_{11} & A_{12} & A_{13} \\ A_{21} & A_{22} & A_{23} \\ A_{31} & A_{32} & A_{33} \end{pmatrix} \cdot \begin{pmatrix} x_1 \\ x_2 \\ x_3 \end{pmatrix} = \begin{pmatrix} b_1 \\ b_2 \\ b_3 \end{pmatrix} \tag{2.7}$$

where A_{ij} denotes the coupling matrix between box i and box j, x_i denotes the coefficients of the basis functions in box i while b_i represents the right hand sides vector of box i. Assuming the off-diagonal sub-matrices, $A_{ij}, i \neq j$, are low rank and, subsequently, can be decomposed as (with $k_i < n_i$, $k_j < n_j$):

$$A_{ij}^{n_i \times n_j} \approx L_i^{n_i \times k_i} S_{ij}^{k_i \times k_j} R_j^{k_j \times n_j} \tag{2.8}$$

where n_i, n_j are the numbers of unknowns and k_i, k_j are the effective ranks in box i and box j, respectively. This decomposition [26] proves beneficial since L_i and R_j associate only with boxes i and j. Unlike other data-sparse-representation techniques such as ACA, which generates separate low rank decomposition for each distinct coupling pair, the L_i matrix produced herein by the proposed skeletonalization process can be shared by $A_{ij}, \forall j \neq i$. Yet another interesting characteristic of equation(3.22) is that

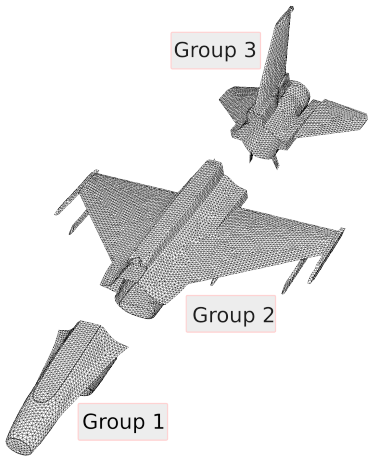

Figure 2.2: Partitioning of the problem geometry into 3 groups.

the entries of S_{ij} are comprised of the original entries of A_{ij}. The reduced set of basis functions employed for S_{ij} are thus named "skeletons".

To obtain the decomposition in equation(3.22) for block i, we concatenate all the A_{ij} sub-matrices or A_{ij}^T sub matrices with $i \neq j$:

$$A_i^L = \begin{bmatrix} A_{i1} & A_{i2} & \cdots & A_{iN_j} \end{bmatrix}^{n_i \times (N_{tot} - n_i)}, \tag{2.9}$$

$$A_i^R = \begin{bmatrix} A_{1i}^T & A_{2i}^T & \cdots & A_{N_j i}^T \end{bmatrix}^{n_i \times (N_{tot} - n_i)} \tag{2.10}$$

where N_{tot} is the total number of DoFs of the problem and N_j is the number of geometrical partitions in the current level. Following the approach proposed in [27], which involves a column pivoted QR decomposition, we perform the desired decompositions of A_i^L and A_i^R. Subsequently, the matrices L_i and R_i can be computed separately and, accordingly, the incoming (receiving) and the outgoing (radiating) skeletons. Namely, for each of the groups, there would be two skeletons responsible for radiating and receiving operations, respectively. However, an alternative enables us to consolidate

the L and R matrices, through concatenating all A_{ij} and A_{ij}^T sub-matrices. We write:

$$A_i = \left[\begin{array}{cc} A_i^L & A_i^R \end{array} \right] = \left[\begin{array}{ccccccc} A_{i1} & A_{i2} & \cdots & A_{1i}^T & A_{2i}^T & \cdots \end{array} \right]^{n_i \times 2(N_{tot}-n_i)} \tag{2.11}$$

When decomposing the matrix A_i in equation (3.23), it can be shown:

$$L_i = R_i^T \tag{2.12}$$

As a consequence, only one QR decomposition needs to be performed for each of the groups. Specifically, we have:

$$A_i^T P_R \approx Q \left[\begin{array}{cc} R_{11} & R_{12} \end{array} \right] \tag{2.13}$$

where P_R is the permutation matrix generated during the QR decomposition process. Moreover, we note that $P_R^T = P_R^{-1}$. The numerical rank k_i would be determined from the diagonal entries of $R = [R_{11}\ R_{12}]$ matrix.

Denote $R_{11}T = R_{12}$, and we have:

$$A_i \approx P_R \left[\begin{array}{c} I \\ \\ T^T \end{array} \right] A_{RS} \tag{2.14}$$

where I is the $k_i \times k_i$ identity matrix. A_{RS} is the first k_i rows of $P_R^T A_i$. Consequently, the first k_i rows of the permutated A_i matrix are the skeleton indices while the rest of the $(n_i - k_i)$ rows are linear combinations of the k_i skeletons and the coefficients are stored in T^T matrix. After the QR decomposition, the L_i matrix is readily available:

$$L_i = P_R \left[\begin{array}{c} I \\ \\ T^T \end{array} \right] \tag{2.15}$$

It is worth pointing out that the skeletonalization process could be highly parallelized.

With the mappings L_i computed, the matrix equation (2.7) can be rewritten as:

$$\begin{pmatrix} A_{11} & 0 & 0 \\ 0 & A_{22} & 0 \\ 0 & 0 & A_{33} \end{pmatrix} \cdot \begin{pmatrix} x_1 \\ x_2 \\ x_3 \end{pmatrix}^{N\times 1} + \begin{pmatrix} 0 & L_1S_{12} & L_1S_{13} \\ L_2S_{21} & 0 & L_2S_{23} \\ L_3S_{31} & L_3S_{32} & 0 \end{pmatrix} \cdot \begin{pmatrix} y_1 \\ y_2 \\ y_3 \end{pmatrix}^{N_{k(1)}\times 1} \approx \begin{pmatrix} b_1 \\ b_2 \\ b_3 \end{pmatrix} \tag{2.16}$$

with $y_j = L_j^T x_j$. From equation(2.16), it is obvious that the solution of the original problem, x, can be expressed in terms of the new y vector with much reduced dimension $N_{k(1)}$ (if the effective ranks are much smaller than the number of unknowns in each block). Written explicitly, we have

$$\begin{pmatrix} x_1 \\ x_2 \\ x_3 \end{pmatrix} \approx \begin{pmatrix} A_{11} & 0 & 0 \\ 0 & A_{22} & 0 \\ 0 & 0 & A_{33} \end{pmatrix}^{-1} \cdot \left(\begin{pmatrix} b_1 \\ b_2 \\ b_3 \end{pmatrix} - \begin{pmatrix} 0 & L_1S_{12} & L_1S_{13} \\ L_2S_{21} & 0 & L_2S_{23} \\ L_3S_{31} & L_3S_{32} & 0 \end{pmatrix} \cdot \begin{pmatrix} y_1 \\ y_2 \\ y_3 \end{pmatrix} \right) \tag{2.17}$$

Evidently, the computation of the solution vector, x, hinges on our ability to compute y. To do so, we shall rewrite equation(2.16) into:

$$\begin{pmatrix} A_{11} & 0 & 0 & 0 & L_1S_{12} & L_1S_{13} \\ 0 & A_{22} & 0 & L_2S_{21} & 0 & L_2S_{23} \\ 0 & 0 & A_{33} & L_3S_{31} & L_3S_{32} & 0 \\ L_1^T & 0 & 0 & -I_1 & 0 & 0 \\ 0 & L_2^T & 0 & 0 & -I_2 & 0 \\ 0 & 0 & L_3^T & 0 & 0 & -I_3 \end{pmatrix} \cdot \begin{pmatrix} x_1 \\ x_2 \\ x_3 \\ y_1 \\ y_2 \\ y_3 \end{pmatrix} \approx \begin{pmatrix} b_1 \\ b_2 \\ b_3 \\ 0 \\ 0 \\ 0 \end{pmatrix} \tag{2.18}$$

Left multiply equation (2.18) with

$$\begin{pmatrix} R_1 & 0 & 0 & 0 & 0 & 0 \\ 0 & R_2 & 0 & 0 & 0 & 0 \\ 0 & 0 & R_3 & 0 & 0 & 0 \\ 0 & 0 & 0 & I & 0 & 0 \\ 0 & 0 & 0 & 0 & I & 0 \\ 0 & 0 & 0 & 0 & 0 & I \end{pmatrix} \begin{pmatrix} A_{11}^{-1} & 0 & 0 & 0 & 0 & 0 \\ 0 & A_{22}^{-1} & 0 & 0 & 0 & 0 \\ 0 & 0 & A_{33}^{-1} & 0 & 0 & 0 \\ 0 & 0 & 0 & I & 0 & 0 \\ 0 & 0 & 0 & 0 & I & 0 \\ 0 & 0 & 0 & 0 & 0 & I \end{pmatrix} \tag{2.19}$$

results in

$$\begin{pmatrix} I & 0 & 0 & 0 & L_1^T A_{11}^{-1} L_1 S_{12} & L_1^T A_{11}^{-1} L_1 S_{13} \\ 0 & I & 0 & L_2^T A_{22}^{-1} L_2 S_{21} & 0 & L_2^T A_{22}^{-1} L_2 S_{23} \\ 0 & 0 & I & L_3^T A_{33}^{-1} L_3 S_{31} & L_3^T A_{33}^{-1} L_3 S_{32} & 0 \\ I & 0 & 0 & -I & 0 & 0 \\ 0 & I & 0 & 0 & -I & 0 \\ 0 & 0 & I & 0 & 0 & -I \end{pmatrix} \cdot \begin{pmatrix} L_1^T x_1 \\ L_2^T x_2 \\ L_3^T x_3 \\ y_1 \\ y_2 \\ y_3 \end{pmatrix} = \begin{pmatrix} L_1^T A_{11}^{-1} b_1 \\ L_2^T A_{22}^{-1} b_2 \\ L_3^T A_{33}^{-1} b_3 \\ 0 \\ 0 \\ 0 \end{pmatrix} \tag{2.20}$$

Equation (2.20) can be simplified by removing the redundant equations, and we have:

$$\begin{pmatrix} y_1 \\ y_2 \\ y_3 \end{pmatrix} \approx \begin{pmatrix} E_{11} & S_{12} & S_{13} \\ S_{21} & E_{22} & S_{23} \\ S_{31} & S_{32} & E_{33} \end{pmatrix}^{-1} \cdot \begin{pmatrix} C_1 & 0 & 0 \\ 0 & C_2 & 0 \\ 0 & 0 & C_3 \end{pmatrix} \cdot \begin{pmatrix} b_1 \\ b_2 \\ b_3 \end{pmatrix} \tag{2.21}$$

where $E_{ii} = (L_i^T A_{ii}^{-1} L_i)^{-1}$, $C_i = E_{ii} L_i^T A_{ii}^{-1}$. Substituting equation(2.21) to equation(2.17) gives:

$$A^{-1} \approx A_D^{-1} - A_D^{-1} L_D S (E+S)^{-1} C_D \tag{2.22}$$

with $E = \begin{pmatrix} E_{11} & 0 & 0 \\ 0 & E_{22} & 0 \\ 0 & 0 & E_{33} \end{pmatrix}$ and $S = \begin{pmatrix} 0 & S_{12} & S_{13} \\ S_{21} & 0 & S_{23} \\ S_{31} & S_{32} & 0 \end{pmatrix}$. Moreover, from the simple fact that $S = (E+S) - E$, equation(2.22) can be rewritten as:

$$A^{-1} \approx A_D^{-1} - A_D^{-1} L_D C_D + A_D^{-1} L_D E (E+S)^{-1} C_D \tag{2.23}$$

where A_D, L_D, C_D are all block diagonal matrices whose diagonal blocks are A_{ii}, L_i, C_i, respectively. Finally, the approximate A^{-1} can be displayed as:

$$(A^{-1})^{N \times N} \approx D + B((E+S)^{-1})^{N_{k(1)} \times N_{k(1)}} C \tag{2.24}$$

with $B = A_D^{-1} L_D E$, $C = C_D$, $D = A_D^{-1} - A_D^{-1} L_D C_D$, N is the number of RWG basis functions, and $N_{k(1)}$ is the sum of all effective ranks of all groups, which in many applications can be notably less than N.

The use of equation(2.24) leads to a significant reduction in memory consumption since for all the matrices involved in equation(2.24), B, C, D, E matrices are all block diagonal. The S matrix is off-diagonal dense matrix, namely, $S_{ii} = 0$. However, considering its entries are nothing but a permuted subset of the original MoM impedance matrix in equation (2.7), we need only store the indices of the skeleton DoFs. This is crucial for the multi-level implementation. Even the four block diagonal matrices aforementioned, not all the entries need to be stored explicitly. One obvious approach stores only A_{ii}^{-1}, E_{ii} and L_i matrices, and subsequently, all operations involved in the direct solver can be fully accounted for.

2.2.2 Skeletons & Skeletonalization

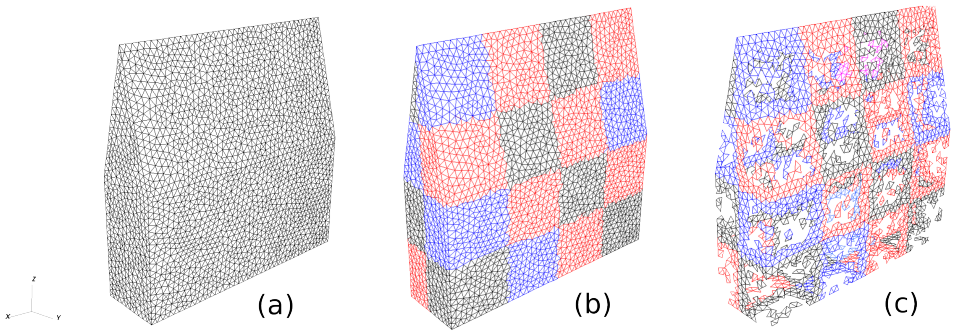

Figure 2.3: Skeletonalization

The skeletons, or the skeleton DoFs are the reduced set of DoFs that are capable of representing the receiving and/or radiating phenomena. Herein this section

we visually describe the skeleton and the related skeletonalization process through Figure.2.3. Take the example of an wedge geometry as illustrated in Figure.2.3 (a), the DoFs are partitioned into groups and their supports are depicted using distinct colors as in Figure.2.3 (b). The skeletonalization process would then be evoked to identify the skeleton of each group, i.e. the reduced set of DoFs, whose supports are colored the same as in Figure.2.3 (c). Thereafter, the indices of these reduced DoFs (or skeleton), are stored and utilized to assemble the S matrix.

2.2.3 Multi-level Direct Solver

Single-level direct solver takes advantage of the rank deficiency property of the off-diagonal coupling matrices and use the Shur's complement to represent the solution of the original problem in terms of a reduced set of unknowns, i.e., skeletons. Note that this reduced set of unknowns are a subset of the original unknowns, which implies that the redundancy exist between the first level partitions could still exist among couplings between different partitions of this reduced set of skeletons. Then these coupling matrices could still possess rank deficient property, if properly re-grouped. This can be seen clearly from the expression of $(E + S)$ matrix in equation(2.24), where the $[S]$ are nothing but the coupling matrices between the skeleton unknowns.

It would be logical to extend the algorithm to further compress the $(E+S)$ matrix in (2.24). Mathematically, one can simply substitute the original A matrix with the $(E + S)$ matrix obtained in equation(2.24). Subsequently, we cluster the DoFs within the current children groups into groups in higher levels, i.e., those *children* groups share the same *parent* in the tree structure. This re-grouping process can be straightforwardly demonstrated by Figure.2.4, i.e., the skeleton DoFs resulted from

the previous level operation as in Figure.2.4 (a) would be re-grouped into coarser level groups as in Figure.2.4 (b). In terms of matrix operation, this procedure is equivalent

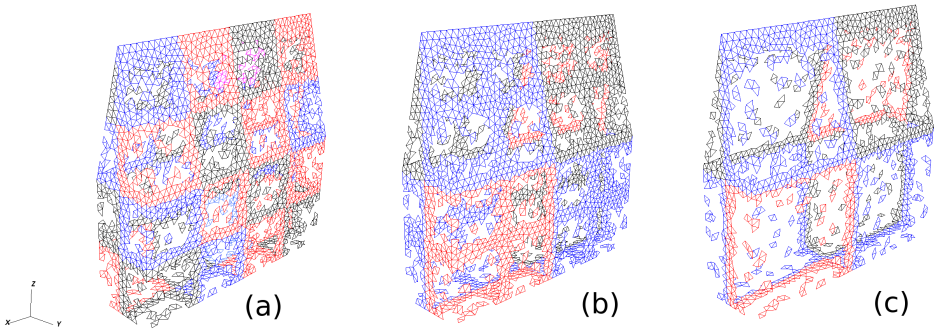

Figure 2.4: Multi-level Skeltonalization

to clustering the diagonal matrix groups as illustrated in Figure.2.5. After the 1^{st} level direct solver, the resulting $(E + S)$ matrix could be represented by the first square in Figure.2.5, where gray blocks represent matrices that are recalculated and updated, while dark blocks represents matrices that are not changed beyond row and column permutations. Subsequently, the red square lines would cluster the group to the next level and generate a $(E+S)$ matrix. Next, we perform the algorithm to this

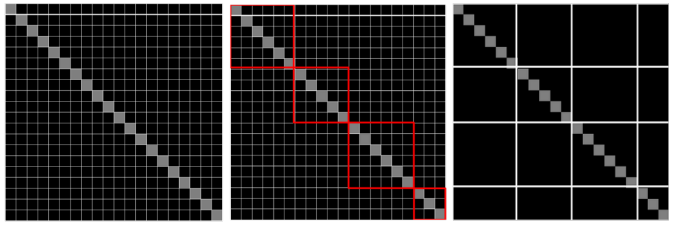

Figure 2.5: Matrix representation of the direct solver process. Gray blocks represents matrices that are updated, dark blocks represents matrices that are not changed beyond row and column permutation.

re-clustered $(E+S)$ matrix, i.e., identifying the skeletons and mapping matrices L_i of these new set of DoFs in the current level. The supports of the resulted skeletons are then plotted in Figure.2.4 (c). Mathematically, the corresponding expression can be written explicitly as:

$$(A^{-1})^{N\times N} \approx D+ \quad B[D_{(2)} + B_{(2)}((E_{(2)} + S_{(2)})^{-1})^{N_{k(2)}\times N_{k(2)}} C_{(2)}]^{N_{k(1)}\times N_{k(1)}} C \quad (2.25)$$

Note that the dimension of $(E_{(2)}+S_{(2)})$, i.e., $N_{k(2)}$, is further compressed. Continuing this algorithm recursively, one ends up with a multi-level version of the direct solver and consequently achieves gain in a telescope manner. The current multi-level direct solver would come to a halt and switch to direct LU factorization when it reaches the coarsest level, e.g., the level with no more than 8 groups left.

2.2.4 Skeletonalization Using A Huygen's Surface

Skeletons revealed in this algorithm are the effective basis functions that can accurately account for both the near field and far field couplings. For the group i, whose support of DoFs is depicted by red triangulation in Figure.2.6, its near field exhibits higher degree of oscillations/variations. However, the couplings between group i and the groups reside outside group i's Huygen's surface are smooth. Consequently, for DoFs that reside in groups outside group i (whose supports are colored black), the couplings could be accounted for much more efficiently using the Huygen's surface. The use of the Huygen's surface to compute far field couplings is justified through the Huygen's principle. Namely, any field radiating from any current enclosed inside the Huygen's surface is equivalent to the field radiating from the induced currents on the Huygen's surface [26]. We remark that the Huygen's surface could be any shape as long as Huygens principle is respected. In the current implementation, the

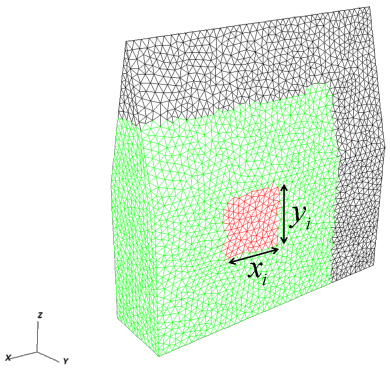

Figure 2.6: Near field and far field region of group i

Huygen's surfaces are constructed by simply setting $d_{\Gamma_i^a} \approx 3d_i$, where d_i is the box size at i^{th} level as in Figure.2.7. As a consequence, the skeletonalization process can be accelerated via Huygen's surfaces through the following steps. First, these surfaces denoted by Γ_a are discretized based on the precision required [26] as in Figure.2.7, and assigned basis functions to the corresponding traingulations. After this, instead of calculating the matrix equation(3.23), we assemble the following matrix $A_i^{\Gamma_a}$,

$$(A_i^{\Gamma_a})^{n_i \times 2(N_i^{nb}+2K)} =$$

$$\begin{bmatrix} A_{i,j_1} & A_{i,j_2} & \cdots & A_{i,j_{nb}} & A_{i,\Gamma_a} & A^T_{j_1,i} & A^T_{j_2,i} & \cdots & A^T_{j_{nb},i} & A^T_{\Gamma_a,i} \end{bmatrix} \tag{2.26}$$

where, N_i^{nb} is the number of basis functions in the neighboring groups of group i, K is the number of basis functions on Γ_a, $A_{i,k}$ denotes the coupling matrices where DoFs in group i serves as receiver and DoF j_{nb} serves as radiator while $A^T_{i,k}$ denotes the alternative scenario. Therefore, the adoption of the Huygen's surface Γ_a separates the far field from the near field.

Subsequently, the $A_i^{\Gamma_a}$ matrix is passed onto the pivoted *QR decomposition* as in equation (2.13). For a $m \times n$ matrix, the complexity of pivoted QR decomposition is

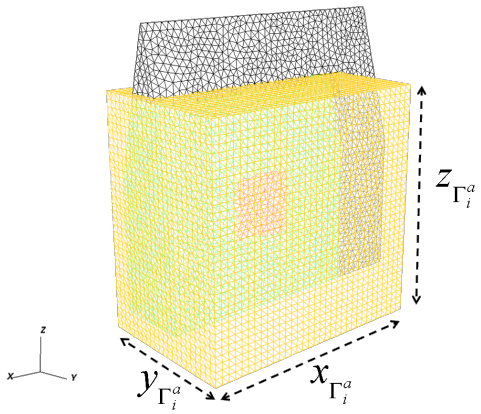

Figure 2.7: Artificial boundary of group i

u^2v, where $u = min\{m, n\}, v = max\{m, n\}$. For the case of direct solver, it is almost always valid that $(N_{tot} - n_i) >> (N_i^{nb} + 2K)$. Thus, the QR decomposition of $A_i^{\Gamma_a}$ is notably more efficient than its A_i counterpart.

2.3 Numerical Results

2.3.1 Sphere

The first example to validate the proposed algorithm is a plane wave, at 300 MHz, scattering from a 4m sphere radius PEC sphere discretized using an averaged mesh size of 0.1λ. The discretization gives rise to 74,169 unknowns. The entire problem geometry is decomposed hierarchically, via an oct-tree structure, and results in 3 levels of partitions. At the leaf level, we have total 272 non-empty groups, which corresponds to approximately 272 DoFs per group on average. CFIE with α=0.5 and QR threshold of 1.e-3 are adopted. The computed far fields are plotted against Mie series in Figure.2.8. On an Intel Xeon platform with X5450 CPUs at 3.00GHz, it takes 4 hours 55 minutes 14 seconds and 6.23 GB memory using double precision

arithmetic. While the direct LU factorization, we estimate, would take 595 hours 21 minutes 32 seconds.

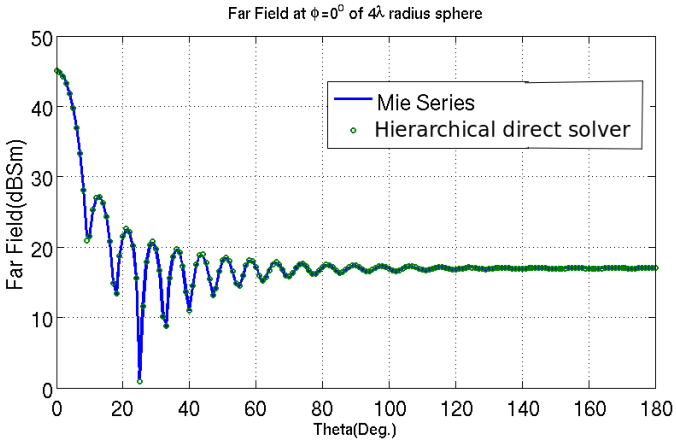

Figure 2.8: Computed RCS of a 4 λ radius sphere compared against the Mie Series results

2.3.2 Complexity and Error Studies

Two numerical experiments are conducted to study the computational complexity of the proposed direct solver, both the memory consumption and CPU computational time. Specifically, we aim to determine the computational complexity under two scenarios: the first one by fixing the mesh size with respect to the wavelength and increasing the frequency; and, the second one is to fix the operating frequency while decreasing the mesh size with respect to the wavelength. In all cases reported herein, the results are obtained using the CFIE with double precision and the tolerance of the QR decomposition is set to be 1.e-3. Moreover, we have parallelized the proposed algorithm using openMP and the computational results reported here are computed with 8 threads. The first complexity studies is a PEC sphere of 1.5m radius and

is discretized using mesh size of 0.1λ with varying frequency. The computational statistics are listed in Table 2.1, in which N denotes the number of DoFs for the problem and n denotes the size of the matrix that is subjected to direct LU factorization at the final level. complexity of approximately $O(N^{1.3})$ is observed for memory consumption and $O(N^{1.8})$ for CPU time. Note that our conclusion is simply based on the numerical results for this particular example. However, it does demonstrate the common trend that we have observed for many other examples. Since we can only apply the proposed direct solver, even with the aids of openMP parallelization, to moderate electrical size problems, we should not extrapolate the results to the asymptotic complexity of electrically large structures, where the unknowns may be in the range of hundreds of millions. Nevertheless, the computational complexity illustrated here are still very encouraging since for electrically large EM problems, the proposed direct solver will often be used in-conjunction with the Krylov iterative solver as an effective preconditioner.

Secondly, for the same sphere at 30MHz, we study the computational complexity with respect to the decrease of the mesh size (*h-refinement*). Computational statistics are obtained for different mesh sizes ranging from 0.01 to 0.0015 wavelengths; and, complexity of $O(N)$ for memory and $O(N^{1.5})$ for CPU times are observed from Table 2.2. Our observed complexity for both memory and CPU time agree well with the predictions described in [19].

Furthermore, we define three sets of error to investigate the accuracy of the solution. They are: (1). The solution error, i.e., ε_{sol}, defined as $\parallel x_{exact} - \tilde{x} \parallel / \parallel x_{exact} \parallel$, with x_{exact} denotes the solution computed from the usual LU factorization wherever possible; and, (2). The factorization error, denoted by $\varepsilon_{fac} = \underset{z}{max}\{\parallel z - A\tilde{A}^{-1}z \parallel$

Table 2.1: Computational Statistics for Fixed Mesh Size Study

freq.	level	N	n	Memory	CPU	ε_{fac}	ε_{app}
300MHz	3	10,242	3,515	0.46GB	4.90e+2s	6.43e-4	4.82e-4
375MHz	3	16,020	4,640	0.86GB	1.15e+3s	6.48e-4	4.83e-4
500MHz	4	28,806	6,450	1.87GB	3.39e+3s	7.64e-4	5.68e-4
600MHz	4	41,415	7,716	2.89GB	6.20e+3s	8.75e-4	7.23e-4
1000MHz	5	116,253	13,925	10.59GB	4.13e+4s	1.07e-3	8.84e-4
2000MHz	6	465,012	28,565	64.02GB	5.03e+5s	2.12e-3	9.23e-4

Table 2.2: Computational Statistics for Fixed Frequency Study

h (λ)	level	N	n	Memory	CPU	ε_{fac}	ε_{app}
0.01	3	10,242	2,644	0.31GB	6.80e+2s	3.42e-3	3.87e-4
0.008	3	16,020	3,396	0.52GB	1,38e+3s	4.25e-3	4.01e-4
0.006	4	28,806	4,597	1.03GB	3.41e+3s	5.80e-3	4.08e-4
0.005	4	41,415	5,474	1.50GB	5.88e+3s	6.47e-3	4.12e-4
0.003	5	116,253	9,256	4.32GB	2.78e+4s	1.06e-2	4.30e-4
0.0015	6	465,012	18,971	17.02GB	2.29e+5s	2.42e-2	5.65e-4

$/ \parallel z \parallel \}$, where $\tilde{A}$ is the approximate matrix to A through the skeletonization process; and, (3). The approximation error, $\varepsilon_{app} = \max_{z}\{\parallel Az - \tilde{A}z \parallel / \parallel Az \parallel \}$. We randomly generated 10 sets of *independent and identically distributed* (i.i.d.) vectors and perform the error calculations, the results of the maximum errors are included in Table 2.1 and Table 2.2 for fixed mesh size and fixed frequency scenarios, respectively.

Examine Table 2.1 and Table 2.2, we observe that the approximation errors are all less than the specified tolerance 1.e-3. However, both the solution and factorization errors increase monotonically as the number of DoFs increases. Especially in the fixed frequency case, where smaller discretization sizes translate directly to larger matrix condition numbers, ($\kappa(A) \propto \frac{1}{(kh)^2}$), without any low frequency regularization

techniques [31]. Moreover, the largest singular value of the coupling matrices of any group grows as $O(\frac{1}{h})$ since the smallest coupling capacitance between two neighboring groups decreases as $O(h)$; whereas the small singular values of the off-diagonal blocks are almost independent of the mesh size since they are predominantly associated with the MFIE operator. Behavior of similar nature was also reported in some literature, e.g. [7]. This phenomenon reinforces the statement that the condition number of the matrix would affect the performance of the direct solution algorithms, especially the ones rely on the rank deficiency of the system matrix [7]. So even for the direct solvers, it is still desirable to have formulations that are capable of yielding good conditioned system matrices.

2.3.3 Machine Gun

In this section, we consider a more complex and somewhat practical target. The current distribution on a free-standing machine gun subjected to an EM plane wave at 2 GHz is shown in Figure. 2.9. The target gives rise to 74,310 unknowns after being discretized, and 201 non-empty groups are established for the 1^{st} level, and 370 DoFs per group on average. Multi-scale structures like the machine gun discussed here would usually yield ill-conditioned matrix equations, that will be costly for the Krylov iterative methods to solve. In circumstances like this, the proposed direct solver will then be highly desirable. Particularly, when it is combined with the newly developed integral equation domain decomposition method (IEDDM) [20] as an effective sub-domain solver for sub-domains that involve singularities and/or small features. As an example, we mount the machine gun to a tank and calculate the EM scattering from it with the same incident plane wave. The entire target, after discretization, results

in 1,027,554 unknowns using a mesh size, on the average, $h = 0.1\lambda$. The current distribution is plotted in Figure. 2.10. In this example, the proposed direct solver serves as a sub-domain solver for the sub-domains, and therefore, the convergence of these sub-domains are guaranteed. At initial running, it took 5 hours 25 minutes to obtain the inverse representation of the impedance matrix for the machine gun domain alone. For the IE-DDM iterations other than the first one, responses from this subdomain can be solved by simply applying the existing inverse to the RHSs.

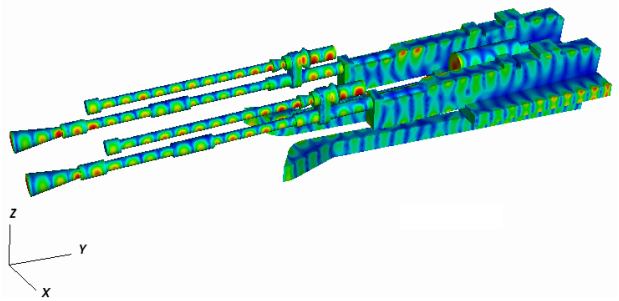

Figure 2.9: current distribution on a free-standing gun

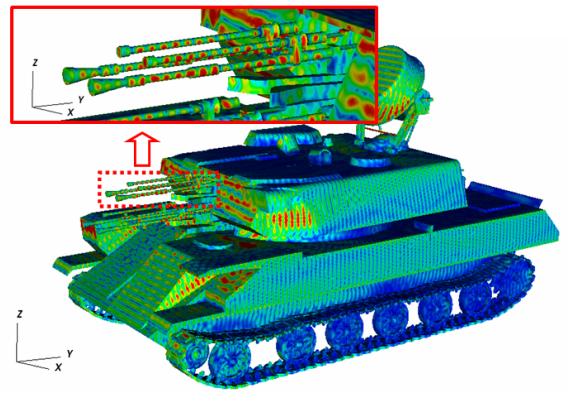

Figure 2.10: current distribution of a gun mounted on a tank

2.3.4 Mock-up Aircraft

For the final example, an electromagnetic wave scattering from a mock-up air platform at 75MHz is considered. The positive x polarized plane wave impinges from positive z direction. For this problem, we have a discretization of the surface with the average mesh size of approximately $\lambda/40$, which gives rise to 60,495 unknowns. It is usually difficult for a mesh generation software to guarantee the quality of each and every triangle when facing geometries of such complexity. However, the presence of ill-shaped triangles with inferior qualities would greatly affect the convergence behavior of the iterative solver, though the percentage of these bad triangles are usually very small. Additionally, the condition number of EFIE deteriorates [31] when it is applied to such a low frequency application. Combinations of these technical difficulties result in the failure of the Krylov iteration methods. Specifically we employed the CGS, and the relative residual stagnates around 0.1 after a few hundred iterations. To combat the above mentioned difficulties, we apply the proposed direct solver and it results in 4-level partitioning and with 221 non-empty groups and 273 DoFs per group on average for the leaf level. Figure 2.11 plots the computed current distribution on the platform, without the dielectric radome of the nose of the airplatform. Moreover, the mono-static far field pattern is also calculated and included in Figure. 2.12. On an Intel Xeon platform with 8 X5450 CPUs at 3.00GHz, it takes 3 hours 11 minutes 53 seconds to obtain the inverse representation. Then it takes 27 minutes 24 seconds to calculate the RHS response from 360 mono-static incident angles on $\phi = 0^o$ plane.

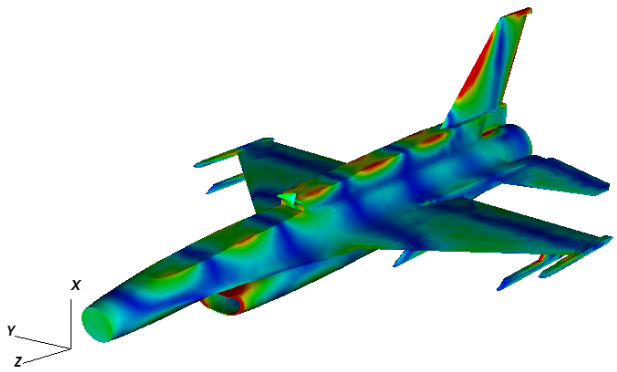

Figure 2.11: current distribution of a mock up platform at 75MHz

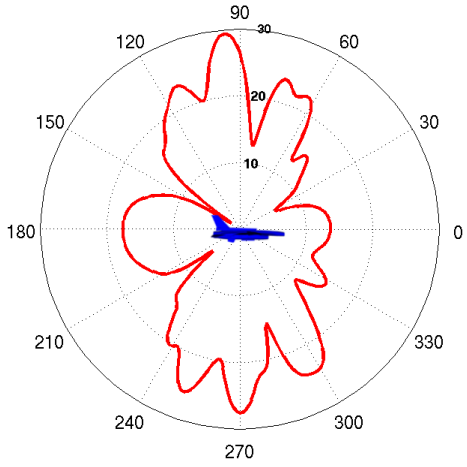

Figure 2.12: mono-static far field pattern of a mock up platform at 75MHz, observation plane $\phi = 0^o$

2.4 Conclusion

In this chapter, a hierarchical direct solver algorithm is developed to solve integral equations in 3D electromagnetic wave scattering from non-penetrable targets. The proposed algorithm utilizes the skeletonalization process to effectively compress the rank-deficient off-diagonal blocks, which correspond to the couplings between groups. Huygen's surfaces are also introduced to account for the far field couplings efficiently, and thus further accelerate the algorithm. It has been demonstrated that the condition number of the system matrix would still affect the solution errors of direct solvers. Despite the limitations, for problems of small or medium electrical sizes, the multi-level version of the proposed algorithm features $O(N^{1.3})$ and $O(N)$ complexity for memory consumption and $O(N^{1.8})$ and $O(N^{1.5})$ for CPU times for fixed mesh size and for h-refinement scenarios, respectively. We emphasize that the complexity reported herein are based on a finite number of moderate electrical size problems that we have studied, and should not be taken asymptotically into electrically large wave problems. Finally, the proposed direct solver when combined with the newly developed IEDDM equip us a versatile tool to solve complex electromagnetic problems with multiscale geometrical features.

Chapter 3: Hierarchial Multi-level Fast Multipole Method

A hierarchical multi-level fast multipole method (H-MLFMM) is elucidated herein to accelerate the solutions of surface integral equation (SIE) methods. The proposed algorithm is particularly suitable for solutions of wideband and multi-scale electromagnetic problems. As documented in [10] that the multi-level fast multipole method (MLFMM) achieves $O(NlogN)$ computational complexity in the fixed mesh size scenario, $hk = cst.$ where h is the mesh size and k is the corresponding wavenumber, for problems discretized under conventional mesh density. However, its performance deteriorates drastically for overly dense meshes where the couplings between different groups are dominated by evanescent waves or circuit physics. In the H-MLFMM algorithm, two different types of basis functions are proposed to address these two different natures of physics corresponding to the electrical size of the elements. Specifically, for the propagating wave couplings, the plane wave basis function adopted by MLFMM are effective and they are inherited by H-MLFMM. Whereas in the circuit physics and for the evanescent waves, H-MLFMM employs the so-called skeleton basis. Moreover, the proposed H-MLFMM unifies the procedures to account for the couplings using these two distinct types of basis functions. $O(N)$ complexity is observed for both memory and CPU time from a set of numerical examples with fixed

mesh sizes. Numerical results are included to demonstrate that H-MLFMM is error controllable and robust for a wide range of applications.

The contributions of the proposed H-MLFMM are mainly two folds. First, it distinguishes the evanescent wave interactions from the propagating wave interactions. Two different sets of basis functions are utilized to address these two different nature of physics, respectively. Second, H-MLFMM unifies these two interaction physics in a framework that the procedures are almost parallel to each other.

The rest of the chapter is organized as follows: Firstly, we present the problem statement, followed by the blueprint of the proposed H-MLFMM and an explanation of algorithm from a physical point of view. Subsequently, we detail the treatment of wave physics within H-MLFMM. Moreover, in this section, we offer an alternative interpretation of MLFMM from a transmitting-receiving model. Additionally, a two-step mapping is implemented to accelerate the aggregation and disaggregation operations within the proposed H-MLFMM for treating the wave physics interactions. Next section focuses on the treatment of circuit physics, or the evanescent wave interactions, via a skeletonalization algorithm. The proposed skeletonalization algorithm for addressing the circuit physics almost parallels the conventional MLFMM. Furthermore, a block diagonal pre-conditioner based on the same skeletonalization algorithm is also introduced. The details of the implementation of skeletonalization algorithm utilized in this chapter is elucidated. The error controllability, scalability and performance of the proposed H-MLFMM are documented in Section VII through several numerical examples. Finally, we conclude our studies and provide a brief summary of our findings.

3.1 Problem Statement

For electromagnetic wave scattering from a non-penetrable target, we have the following boundary value problem statement.

$$\begin{cases} \nabla \times \nabla \times \mathbf{E} - k^2 \mathbf{E} = 0 & in \ \ \Omega \\ \hat{\mathbf{n}} \times \mathbf{E} = 0 & on \ \Gamma_s \\ \lim_{|r| \to \infty} |r| (\nabla \times \mathbf{E}^{sca} + \jmath k \hat{\mathbf{r}} \times \mathbf{E}^{sca}) = 0 \end{cases} \tag{3.1}$$

An incident plane wave $\mathbf{E}^{inc}$ impinges on the boundary Γ_s of a PEC object Ω_s, the complement of the scatter is denoted by $\Omega \, (= \mathbb{R}^3 \setminus \Omega_s)$ and Γ_s is the bounding surface of Ω_s. The wavenumber is denoted by $k = \omega \sqrt{\mu_0 \varepsilon_0}$, with μ_0 and ε_0 being the permeability and the permittivity of the free space, respectively. Subsequently, we have the following boundary condition to be satisfied:

$$\pi_t \mathbf{E} = 0 \qquad on \ \Gamma_s \tag{3.2}$$

where π_t denotes the tangential trace operator on the surface and it is defined as $\pi_t \mathbf{u} = \hat{\mathbf{n}} \times \mathbf{u} \times \hat{\mathbf{n}}$. Expand $\mathbf{E} = \mathbf{E}^{inc} + \mathbf{E}^{sca}$, we have

$$-\pi_t \mathbf{E}^{inc} = \pi_t \mathbf{E}^{sca} \qquad on \ \Gamma_s \tag{3.3}$$

By introducing an equivalent electric current $\mathbf{J} = (\hat{\mathbf{n}} \times \mathbf{H}) \in H^{-1/2} \, (div_\Gamma, \Gamma_s)$, both the electric $\mathbf{E}$ and the magnetic $\mathbf{H}$ fields in the exterior region, Ω, can be well represented by $\mathbf{J}$ as a result of Stratton-Chu representation formulae. Thus, we have the electric field integral equation (EFIE):

$$\pi_t \mathbf{E}^{inc} = -\pi_t \mathcal{L}(\mathbf{J})(\mathbf{x}) \qquad on \ \Gamma_s \tag{3.4}$$

where $\mathcal{L}(\mathbf{J})(\mathbf{x}) = -\jmath k \eta \int_{\Gamma_s} [\bar{\bar{\mathbf{I}}} + \frac{1}{k^2} \bigtriangledown_\Gamma^{(x)} \bigtriangledown_\Gamma^{(y)} \cdot] G(\mathbf{x},\mathbf{y}) \mathbf{J}(\mathbf{y}) d\mathbf{y}$. $\bigtriangledown_\Gamma^{(x)}$ and $\bigtriangledown_\Gamma^{(y)}$ are respectively the surface gradient operators operated on the observation and the source coordinates.

Magnetic field integral equation (MFIE) can also be derived by invoking the boundary condition $(\hat{\mathbf{n}} \times \mathbf{H})(\mathbf{x}) = \mathbf{J}(\mathbf{x})$ for closed surface targets,

$$\pi_{\times}\mathbf{H}^{inc} = \mathcal{K}(\mathbf{J})(\mathbf{x}) \tag{3.5}$$

where $\mathcal{K}(\mathbf{J})(\mathbf{x}) = \mathbf{J}(\mathbf{x}) - \hat{\mathbf{n}} \times \int_{\Gamma_s} \bigtriangledown_{\Gamma}^{(x)} G(\mathbf{x},\mathbf{y}) \times \mathbf{J}(\mathbf{y}) d\mathbf{y}$, $\pi_{\times}\mathbf{u} = \hat{\mathbf{n}} \times \mathbf{u}$ and $G(\mathbf{x},\mathbf{y}) = \frac{e^{-\jmath k|\mathbf{x}-\mathbf{y}|}}{|\mathbf{x}-\mathbf{y}|}$ is the Green's function in free space. Note that the MFIE formulation equation (3.5), is only applicable to closed-surfaced non-penetrable targets.

The combined field integral equation (CFIE) combines the EFIE and the MFIE to yield:

$$\alpha\pi_t\mathbf{E}^{inc} + (1-\alpha)\eta\pi_{\times}\mathbf{H}^{inc} = \alpha(-\pi_t\mathcal{L}(\mathbf{J})(\mathbf{x})) + (1-\alpha)\eta\mathcal{K}(\mathbf{J})(\mathbf{x}) \tag{3.6}$$

where $\eta = \sqrt{\mu_0/\varepsilon_0}$ is the free space intrinsic impedance. The CFIE formulation mitigates the notorious internal resonances by effectively using the impedance boundary condition on Γ_s, which renders the resonance frequencies complex, so long as the coefficient $\Re\alpha \neq 0$.

3.2 An Overview of the Hierarchical MLFMM

Depending on the electrical sizes and the distance separated between two groups, the interactions between them are dominated by either propagating wave or circuit (evanescent wave) physics. Accordingly, different numerical treatments should be applied to reflect the two distinct natures of physics. Assuming two groups of DoFs whose supports are denoted as Γ_i and Γ_j in Figure.3.1. If $D_{ij} > d_{min}$, the interaction between group i and group j mainly corresponds to the propagation physics, where EM energy travels and exchanges between group i and group j. Moreover, d_{min} is a chosen minimum distance to separate predominately the wave and circuit physics

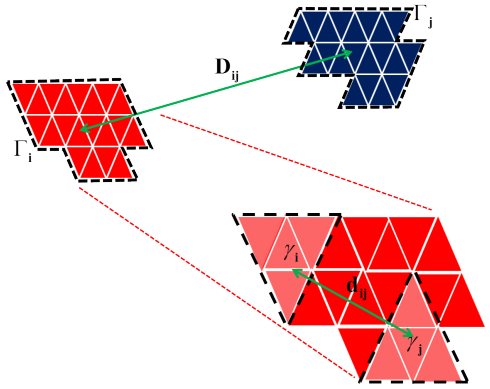

Figure 3.1: Propagation and evanescent wave physics

(herein, we set $d_{min} = \lambda/4$). For groups that are well separated, i.e., $D_{ij} > d_{min}$, energy is predominantly exchanged through wave propagation between the transmitting and receiving groups. The plane wave basis adopted by the conventional MLFMM is well-suited to represent propagating EM waves, hence they are inherited herein to deal with the propagating wave physics effectively.

Another class of interactions is illustrated in Figure. 3.1 between group γ_i and group γ_j. We name this type of coupling "Huygens' coupling", and they mainly occur between groups with small separation distances, namely $d_{ij} < d_{min}$. For interactions involved in the Huygen's coupling, the majority of the energy is trapped locally and converts back and forth between the capacitive and inductive stored energy. The plane wave basis adopted for the wave physics would not be adequate for the Huygen's coupling. Alternatively, we employ the so-called *skeletons* as the basis to account for the interactions between γ_i and γ_j. Unlike the conventional MLFMM, which requires its leaf level group size to be no less than $\lambda/4$ regardless the number of DoFs resides in, H-MLFMM enforces no restrictions on the electrical size of the groups. As a

consequence, the average number of DoFs at the leaf level of the H-MLFMM can always be brought under a certain threshold n_t (typically, we set $n_t = 50$ in this work).

3.3 Propagating Wave Physics

As discussed earlier, interactions between two well-separated groups, $D_{ij} > d_{min}$, are dominated by propagating waves. Consequently, the MLFMM is capable of computing the couplings between them efficiently via the use of plane wave basis. In this section, we present a slightly different perspective of the MLFMM and further introduce a two-step mapping to accelerate the projection between the RWG basis and the plane wave basis.

3.3.1 Revisit the MLFMM

Conventional MLFMM projects the original basis to plane wave basis and accelerates the coupling process in an efficient and error controllable manner. In the following paragraphs an alternative prospective would be elucidated to re-examine the conventional MLFMM, a close connection would be established between the MLFMM and the H-MLFMM afterwards. Conventional MLFMM starts by partitioning the 3D geometry into hierarchical oct-tree groups and then assigns DoFs into corresponding groups according to their geometrical positions. For the sake of simplicity, we assume a binary-tree partition for the following discussion. For a group i at level L, there exists a surface $\Gamma_i^{(L)}$ that encapsulates the support of its DoFs, where i is the group number. Then the coupling phenomena can be classified into two categories.

We refer to the first type of interaction as radiation coupling, where group i and group j satisfy $\Gamma_i^{(L)} \bigcap \Gamma_j^{(L)} = \varnothing$. The corresponding matrix blocks $\mathcal{R}$ are denoted

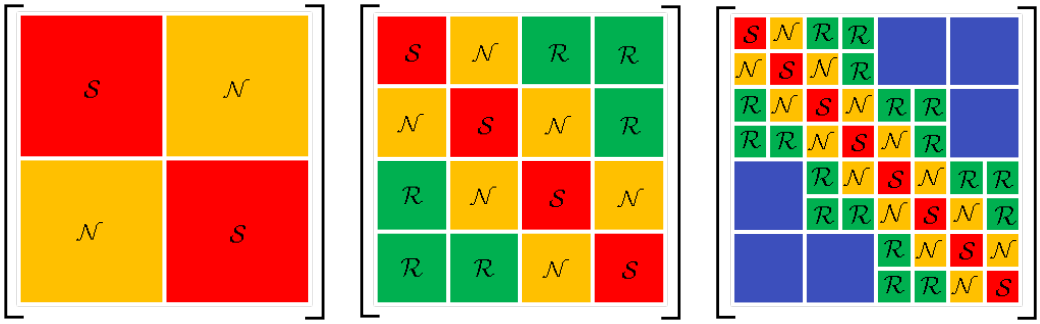

Figure 3.2: Matrix representation corresponding to level 1 (a), level 2 (b) and level 3 (c) binary partition of conventional MLFMM.

by green squares in Figure.3.2, while $\mathcal{S}$ represents self coupling and $\mathcal{N}$ stands for near field coupling between groups that touching each other. Conventional MLFMM adopts the projection between the original basis function and the plane wave basis to accelerate this type of coupling. Take Figure.3.2(c) for example, $\mathcal{R}_{ij}^{(3)}$ denotes the radiation coupling between group i and group j at level 3.

$$\mathcal{R}_{ij}^{(3)} = (\mathcal{X}_i^H)^{(3)} \mathcal{T}_{ij}^{(3)} \mathcal{X}_j^{(3)} = \left[\begin{array}{cc} \mathcal{X}_\theta^H & \mathcal{X}_\phi^H \end{array} \right]_i^{(3)} \left[\begin{array}{cc} \overline{\mathcal{T}}_{ij} & 0 \\ 0 & \overline{\mathcal{T}}_{ij} \end{array} \right]^{(3)} \left[\begin{array}{c} \mathcal{X}_\theta \\ \mathcal{X}_\phi \end{array} \right]_j^{(3)} \tag{3.7}$$

where $(\mathcal{X}_\theta)^{M \times N_i^{(3)}} = \int_{S_i} \left[\begin{array}{c} \hat{\theta}_1 e^{-j\vec{\mathbf{k}_1}\cdot\vec{\mathbf{d}}} \\ \hat{\theta}_2 e^{-j\vec{\mathbf{k}_2}\cdot\vec{\mathbf{d}}} \\ \vdots \\ \hat{\theta}_M e^{-j\vec{\mathbf{k}_M}\cdot\vec{\mathbf{d}}} \end{array} \right] \cdot \left[\begin{array}{cccc} \vec{\alpha}_1(\vec{\mathbf{d}'}) & \vec{\alpha}_2(\vec{\mathbf{d}'}) & \cdots & \vec{\alpha}_{N_i^{(3)}}(\vec{\mathbf{d}'}) \end{array} \right]$,

$(\mathcal{X}_\phi)^{M \times N_i^{(3)}} = \int_{S_i} \left[\begin{array}{c} \hat{\phi}_1 e^{-j\vec{\mathbf{k}_1}\cdot\vec{\mathbf{d}}} \\ \hat{\phi}_2 e^{-j\vec{\mathbf{k}_2}\cdot\vec{\mathbf{d}}} \\ \vdots \\ \hat{\phi}_M e^{-j\vec{\mathbf{k}_M}\cdot\vec{\mathbf{d}}} \end{array} \right] \cdot \left[\begin{array}{cccc} \vec{\alpha}_1(\vec{\mathbf{d}}) & \vec{\alpha}_2(\vec{\mathbf{d}}) & \cdots & \vec{\alpha}_{N_j^{(3)}}(\vec{\mathbf{d}}) \end{array} \right]$ and

$$(\overline{\mathcal{T}}_{ij}^{(3)})^{M \times M} = \left[\begin{array}{cccc} \omega(\hat{\mathbf{k}}_1)\mathcal{T}_1 & 0 & \cdots & 0 \\ 0 & \omega(\hat{\mathbf{k}}_2)\mathcal{T}_2 & \cdots & 0 \\ \vdots & \vdots & \vdots & \vdots \\ 0 & 0 & \cdots & \omega(\hat{\mathbf{k}}_M)\mathcal{T}_M \end{array} \right].$$

Among the expressions, $\mathcal{X}_j^{(3)}$ is the so-called aggregation matrix and $(\mathcal{X}_i^H)^{(3)}$ is the disaggregation matrix. $\vec{\alpha}_\kappa(\vec{\mathbf{d}})$ denotes the original basis functions (usually the RWG functions), $\kappa = 1, 2, \cdots N_i^{(3)}$, here $N_i^{(3)}$ is the number of DoFs within group i at level 3. $\mathcal{T}_m(\vec{\mathbf{k}}_m \cdot \vec{\mathbf{D}}_{ij}) = \sum_{l=1}^{L}(-j)^l(2l+1)h_l^{(2)}(k\mathbf{D}_{ij})P_l(\hat{\mathbf{D}}_{ij} \cdot \hat{\mathbf{k}}_m)$, $m = 1, 2, ..., M$ and M is the number of plane wave basis adopted, usually $M = 2L^2$, where L is the mode number[32]. $h_l^{(2)}$ is the spherical Hankel function of the second kind, P_l is a Legendre polynomial. $\omega(\hat{\mathbf{k}}_m)$ is the weight of the quadrature point at each plane wave direction $\hat{\mathbf{k}}_m$.

Physically, this can be explained via the antenna communication model as follows. Assuming a given current $\vec{\mathbf{J}}_t(\vec{\mathbf{d}'})$ as a transmitting antenna, The radiation pattern at direction $\hat{\mathbf{k}}(\theta, \phi)$ can be expressed as follows,

$$\vec{\mathbf{E}}^t(\hat{\mathbf{k}}) = \left(\hat{\theta} \cdot \int_{S_i} e^{-j\vec{\mathbf{k}}\cdot\vec{\mathbf{d}}'}\vec{\mathbf{J}}_t(\vec{\mathbf{d}'})\right)\hat{\theta} + \left(\hat{\phi} \cdot \int_{S_i} e^{-j\vec{\mathbf{k}}\cdot\vec{\mathbf{d}}\,'}\vec{\mathbf{J}}_t(\vec{\mathbf{d}'})\right)\hat{\phi} \tag{3.8}$$

Next, the transmitting antenna's outgoing radiation pattern is transformed to the incoming radiation pattern as follows (at $\hat{\mathbf{k}}$ direction),

$$\vec{\mathbf{E}}_I^t(\hat{\mathbf{k}}) = \mathcal{T}(\hat{\mathbf{k}})\vec{\mathbf{E}}^t(\hat{\mathbf{k}}) \tag{3.9}$$

Now suppose we have another receiving antenna with current $\vec{\mathbf{J}}_r(\vec{\mathbf{d}})$, and subsequently its receiving pattern at direction $\hat{\mathbf{k}}$ can be expressed by

$$\vec{\mathbf{E}}^r(\hat{\mathbf{k}}) = \left(\hat{\theta} \cdot \int_{S_i} e^{j\vec{\mathbf{k}}\cdot\vec{\mathbf{d}}}\vec{\mathbf{J}}_r(\vec{\mathbf{d}})\right)\hat{\theta} + \left(\hat{\phi} \cdot \int_{S_i} e^{j\vec{\mathbf{k}}\cdot\vec{\mathbf{d}}}\vec{\mathbf{J}}_r(\vec{\mathbf{d}})\right)\hat{\phi} \tag{3.10}$$

Consequently, the reaction density $\mathcal{P}^r(\hat{\mathbf{k}})$ for the receiving antenna at the direction $\hat{\mathbf{k}}$ is:

$$\mathcal{P}^r(\hat{\mathbf{k}}) = \vec{\mathbf{E}}^r(\hat{\mathbf{k}}) \cdot \vec{\mathbf{E}}_I^t(\hat{\mathbf{k}}) \tag{3.11}$$

And, the total reaction $\mathcal{P}^r$ can be obtained by integrating over the unit sphere,

$$\mathcal{P}^r = \int d^2\hat{k}\mathcal{P}^r(\hat{\mathbf{k}}) \approx \sum_{m=1}^{M} \omega(\hat{\mathbf{k}}_m)\mathcal{P}^r(\hat{\mathbf{k}}_m) = \sum_{m=1}^{M} \omega(\hat{\mathbf{k}}_m)\vec{\mathbf{E}}^r(\hat{\mathbf{k}}_m) \cdot \vec{\mathbf{E}}_I^t(\hat{\mathbf{k}}_m) \tag{3.12}$$

where M is the number of quadrature points on the unit sphere, each quadrature point corresponds to a plane wave basis (usually $M = 2L^2$); and, $\omega(\hat{\mathbf{k}}_m)$ is the weight associated with the quadrature direction $\hat{\mathbf{k}}_m$.

The incoming radiation pattern can be recast as

$$\vec{\mathbf{E}}_I^t(\hat{\mathbf{k}}_m) = \mathcal{T}(\hat{\mathbf{k}}_m)[\mathcal{E}_\theta^t(\hat{\mathbf{k}}_m)\hat{\theta}_m + \mathcal{E}_\phi^t(\hat{\mathbf{k}}_m)\hat{\phi}_m] \tag{3.13}$$

where $\mathcal{E}_\theta^t(\hat{\mathbf{k}}_m) = \hat{\theta}_m \cdot \int_{S_i} e^{-j\vec{\mathbf{k}}_m \cdot \vec{\mathbf{d}}'} \vec{\mathbf{J}}_t(\vec{\mathbf{d}}')$ and $\mathcal{E}_\phi^t(\hat{\mathbf{k}}_m) = \hat{\phi}_m \cdot \int_{S_i} e^{-j\vec{\mathbf{k}}_m \cdot \vec{\mathbf{d}}'} \vec{\mathbf{J}}_t(\vec{\mathbf{d}}')$

Similarly, $\vec{\mathbf{E}}^r(\hat{\mathbf{k}}_m)$ can be re-written as

$$\vec{\mathbf{E}}^r(\hat{\mathbf{k}}_m) = \mathcal{E}_\theta^r(\hat{\mathbf{k}}_m)\hat{\theta}_m + \mathcal{E}_\phi^r(\hat{\mathbf{k}}_m)\hat{\phi}_m \tag{3.14}$$

Consequently, the numerical integration process in equation (3.12) can be cast into the following matrix form,

$$\mathcal{P}^r = \begin{bmatrix} (\mathbf{E}_\theta^r)^T & (\mathbf{E}_\phi^r)^T \end{bmatrix} \begin{bmatrix} \overline{\mathcal{T}} & 0 \\ 0 & \overline{\mathcal{T}} \end{bmatrix} \begin{bmatrix} \mathbf{E}_\theta^t \\ \mathbf{E}_\phi^t \end{bmatrix} \tag{3.15}$$

where $\mathbf{E}_\theta^t = \begin{bmatrix} \mathcal{E}_\theta^t(\hat{\mathbf{k}}_1) & \mathcal{E}_\theta^t(\hat{\mathbf{k}}_2) & \cdots & \mathcal{E}_\theta^t(\hat{\mathbf{k}}_M) \end{bmatrix}^T$,
$\mathbf{E}_\phi^t = \begin{bmatrix} \mathcal{E}_\phi^t(\hat{\mathbf{k}}_1) & \mathcal{E}_\phi^t(\hat{\mathbf{k}}_2) & \cdots & \mathcal{E}_\phi^t(\hat{\mathbf{k}}_M) \end{bmatrix}^T$,
$\mathbf{E}_\theta^r = \begin{bmatrix} \mathcal{E}_\theta^r(\hat{\mathbf{k}}_1) & \mathcal{E}_\theta^r(\hat{\mathbf{k}}_2) & \cdots & \mathcal{E}_\theta^r(\hat{\mathbf{k}}_M) \end{bmatrix}$, $\mathbf{E}_\phi^r = \begin{bmatrix} \mathcal{E}_\phi^r(\hat{\mathbf{k}}_1) & \mathcal{E}_\phi^r(\hat{\mathbf{k}}_2) & \cdots & \mathcal{E}_\phi^r(\hat{\mathbf{k}}_M) \end{bmatrix}$,
$\overline{\mathcal{T}} = \begin{bmatrix} \omega(\hat{\mathbf{k}}_1)\mathcal{T}_1 & \omega(\hat{\mathbf{k}}_2)\mathcal{T}_2 & ... & \omega(\hat{\mathbf{k}}_M)\mathcal{T}_M \end{bmatrix} \cdot \bar{\bar{\mathbf{I}}}$, where $\bar{\bar{\mathbf{I}}}$ is the identity matrix.

Using the expression in equation (3.7), the current in the transmitting group can be re-written as
$\vec{\mathbf{J}}_t(\vec{\mathbf{d}}') = \begin{bmatrix} \vec{\alpha}_1(\vec{\mathbf{d}}') & \vec{\alpha}_2(\vec{\mathbf{d}}') & \cdots & \vec{\alpha}_{N_j^{(3)}}(\vec{\mathbf{d}}') \end{bmatrix} \cdot \tilde{\mathcal{J}}_j$ while the current in the receiving group is re-written as $\vec{\mathbf{J}}_r(\vec{\mathbf{d}}) = \begin{bmatrix} \vec{\alpha}_1(\vec{\mathbf{d}}) & \vec{\alpha}_2(\vec{\mathbf{d}}) & \cdots & \vec{\alpha}_{N_i^{(3)}}(\vec{\mathbf{d}}) \end{bmatrix} \cdot \tilde{\mathcal{J}}_i$. Consequently,

the aggregation and disaggregation matrix in equation (3.7) can be decomposed as $\mathbf{E}_\theta^t = \mathcal{X}_\theta \cdot \tilde{\mathcal{J}}_j^t$, $\mathbf{E}_\phi^t = \mathcal{X}_\phi \cdot \tilde{\mathcal{J}}_j^t$, $\mathbf{E}_\theta^r = \mathcal{X}_\theta^* \cdot \tilde{\mathcal{J}}_i^r$ and $\mathbf{E}_\phi^r = \mathcal{X}_\phi^* \cdot \tilde{\mathcal{J}}_i^r$, where $\tilde{\mathcal{J}}_j^t$ and $\tilde{\mathcal{J}}_i^r$ are the column coefficient vectors of basis functions in the transmitting and receiving groups, respectively. Finally, the relationship between the reaction $\mathcal{P}_{ij}^r$ and the radiation coupling $\mathcal{R}_{ij}$ in equation (3.7) can be established as follows,

$$\mathcal{P}_{ij}^r \approx (\tilde{\mathcal{J}}_i^r)^T \mathcal{R}_{ij} (\tilde{\mathcal{J}}_j^t) \tag{3.16}$$

Similar expansion as equation (3.7) can be derived for higher levels as well. For instance, the radiation coupling between group i and group j at level 2 illustrated by Figure.3.2(b) can be cast into the following expansion,

$$\mathcal{R}_{ij}^{(2)} \approx (\mathcal{X}_i^H)^{(2)} \mathcal{T}_{ij}^{(2)} \mathcal{X}_j^{(2)} \tag{3.17}$$

A naive implementation of equation (3.17) requires assembling and storing two types of dense matrices, i.e., $\left(\mathcal{X}_i^{(2)}\right)^{M \times N_i^{(2)}}$ and $\left(\mathcal{X}_j^{(2)}\right)^{M \times N_j^{(2)}}$. Normally $M \propto (kd)^2$ and $N_i^{(2)} \propto (kd)^2$ for surface integral problems, large kd at coarser levels would render equation (3.17) expensive and inefficient. Instead, MLFMM further expands $\mathcal{X}_i^{(2)}$ through interpolating the aggregation and disaggregation matrices of its children's groups. Physically this is equivalent to approximate the far field via interpolation from far fields of the children groups. Take $\mathcal{E}_\theta$ for example,

$$\begin{bmatrix} \mathcal{E}_{1\theta} \\ \vdots \\ \mathcal{E}_{M\theta} \\ \mathcal{E}_{(M+1)\theta} \\ \vdots \\ \mathcal{E}_{(4M)\theta} \end{bmatrix}^{(2)} = \mathcal{I}_j^{(2,3)} \cdot \begin{bmatrix} (\mathcal{E}_{1\theta})_{j,1} + (\mathcal{E}_{1\theta})_{j,2} \\ \vdots \\ (\mathcal{E}_{4M\theta})_{j,1} + (\mathcal{E}_{4M\theta})_{j,2} \end{bmatrix}^{(3)} \tag{3.18}$$

where $\mathcal{I}_j^{(2,3)} = \begin{bmatrix} 1 & \cdots & 0 \\ \vdots & \ddots & \vdots \\ 0 & \cdots & 1 \\ c_{M+1,1} & \cdots & c_{M+1,M} \\ \vdots & \ddots & \vdots \\ c_{4M,1} & \cdots & c_{4M,M} \end{bmatrix}^{(2,3)}$ and $c_{a,b}$ denotes the weight of b^{th} spectrum at level 3 that is used in the interpolation of a^{th} spectrum at level 2, $a = 1, 2, \cdots, 4M$ and $b = 1, 2, \cdots, M$. In [10] a local interpolation results in a sparse matrix and it reveals that the interpolation error decreases exponentially as the number of interpolation points is increased. Plug equation (3.18) into equation (3.16), the reaction received by group i that is transmitted by group j at level 2 can be formulated as:

$$\mathcal{P}_{ij}^{(2)} \approx (\tilde{\mathcal{J}}_i^{(2)})^T \left(\overline{\mathcal{X}}_i^{(2,3)}\right)^H \left(\overline{\mathcal{I}}_i^{(2,3)}\right)^T \begin{bmatrix} \overline{\mathcal{T}}_{ij} & 0 \\ 0 & \overline{\mathcal{T}}_{ij} \end{bmatrix}^{(2)} \left(\overline{\mathcal{I}}_j^{(2,3)}\right) \left(\overline{\mathcal{X}}_j^{(2,3)}\right) \tilde{\mathcal{J}}_j^{(2)} \tag{3.19}$$

where $\tilde{\mathcal{J}}_j^{(2)}$ is the coefficient column vector for group j at level 2. Explicitly, we have $\tilde{\mathcal{J}}_j^{(2)} = \begin{bmatrix} \tilde{\mathcal{J}}_{j,1}^{(3)} \\ \tilde{\mathcal{J}}_{j,2}^{(3)} \end{bmatrix}$, assuming a binary-tree partition is adopted. Also $\left(\overline{\mathcal{X}}_j^{(2,3)}\right) = \begin{bmatrix} (\mathcal{X}_\theta)_{j,1}^{(3)} & (\mathcal{X}_\theta)_{j,2}^{(3)} \\ (\mathcal{X}_\phi)_{j,1}^{(3)} & (\mathcal{X}_\phi)_{j,2}^{(3)} \end{bmatrix}$. Subsequently, the radiation coupling between group i and group j at level 2, illustrated by Figure.3.2(b), can be approximated by:

$$\mathcal{R}_{ij}^{(2)} \approx \left(\overline{\mathcal{X}}_i^{(2,3)}\right)^H \left(\overline{\mathcal{I}}_i^{(2,3)}\right)^T \begin{bmatrix} \overline{\mathcal{T}}_{ij} & 0 \\ 0 & \overline{\mathcal{T}}_{ij} \end{bmatrix}^{(2)} \left(\overline{\mathcal{I}}_j^{(2,3)}\right) \left(\overline{\mathcal{X}}_j^{(2,3)}\right) \tag{3.20}$$

The second type of coupling takes place between two groups that fail to satisfy $\Gamma_i^{(L)} \bigcap \Gamma_j^{(L)} = \varnothing$. Matrix blocks correspond to this type of coupling are represented by red and orange blocks in Figure.3.2, where red blocks denote the self-term $\mathcal{S}$ and orange blocks denote neighboring coupling $\mathcal{N}$. For self-term and neighboring coupling matrices, the original DoF basis functions, e.g. RWGs are directly employed for the computations. Inherently, MLFMM does not require the existence of a rectangular

grid, however, it facilitates the identification of the aforementioned couplings by simply enforcing the $\Gamma_i^{(L)}$ to be the rectangular brick from the Cartesian partition. Also this Cartesian grid creates repetitive partition patterns such that one set of translators $\mathcal{T}_{ij}$ can be shared for each level of partition. Lastly, this helps to admit interpolation techniques such that the plane wave contributions can be projected between adjacent partition levels in a highly efficient manner.

3.3.2 Far Field Skeleton Basis for Aggregation/Disaggregation Matrix

The matrices $\mathcal{X}_i$ in equation (3.7) that accomplish the change of basis from RWG to plane wave basis, i.e., aggregation and disaggregation matrices, prove to be highly rank deficient [33] when the original DoFs are overly populated. Some work has been done previously to reduce the linear dependencies via the singular value decomposition (SVD) [33]. H-MLFMM herein takes advantage of the linear dependencies through a two-step change of basis procedure.

Take the aggregation matrix $(\mathcal{X}_j)^{M\times N_j}$ from equation (3.7) for instance, where M is the number of plane wave basis employed and N_j is the number of the original DoFs within this group. This dense matrix accomplishes the projection from the original DoFs to the plane wave basis. It can be interpreted as a set of N_j column vectors. These N_j columns become increasingly linearly dependent as the number of DoFs per square wavelength grows. This is mainly because of the smoothness of the far field, which is independent of the number of original DoFs within the group. H-MLFMM extracts the k_j numerically independent columns up to a preset tolerance. These columns relates to k_j DoFs and they are a subset of the original DoFs. The rest of the columns can then be expressed as linear combinations of these skeleton columns.

Subsequently, the aggregation process can be rewritten as a two-step mapping as follows,

$$(\mathcal{X}_j)^{M\times N_j} \approx (\mathcal{F}_j)^{M\times k_j} (\mathcal{P}_j)^{k_j\times N_j} \tag{3.21}$$

where $\mathcal{P}_j$ is a mapping matrix that maps the original N_j DoFs to k_j far field skeletons, $\mathcal{F}_j$ is a subset of the original $\mathcal{X}_j$ matrix and it continues mapping the k_j far field skeletons to M plane wave basis. Note that this far field skeleton should be distinguished from the near field skeleton adopted in the next section.

3.4 Evanescent Modes Spectrum

Interactions within this regime reflect predominantly evanescent waves phenomena as the mesh density increases. Conventional MLFMM fails to address this category of coupling effectively via plane wave basis. H-MLFMM adopts a new set of basis, i.e., near field skeleton basis, and takes advantage of the Huygens' principle to account for this type of physics. A single level skeletonalization algorithm would be presented first. Next, a hierarchical skeletonalization algorithm is developed to expedite the matrix vector multiplication. Even after the change of basis, the compressed interaction matrices may still be numerically rank deficient and we shall exploit the redundancy by ACA algorithm to further reduce the needed computational resources.

3.4.1 Near Field Skeletons For Huygens' Couplings

For the sake of simplicity, we assume a binary tree partition and the impedance matrix can be illustrated as in Figure.3.3 to demonstrate the skeletonalization algorithm. Figure 3.3(a) offers a zoom-in view of the upper-left conner of Figure.3.2(c), i.e., $\mathcal{H}_{ij}^{(0)} = \mathcal{R}_{ij}^{(3)}$. For each of the groups from level 0 to level 2 in Figure.3.3, there

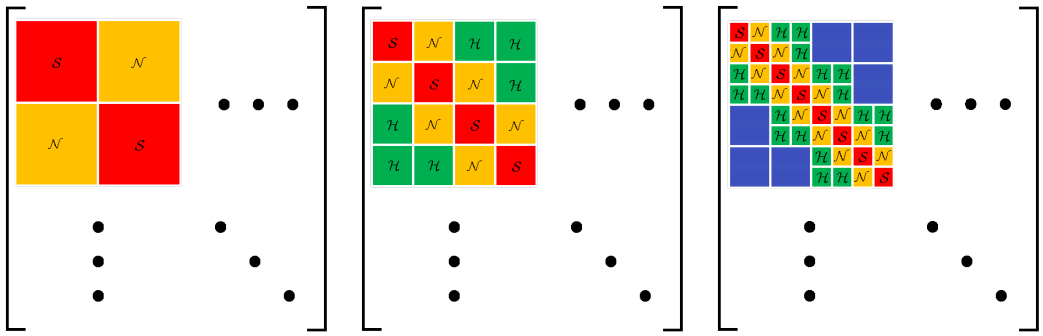

Figure 3.3: Matrix representation corresponding to level 0 (a), level 1 (b) and level 2 (c) binary paritition of H-MLFMM.

exists a minimum Huygens' surface $\Gamma_i^{(L)}$ that encapsulates the support of its DoFs, where i is the group number. The skeleton basis can then be employed to represent the interactions between group i and any group j that satisfies $\Gamma_i^{(L)} \bigcap \Gamma_j^{(L)} = \varnothing$.

Take the H-MLFMM leaf level illustrated by Figure.3.3(c) for instance. Each of the Huygens' coupling pairs can be decomposed as,

$$\mathcal{H}_{ij}^{(2)} \approx \mathcal{V}_i^{(2)} \mathcal{S}_{ij}^{(2)} \left(\mathcal{V}_j^{(2)}\right)^T \tag{3.22}$$

where $\mathcal{H}_{ij}^{(2)}$ denotes the Huygens' coupling between group i and group j from level 2, $\mathcal{V}_i^{(2)}$ denotes the mapping matrix that projects the skeletons to the original DoFs in the receiving group i, $\left(\mathcal{V}_j^{(2)}\right)^T$ denotes the mapping matrix that projects its original DoFs to its skeletons in the transmitting group j and $\mathcal{S}_{ij}^{(2)}$ is the dense coupling matrix between the skeletons of two corresponding groups. Instead of calculating the original dense coupling matrix $\mathcal{H}_{ij}^{(2)}$, H-MLFMM only assembles and stores a reduced dense matrix $\mathcal{S}_{ij}^{(2)}$. The first subsection of Part VI would explain the algorithm to accomplish decomposition equation (3.22) in greater details.

An interesting analogy can be observed from equation (3.22) and equation (3.7), where $\mathcal{V}_i^{(2)}$ in equation (3.22) and $(\mathcal{X}_i^H)^{(3)}$ in equation (3.7) both serve as the projection from new basis, i.e., plane wave basis and skeletons basis, to the original DoFs, and $\mathcal{S}_{ij}^{(2)}$ in equation (3.22) serves similar purpose as the translation matrix $\mathcal{T}_{ij}^{(3)}$ in equation (3.7) does. However, they do exhibit different mathematical properties. Owning to the orthogonality of spherical harmonics, $\mathcal{T}_{ij}^{(3)}$ in equation (3.7) is a diagonal sparse matrix while the $\mathcal{S}_{ij}^{(2)}$ in equation (3.22) is dense.

For level L other than the leaf level, expansion as equation (3.22) can be calculated for each Huygens' coupling pair straight-forwardly. Consequently, one would have to calculate and store $\mathcal{V}_i^{(L)}$ for every group on each level. Instead, H-MLFMM further expands the $\mathcal{V}_i^{(L)}$ matrix as an interpolation of the two matrices $\mathcal{V}_{i,1}^{(L+1)}$ and $\mathcal{V}_{i,2}^{(L+1)}$ via mapping matrix $\mathcal{V}_i^{(L,L+1)}$. For instance, the $\mathcal{H}_{ij}^{(1)}$ matrices illustrated by green blocks in Figure.3.3(b) can be expressed as

$$\mathcal{H}_{ij}^{(1)} \approx \mathcal{V}_i^{(1)} \mathcal{S}_{ij}^{(1)} \left(\mathcal{V}_j^{(1)}\right)^T \tag{3.23}$$

where $\mathcal{V}_i^{(1)} = \begin{bmatrix} \mathcal{V}_{i,1}^{(2)} \\ \mathcal{V}_{i,2}^{(2)} \end{bmatrix} \cdot \mathcal{V}_i^{(1,2)}$. Here $\mathcal{V}_{i,1}^{(2)}$ and $\mathcal{V}_{i,2}^{(2)}$ are the mapping matrices of the two children groups of group i while $\mathcal{V}_i^{(1,2)}$ is the interpolative mapping matrix. Mathematically, it accomplishes projection from the children's skeleton basis to their parent's skeleton basis. $\mathcal{S}_{ij}^{(1)}$ denotes the dense coupling matrix between the skeleton of group i and group j at level 1. The expansion equation (3.23) can be applied recursively until it reaches the leaf level of H-MLFMM.

The remaining coupling does not satisfy $\Gamma_i^{(L)} \bigcap \Gamma_j^{(L)} = \varnothing$, they are the self-term $\mathcal{S}$ denoted by red blocks and neighboring coupling term $\mathcal{N}$ denoted by orange blocks in Figure.3.3. For each level, Huygens' coupling blocks are identified and accounted

for via equation (3.23) for levels other than leaf level and equation (3.22) for the leaf level. The remaining coupling blocks $\mathcal{S}$ and $\mathcal{N}$ in the finest level illustrated by Figure.3.3(c) are represented via the original basis functions, e.g., RWG basis, and the conventional MoM representations of such are assembled and stored explicitly.

3.4.2 Hierarchical Skeletonalization

As discussed in equation (3.23), H-MLFMM uses cascaded mapping matrices to project the skeletons to its parent in the adjacent level. A skeletonalization technique is developed to calculate matrices $\mathcal{V}_i^{(1,2)}$ for each level. Just as the leaf level $\mathcal{V}_i^{n_i \times k_i}$ matrix in equation (3.26) maps the original DoFs to its skeleton basis, $\mathcal{V}_i^{(1,2)}$ maps the skeleton basis of children level to the parent level. Thus, the algorithm applied to solve for $\mathcal{V}_i^{(2)}$ can be applied to solve for $\mathcal{V}_i^{(1,2)}$ in a recursive manner. Assume the original DoFs within group i and group j at level 1 are replaced by the union of the skeletons DoFs revealed from their children groups at level 2. Subsequently the coupling matrix $A_{ij}^{(1)}$ between group i and group j can be decomposed as follows,

$$A_{ij}^{(1)} \approx \mathcal{V}_i^{(1,2)} \mathcal{S}_{ij}^{(1,2)} (\mathcal{V}_j^{(1,2)})^T \tag{3.24}$$

where $\mathcal{V}_i^{(1,2)}$ maps the skeleton basis from children level to their counterparts at parents level. Subsequently, the original coupling matrix $A_{ij}^{(1)}$ between the group i and group j can be expressed in a telescoped manner as follows,

$$A_{ij}^{(1)} \approx \begin{bmatrix} \mathcal{V}_{i,1}^{(2)} \\ \mathcal{V}_{i,2}^{(2)} \end{bmatrix} \mathcal{V}_i^{(1,2)} \mathcal{S}_{ij}^{(1,2)} (\mathcal{V}_j^{(1,2)})^T \begin{bmatrix} (\mathcal{V}_{j,1}^{(2)})^T & (\mathcal{V}_{j,2}^{(2)})^T \end{bmatrix} \tag{3.25}$$

3.4.3 Acceleration of $\mathcal{S}_{ij}$ Assembly via Adaptive Cross Approximation

MLFMM algorithm diagonalized the translator $\mathcal{T}_{ij}$ in equation (3.7) and only one set of such translators needs to be assembled for each partition level. Unfortunately, the $\mathcal{S}_{ij}$ matrices in equation (3.22), which represent the couplings between the skeleton DoFs, have to be assembled and stored for each coupling pair. Dense as $\mathcal{S}_{ij}$ matrices are, they are generally numerically rank deficient. This is true due to the fact that coupling between group i and group j is directional in the solid angle sense, yet they are accounted for via the skeleton DoFs that are capable of representing couplings across the whole angular spectrum. The redundancy can be systematically allured through data sparsification algorithms. Specifically, herein we apply the adaptive cross approximation (ACA) algorithm [14] to accelerate the assembly of $\mathcal{S}_{ij}$ matrices and to reduce the memory consumption as well.

3.4.4 Block-diagonal Pre-conditioner based on Skeletonalization Algorithm

A suitable pre-conditioner can effectively accelerate the convergence of Krylov solvers. Block diagonal pre-conditioner, which is in essence a diagonal scaling operation, has been one of the most widely applied pre-conditioners. The implementation of this pre-conditioner usually involves direct factorization of the self term from the MLFMM, which could be expensive in the low frequency or multi-scale scenario where large numbers of DoFs may still reside in one group. An extreme case would be the one provided in the next section, where there are 131,745 DoFs per cube in average. For groups like this, an $O(N^3)$ direct factorization could be extremely expensive. In [34], we developed a fast direct solver for surface integral equations. The algorithm is

based on the skeletonalization algorithm discussed in section III as well. The performance of this direct solver can be found at Table 3.4. For details of this direct solver, readers are referred to references [35], [34].

3.5 Implementation of Skeletonalization Algorithm

One of the properties that has been widely recognized and utilized in fast integral equation algorithms is the redundancy that manifests in the interactions between well separated groups. Numerically, the coupling matrices are often rank deficient. Specifically, the discretization densities employed usually need to be quite fine in order to capture the highly oscillatory near field phenomena. However, this desired local sampling well exceeds the Nyquist rate and proves to be an over-kill for computing the far field radiations. MLFMM expands the Green's function and calculates the far field interactions in terms of plane waves. This new set of basis functions would then be aggregated and translated in a highly efficient manner to account for the far field interactions.

Another category of algorithms seek to compress the far field coupling matrix itself. For these methods, the canonical singular value decomposition (SVD) has been shown to be optimal [26] in terms of spectral radius. Nonetheless, the formidable cost of direct SVD renders the method too expansive to be a fast algorithm. Recently, there are quite a few rank-revealing algorithms that compute the effective rank and the corresponding approximate SVD within the specified tolerance without the need to fully assemble the matrices [14, 36]. The skeletonalization algorithms originally

proposed in [27] managed to express the coupling between a group and all its well-separated groups using a single set of skeleton DoFs, i.e, a reduced set of the original DoFs.

3.5.1 Skeletonalization based on Huygens' Principle

Assume the supports of group i are plotted using red triangulations, denoted by Γ_i in Figure.3.4(a). These DoFs are marked by Λ_i. The supports of Huygens' coupling groups are plotted using green triangulations and connoted by $\Gamma_{i,B}$. Then each of these Huygens' coupling blocks $\mathcal{H}_{i,j}$ can be decomposed as:

$$\mathcal{H}_{ij}^{n_i \times n_j} \approx \mathcal{V}_i^{n_i \times k_i} \mathcal{S}_{ij}^{k_i \times k_j} \left((\mathcal{V}_j)^T \right)^{k_j \times n_j} \tag{3.26}$$

where n_i, n_j are the number of unknowns in box i and box j, respectively. k_i, k_j are the corresponding numerical ranks, and moreover we also expect $k_i < n_i$ and $k_j < n_j$. This decomposition proves to be quite beneficial since $\mathcal{V}_i$ and $\mathcal{V}_j$ associate only with indexes i and j, respectively. In other words, one single set of near field skeleton basis of group i can be employed in all $\mathcal{H}_{ij}$ where $j \neq i$. Another important characteristic of equation (3.26) is that the entries of $\mathcal{S}_{ij}$ matrices are comprised of the original entries from $\mathcal{H}_{ij}$, which means that the new basis functions are a subset of the original DoFs. These new basis functions are named "skeletons" or "skeleton DoFs".

Next, a Huygens' surface Γ_a that satisfies $\Gamma_a \bigcap \Gamma_i = \emptyset$, $\Gamma_a \bigcap \Gamma_{i,B} = \emptyset$ is constructed to encapsulate Γ_i, as illustrated by the blue triangulations in Figure.3.4(b). Physically any field that can be induced on Γ_i could be equally well induced by current distributions on Γ_a by virtue of the Huygens' principle[26]. Subsequently, the

couplings between Γ_i and any DoFs outside Γ_a can be well represented via the interactions between Γ_i and Γ_a up to a prescribed tolerance ϵ, which is dependent on the mesh density on Γ_a [26].

To fully account for the couplings between Γ_i and Γ_a, electric currents $\mathbf{J}_{\Gamma_a} \in H^{-1/2}\left(div_{\Gamma}, \Gamma_a\right)$ and magnetic currents $\mathbf{M}_{\Gamma_a} \in H^{-1/2}\left(div_{\Gamma}, \Gamma_a\right)$ are both assigned to Γ_a and represented via the div-conforming RWG basis functions. Afterwards, four reaction matrices are assembled,

$$A_1^i =< \mathbf{J}, \mathbf{E}(\mathbf{J}_{\Gamma_i}) >_{\Gamma_a} \tag{3.27}$$

$$A_2^i =< \mathbf{M}, \mathbf{H}(\mathbf{J}_{\Gamma_i}) >_{\Gamma_a} \tag{3.28}$$

$$A_3^i =< \mathbf{J}, \mathbf{E}(\mathbf{J}_{\Gamma_a}) >_{\Gamma_i} \tag{3.29}$$

$$A_4^i =< \mathbf{J}, \mathbf{E}(\mathbf{M}_{\Gamma_a}) >_{\Gamma_i} \tag{3.30}$$

where $< \mathbf{J}, \mathbf{E} >_{\Gamma_a} = \int_{\Gamma_a} \mathbf{J} \cdot \mathbf{E}\, dS$, and $\mathbf{E}(\mathbf{J}_{\Gamma_a})$ and $\mathbf{E}(\mathbf{M}_{\Gamma_a})$ are the electric fields produced by the electric and magnetic currents, $\mathbf{J}_{\Gamma_a}$ and $\mathbf{M}_{\Gamma_a}$, respectively. Concatenate these 4 matrices into one single matrix A_i, one has

$$A_i = \left[\begin{array}{cccc} A_1^{i\,T} & A_2^{i\,T} & A_3^i & A_4^i \end{array} \right]^{n_i \times 4N_{\Gamma_a}} \tag{3.31}$$

where N_{Γ_a} is the number of DoFs associated with the discretization on Γ_a.

By applying a rank revealing QR decomposition [37] to equation (3.31) yields,

$$A_i^T P_R = \left[\begin{array}{cc} Q_{11} & Q_{12} \\ Q_{21} & Q_{22} \end{array} \right] \left[\begin{array}{cc} R_{11} & R_{12} \\ 0 & R_{22} \end{array} \right] = \left[\begin{array}{c} Q_{11} \\ Q_{21} \end{array} \right] \left[\begin{array}{cc} R_{11} & R_{12} \end{array} \right] + \left[\begin{array}{c} Q_{12} \\ Q_{22} \end{array} \right] \left[\begin{array}{cc} 0 & R_{22} \end{array} \right] \tag{3.32}$$

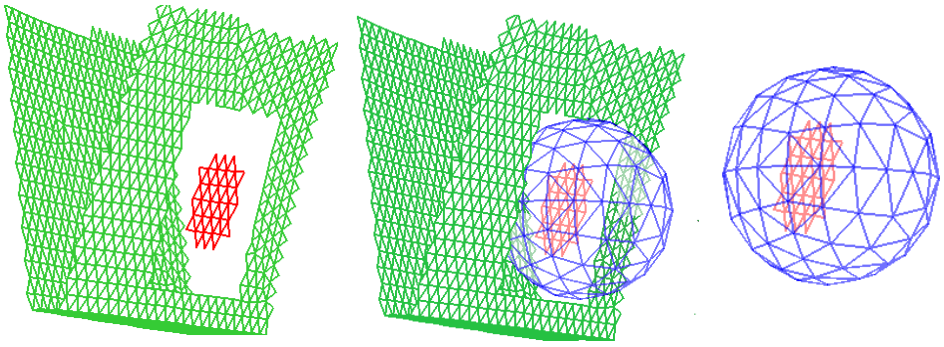

Figure 3.4: (a) Γ_i (red triangulations) as the support of group i and $\Gamma_{i,B}$ (green triangulations) as the support of its secondary neighbors (b) Γ_i and $\Gamma_{i,B}$ with the Huygens' surface Γ_a (blue triangulations) (c) Γ_i and Γ_a only

where Q_{11} and R_{11} are of size $k \times k$. Note that R_{11} is an upper triangle matrix and its diagonal entries are positive and non-increasing, then numerical rank k can be identified by looking for the first diagonal entry R_k that satisfies $\|R_k\| < \epsilon \| \cdot R_1\|$, where R_1 is the first diagonal entry of R_{11}. It can be proved [27] that $\|\sigma_1(R_{22})\| \leq \sigma_{k+1}(A_i) \cdot \sqrt{1 + k(n-k)}$, where $\sigma_1(R_{22})$ is the largest singular value of R_{22} and $\sigma_{k+1}(A_i)$ is the $(k+1)^{th}$ largest singular value of A_i. Subsequently,

$$A_i^T P_R \approx \begin{bmatrix} Q_{11} \\ Q_{21} \end{bmatrix} \begin{bmatrix} R_{11} & R_{12} \end{bmatrix} \tag{3.33}$$

where P_R is the permutation matrix produced by the QR decomposition.

$$R_{11} T = R_{12} \tag{3.34}$$

Then

$$A_i \approx P_R \begin{bmatrix} I \\ T^T \end{bmatrix} A_{RS} \tag{3.35}$$

where I is the $k \times k$ identity matrix. A_{RS} is the first k rows of $P_R^T A_i$. Consequently, DoFs that correspond to the first k_i rows of the matrix $P_R^T A_i$ constitute the skeletons

or skeleton DoFs of this group. The rest of the $(n_i - k)$ rows are linear combinations of the k skeletons and the coefficients are stored in T^T matrix. The V_i matrix is readily available, i.e.,

$$\mathcal{V}_i = P_R \begin{bmatrix} I \\ T^T \end{bmatrix} \tag{3.36}$$

Theoretically, the discretization size on Γ_a depends solely on the prescribed precision ϵ regardless of the mesh density on Γ_i. For matrix A^H in equation (3.31), the complexity of the rank revealing QR decomposition scales as $O(n_i \cdot N_{\Gamma_a} \cdot k)$, where k is the numerical rank and $k \leq min\{n_i, N_{\Gamma_a}\}$. The electrical size of the Huygens' surface is bounded by $\lambda/4$ in H-MLFMM, so N_{Γ_a} is bounded as well. Consequently, the complexity of the rank revealing QR decomposition is under control for the skeletonalization algorithm aforementioned. Another benefit of Huygens' surface allows the Huygens' couplings $\mathcal{H}$ between any two groups to be accounted for directly as long as their DoFs reside completely outside one another's Huygens' surface, even if they are from different partition levels.

We note that the shape of Γ_a is largely irrelevant as long as it satisfies $\Gamma_a \bigcap \Gamma_i = \emptyset$ and $\Gamma_a \bigcap \Gamma_{i,B} = \emptyset$. Practically, a desirable design of Γ_a should be the one with the maximum dimension that doesn't violate $\Gamma_a \bigcap \Gamma_{i,B} = \emptyset$, simply because the Huygens' surface is only designed to capture the couplings with its secondary neighbor groups that does not intersect with its Huygens' surface. Note that Γ cannot intersect the group DoFs, nor is it allowed to intersect its secondary neighbor DoFs. One convenient approach involves constructing a sphere as Γ_a, whose radius r_{Γ_a} is the maximum distance from the group center to its closest secondary neighbor DoF. This sphere is then discretized according to the precision requirement and basis functions are assigned. Practically, since $r_{\Gamma_a} \leq \lambda/4$, namely the size of the leaf level group

from conventional MLFMM, r_{Γ_a} is assigned in such a way such that the discretized geometrical description of Γ_a will not intersect the DoFs within the group and its secondary neighbor DoFs. We choose to use 150 triangles to discretize Γ_a for all the examples shown in this work, which gives to 300 basis function for $\mathbf{J_{\Gamma_a}}$ and $\mathbf{M_{\Gamma_a}}$, respectively. Consequently, h_{Γ_a} is typically much less than 0.1λ and thus the accuracy of the algorithm would only depend on the prescribed accuracy from the skeletonalization algorithm. It is worth pointing out that the skeletonalization process of different groups are completely independent and thus can be executed in a highly parallelized manner. For more details of the skeletonalization algorithm, references [26][27] [35][34] could be helpful.

3.6 Numerical Results

In this section, we study the error controllability and performance of the proposed H-MLFMM algorithm. The error controllability of H-MLFMM is investigated through some canonical as well as complex targets. Whereas the scalability and accuracy of the algorithm would be demonstrated by means of a set of experiments. QR tolerance of 10^{-3} and double precision are assumed unless otherwise specified. Furthermore, we employ the combined field integral equation (CFIE) with $\alpha = 0.5$ for our studies herein.

3.6.1 Error Controllability Study

To assess the error controllability of the proposed H-MLFMM, matrix-vector multiplication (MVM) errors ϵ_m are calculated for various targets,

$$\epsilon_m = \frac{||ZI - \tilde{Z}I||}{||ZI||} \tag{3.37}$$

where Z denotes the impedance representation from MLFMM, $\tilde{Z}$ is the impedance representation from H-MLFMM and I is the input current vector. $||\cdot||$ denotes the 2-norm. Huygens' theorem states that any field that can be induced on Γ_i could be equally well induced by current distributions on Γ_a [26]. The previous sections have elucidated a systematic analysis on the parameters of the Huygens' surface and provide a guideline for general construction of the Huygens' surface. The following experiments demonstrates that the error is kept under control for this implementation.

First example is a PEC cone-sphere shown in [12] at 1800 MHz, MVM error from 6 level H-MLFMM are calculated against that from 4 level MLFMM. Then a $3m \times 3m \times 3m$ PEC cube is calculated at 100MHz, for this example 3 level H-MLFMM is adopted, while 2 level MLFMM is used as reference. For a more sophisticated model, part of a PEC aircraft platform as shown in Figure.3.5 at 200MHz is calculated using 6 level H-MLFMM and 4 level MLFMM, respectively. $\varepsilon = 10^{-3}$ tolerance is adopted. As mentioned in section 5.1, 150 triangles are employed to discretize Γ_a, which gives rise to 300 basis functions for $\mathbf{J_{\Gamma_a}}$ and $\mathbf{M_{\Gamma_a}}$, respectively. For each of the three aforementioned cases, 30 sets of i.i.d. complex vectors are randomly generated and the error calculations are performed afterwards, the maximum results are listed in Table 3.1. It can be observed that the MVM errors of all 3 examples are kept under the the tolerance adopted in the QR decomposition.

3.6.2 Scalability Study

Having established the error controllability of H-MLFMM, we continue to conduct a series of experiments to illustrate the scalability of H-MLFMM from several aspects.

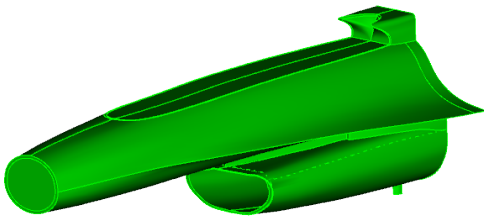

Figure 3.5: Part of a mock-up aircraft

Table 3.1: MVM Error

example	DoFs.	DoFs per MLFMM leaf cube	DoFs per H-MLFMM leaf cube	ϵ_m
cone-sphere	58,764	408	27	2.42×10^{-4}
cube	18,648	333	63	3.61×10^{-4}
aircraft part	146,265	504	26	4.95×10^{-4}

Fixed mesh size complexity study

We intend to study the scalability of the H-MLFMM under constant mesh size. For this study, $kh = 10^{-2}\pi$ is used to discretize a series of PEC spheres whose radius are listed in the first column of Table 3.2. CPU time consumed by skeletonalized algorithm(S.A.) and S_{ij} assembly are listed together with peak memory consumption. They are calculated using H-MLFMM with tolerance $\varepsilon = 10^{-3}$ at 15MHz. The memory and CPU time per iteration statistics are presented in Table 3.2. The memory scales as $O(N)$ while $O(N)$ scalability is also observed from Figure.3.7 for CPU time per iteration, at least for the sphere example.

Table 3.2: Computational statistics for fixed mesh size problems

radius (λ)	DoFs	DoFs per leaf cube	Setup Memory(MB)	Setup CPU time(s) S.A.	Setup CPU time(s) S_{ij}	CPU time per MVM (s)
0.100	18,291	16	402	27	57	5.26×10^{-2}
0.150	41,415	36	930	52	105	1.32×10^{-1}
0.200	74,169	16	1,715	115	239	3.21×10^{-1}
0.225	93,873	21	2,151	137	291	3.73×10^{-1}
0.250	116,253	26	2,606	161	339	4.82×10^{-1}
0.275	141,063	31	3,166	188	385	5.51×10^{-1}
0.400	298,863	17	6,773	480	902	1.28×10^{0}
0.800	1,183,665	17	26,883	2,233	3,406	5.28×10^{0}

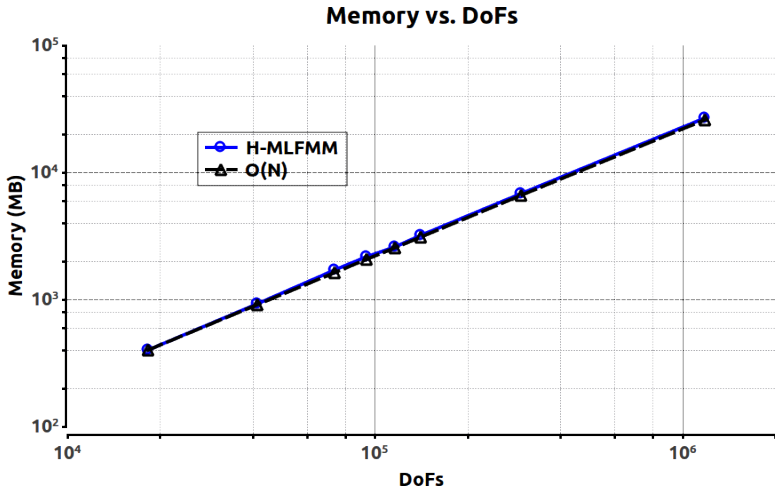

Figure 3.6: Complexity of memory consumption for fixed mesh size problems

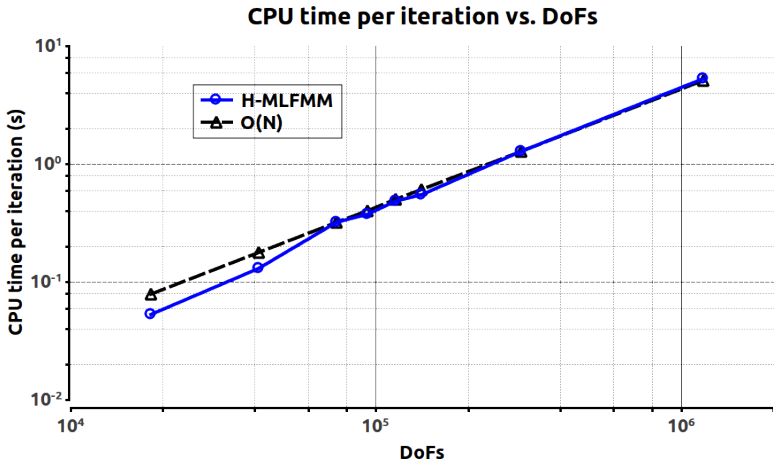

Figure 3.7: Complexity of CPU time for fixed mesh size problems

Fuselage structure

We intend to demonstrate the wide band simulation capability offered by H-MLFMM. EM response from 1MHz up to 8GHz are calculated based on one single mesh. The object adopted for this set of experiments is shown in Figure.3.8, where computational adversaries such as cavity, sharp corners, etc. are presented in this geometry. For the frequency range from 1,000MHz up to 8,000MHz, straight-forward automatic surface refinement helps to keep the mesh size $h \approx 0.1\lambda$. i.e., $kh \approx 0.2\pi$, where k is the wave number. For the remaining frequency range lower than 1000MHz down to 1MHz, the mesh at 1000MHz is adopted in all cases. Positive Z polarized plane wave impinges upon the target along positive X direction, i.e, propagates towards the intake. Table 3.4 shows the memory consumption for setup stage and pre-conditioner, respectively. $\varepsilon = 10^{-3}$ tolerance is adopted for all cases. For frequency under 125MHz, the memory requirement of MLFMM exceeds the hardware

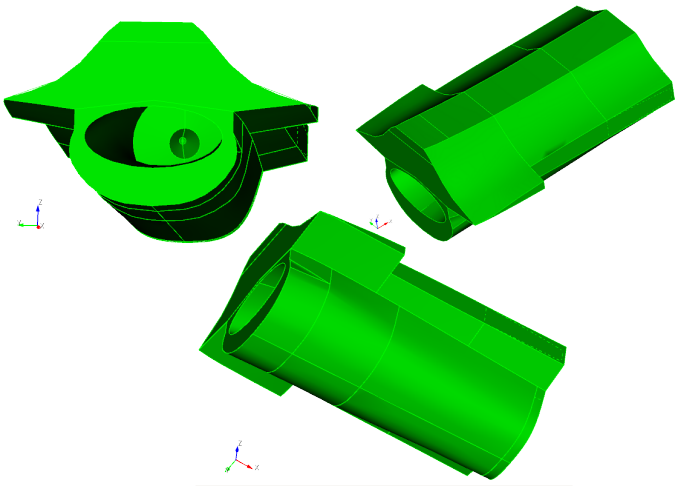

Figure 3.8: Front, top and bottom view of central fuselage part of an aircraft model

resources available to us, and therefore, the memory requirements for those frequencies shown in Table 3.4 are estimated and printed in bold italic font. CPU time for near field assembly and each MVM operation are shown in Table 3.5 and 3.6 where results for frequency lower than 125MHz are unavailable for MLFMM. On the Krylov solver side we adopt Generalized Conjugate Residual (GCR) [38] algorithm with 30 restart and converged with the relative residual smaller than 10^{-2}.

The computational parameters from the frequency band from 1MHz to 8,000MHz are listed in Table 3.3. Note the difference in average DoFs per leaf level between H-MLFMM and MLFMM at low frequencies.

Based on the statistics from Table 3.4, Table 3.5 and Table 3.6 , we plot the scaling curves for memory consumption in Figure.3.9 and CPU time per MVM operation in Figure.3.10, on log-log scale, where N is the number of DoFs. Note that the memory scalability curve of H-MLFMM matches up with that of MLFMM for the $hk = 0.2\pi$ spectrum and no significant reduction in CPU time and memory consumption is

Table 3.3: Computational Parameters

Freq. (MHz)	hk	DoFs	DoFs per MLFMM leaf cube	DoFs per H-MLFMM leaf cube
8,000	0.2π	8,350,452	9	9
4,000	0.2π	2,087,613	9	9
2,000	0.2π	529,827	9	9
1,000	0.2π	131,745	9	9
500	0.1π	131,745	38	9
250	0.05π	131,745	156	9
125	0.025π	131,745	813	9
60	0.012π	131,745	4,392	9
30	0.006π	131,745	32,936	9
15	0.003π	131,745	32,936	9
1	0.0002π	131,745	131,745	9

observed, this is due to the reason that H-MLFMM automatically degenerates to conventional MLFMM under these discretization scenarios, where the number of DoFs per leaf level group in conventional MLFMM is less than 50. At the low frequency end, memory consumption for both algorithms approach constants as expected. However, the constant is much smaller for the H-MLFMM than the MLFMM.

The incorporation of ACA accelerates the assembly of $\mathcal{A}_{ij}$ matrices and reduces the memory consumption, as shown in Table 3.7. The ACA tolerance is set to 10^{-3}. Looking at the data from Table 3.4 at the low frequency spectrum, we have observed significant data compression using the ACA algorithm.

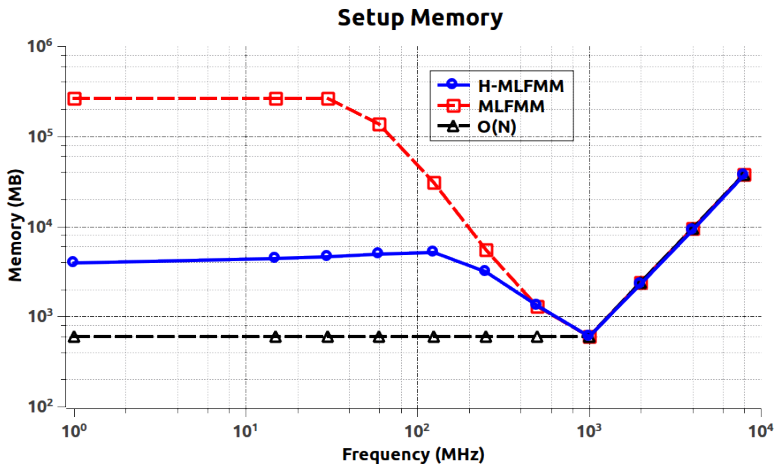

Figure 3.9: Complexity comparison of memory consumption, H-MLFMM vs. MLFMM. 1MHz–1GHz, N is constant. 1GHz– 8GHz, $N \propto f$

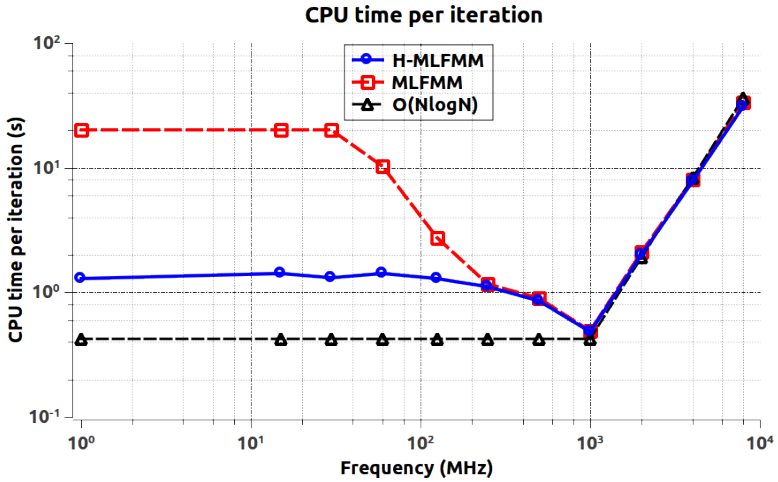

Figure 3.10: Complexity comparison of CPU time per MVM, H-MLFMM vs. MLFMM. 1MHz–1GHz, N is constant. 1GHz – 8GHz, $N \propto f$

Table 3.4: Memory Statistics

Freq.	Setup Memory(MB)		Pre-cond. Memory(MB)	
(MHz)	MLFMM	H-MLFMM	MLFMM	H-MLFMM
8,000MHz	37,910	36,339	1,390	1,390
4,000MHz	9,423	8,940	348	348
2,000MHz	2,399	2,273	91	91
1,000MHz	598	568	22	22
500MHz	1,281	1,146	91	91
250MHz	5,529	5,310	400	400
125MHz	30,737	21,468	1,993	1,993
60MHz	***134,976***	15,683	***12,502***	4,078
30MHz	***264,845***	12,036	***66,390***	4,953
15MHz	***264,845***	11,081	***66,390***	4,820
1MHz	***264,845***	9,321	***66,390***	4,761

Table 3.5: CPU Time Statistics from 1GHz to 8GHz

Freq.	Near field (s)		CPU time per MVM (s)	
(MHz)	MLFMM	H-MLFMM	MLFMM	H-MLFMM
8,000MHz	1,206	1,201	33.20	31.02
4,000MHz	302	302	8.32	7.79
2,000MHz	170	172	2.10	2.01
1,000MHz	26	27	0.49	0.48

To examine the accuracy of the far field, we define the far field difference ϵ_f as follows:

Table 3.6: CPU Time Statistics from 1MHz to 500MHz

Freq.	Near field(s)			CPU time per MVM (s)	
(MHz)	MLFMM	H-MLFMM		MLFMM	H-MLFMM
		S.A.	S_{ij}		
500MHz	60	65	49	0.90	0.85
250MHz	317	126	303	1.17	1.10
125MHz	1,845	193	1,031	2.72	1.28
60MHz	***8,162***	225	832	***10.23***	1.41
30MHz	***16,051***	244	682	***19.98***	1.31
15MHz	***16,051***	241	632	***19.98***	1.41
1MHz	***16,051***	235	530	***19.98***	1.28

Table 3.7: Memory Statistics of H-MLFMM with ACA

Freq.	Setup Memory(MB)		
(MHz)	MLFMM	H-MLFMM	H-MLFMM + ACA
250MHz	5,529	5,310	3,371
125MHz	30,737	21,468	6,516
60MHz	***134,976***	15,683	5,847
30MHz	***264,845***	12,036	5.628
15MHz	***264,845***	11,081	5,335
1MHz	***264,845***	9,321	4,698

$$\epsilon_f = \frac{\sqrt{\sum_{\theta,\phi} |\tilde{\mathbf{E}} - \mathbf{E}|^2}}{\sqrt{\sum_{\theta,\phi} |\mathbf{E}|^2}} \tag{3.38}$$

Table 3.8: CPU Statistics of H-MLFMM with ACA

Freq.	Setup CPU Time(s)				
(MHz)	MLFMM	H-MLFMM		H-MLFMM+ACA	
		S.A.	S_{ij}	S.A.	S_{ij}
250MHz	317	126	303	126	137
125MHz	1,845	193	1,031	193	305
60MHz	***8,162***	225	832	225	312
30MHz	***16,051***	244	682	244	301
15MHz	***16,051***	241	632	241	289
1MHz	***16,051***	235	530	235	273

where $\tilde{\mathbf{E}}$ is the far field results calculated from H-MLFMM, and $\mathbf{E}$ is computed using MLFMM. Real part of both solutions are plotted side-by-side in Figure.3.12, Figure.3.14 and Figure.3.16.

Results of far fields computed using both H-MLFMM and MLFMM with different discretization sizes are shown in Figure. 3.11, Figure. 3.13 and Figure. 3.15. As evidenced from these plots, the results computed using these two algorithms agree well with each other.

To validate the accuracy of the H-MLFMM at low frequency with very small discretization size, we apply MLFMM to the same object, as shown in Fig 3.8, using a different discretization size, namely $hk = 0.01\pi$. The result computed using MLFMM is used as a reference to compare against the result from the proposed H-MLFMM algorithm with a much finer discretization size. For the far field patterns, it can be seen from Figure. 3.17 very good agreement between these two results. However,

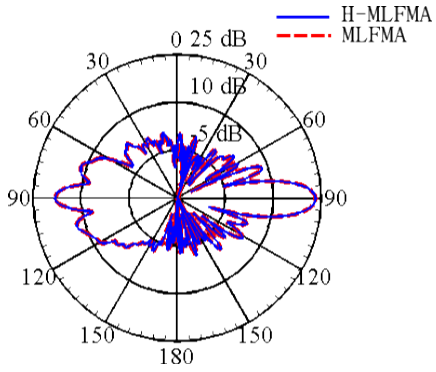

Figure 3.11: Far field of H-MLFMM vs. MLFMM on $\phi = 0^o$ plane at 1000MHz

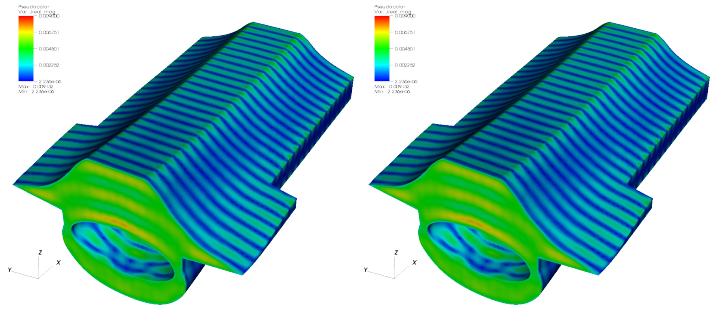

Figure 3.12: Real part of current at 1GHz (a)H-MLFMM (b)MLFMM

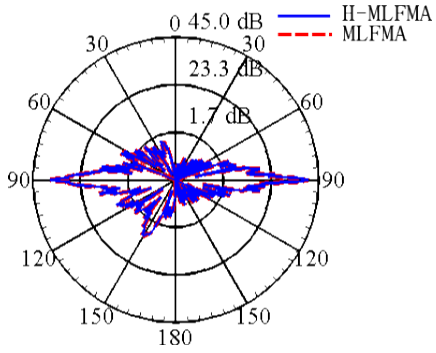

Figure 3.13: Far field of H-MLFMM vs. MLFMM on $\phi = 0^o$ plane at 8000MHz

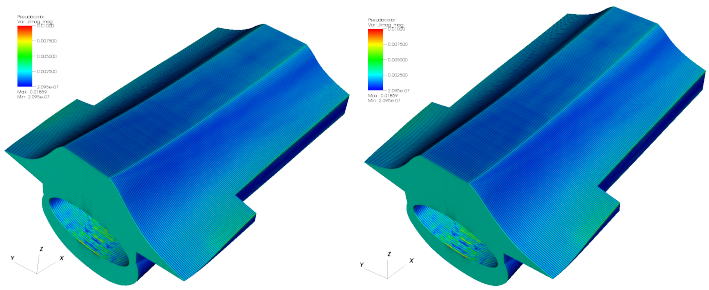

Figure 3.14: Real part of current at 8GHz (a)H-MLFMM (b)MLFMM

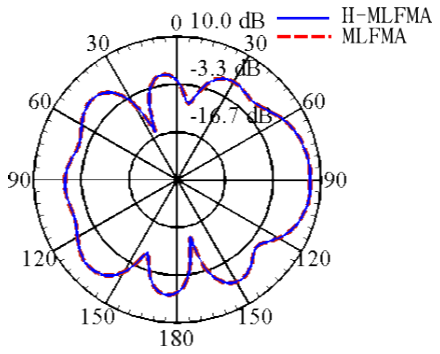

Figure 3.15: Far field of H-MLFMM vs. MLFMM on $\phi = 0^o$ plane at 125MHz

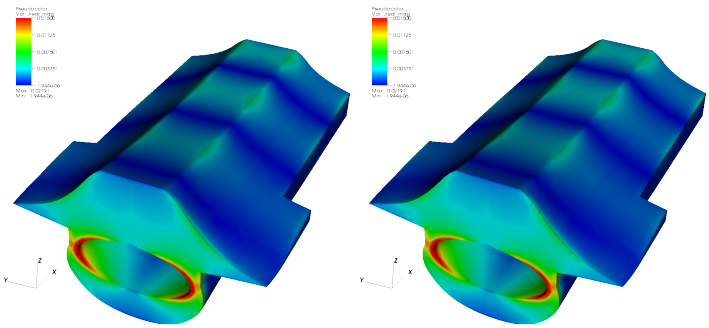

Figure 3.16: Real part of current at 125MHz (a)H-MLFMM (b)MLFMM

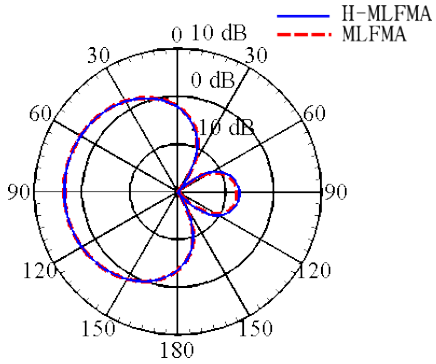

Figure 3.17: Far field comparison of $hk = 0.003\pi$ using H-MLFMM and $hk = 0.01\pi$ using MLFMM on $\phi = 0^o$ plane at 15MHz

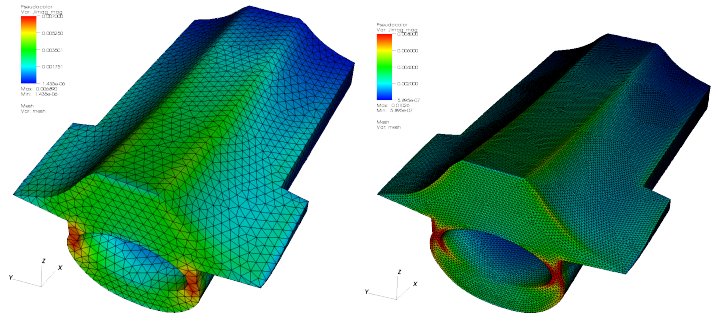

Figure 3.18: Imaginary part of current at 15MHz (a)$hk = 0.01\pi$ (b)$hk = 0.003\pi$

there are noticeable differences in the near field distributions between these numerical results. Some subtle and fine features in the near field distribution can be observed from the result obtained using the much finer discretization, $hk = 0.003\pi$, by the H-MLFMM. Furthermore, a closer look at the local field distribution near the intake is provided in Figure. 3.19.

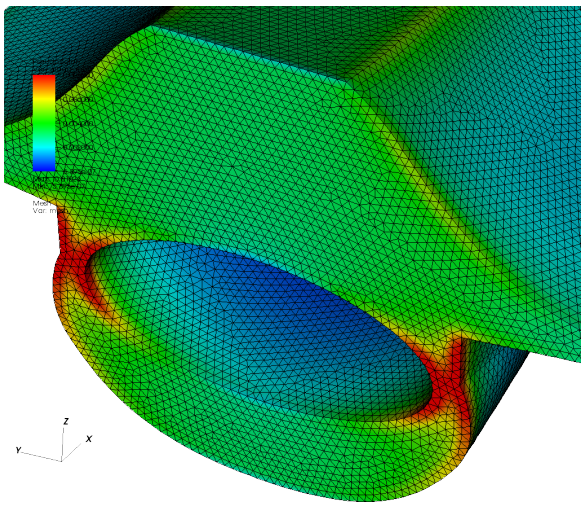

Figure 3.19: A zoom-in view of Figure.3.18(b)

3.6.3 Mock-up aircraft

For this example, a mock-up PEC aircraft model is illuminated by a y-polarized plane wave propagating from nose direction at 0.5MHz. The average mesh size of the geometry is $10^{-4}\lambda$ at 0.5MHz, resulting in 242,778 unknowns. Conventional MLFMM, without low frequency treatments, would require 899.4 GB memory and 21 hours. The H-MLFMM without the aid of ACA takes 15.4 GB and 23 minutes. The application of the ACA algorithm further reduces the computational resources to 8.8 GB in memory and 16 minutes in CPU time. Figure. 3.20 plots the real part of the electric current as well as a zoom-in view to highlight very small elements locally.

3.6.4 Circuit Board

The last example is a PEC circuit board model, discretized with 69,870 DoFs, which is illuminated by a z-polarized plane wave at 10GHz from negative x direction.

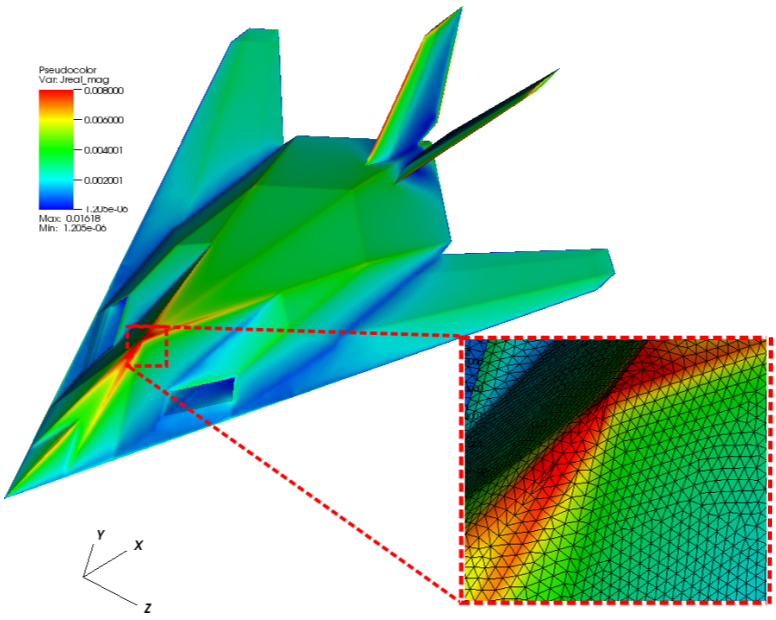

Figure 3.20: Real part of the electric current on a mock-up aircraft at 0.5MHz

The average mesh size is $h = 10^{-3}\lambda$. Finer elements are adopted to describe the geometrical details while coarser elements are employed to discretize the part of the geometry that is smooth. The ratio between the maximum and the minimum sizes of the triangles is 164. Conventional MLFMM requires 74.5 GB memory while H-MLFMM takes 2.2 GB. The electric current distribution on the circuit board is shown in Figure. 3.21 on logarithmic scale.

3.6.5 Monopole antenna radiation problem in the presence of mock-up aircraft

As shown in the previous mock-up aircraft example, H-MLFMM enables the simulation within a wide spectrum using only the mesh that is adequate at the highest frequency. In this example, the objective is to simulate the electromagnetic interference between 10 antennae, including a Vivaldi antenna array, in the presence of a

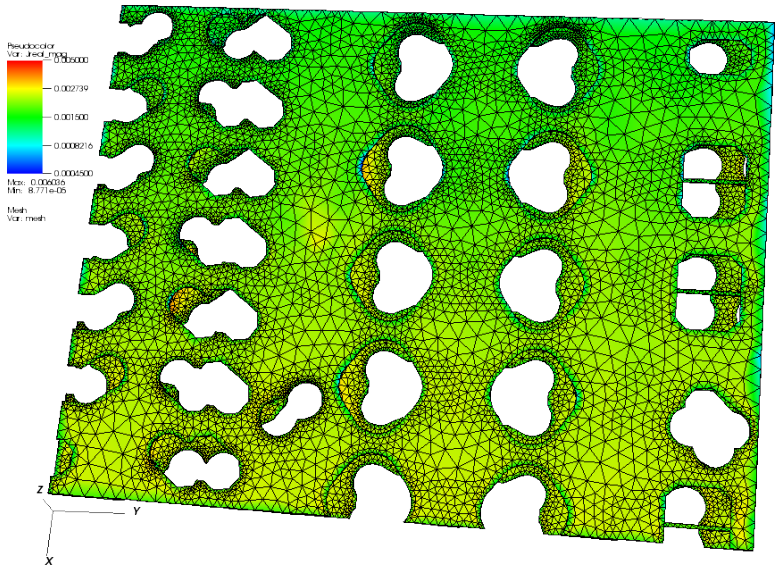

Figure 3.21: Real part of the electric current on a circuit board at 10GHz in logarithmic scale

mock-up aircraft from 75MHz up to 18GHz using only the mesh obtained at 3GHz. For the frequency band from 3GHz to 18GHz, the mesh can be adaptively refined to accommodate the frequency of interest and this is out of the scope of this work. We mainly focuse on the low frequency and multi-scale problems. These problems deteriorates as the ratio of mesh size and wavelength decreases and we would solve this problem at the low frequency end, specifically, we are interested in the electromagnetic interference of a monopole antenna radiating in the presence of a mock-up aircraft platform at 75MHz as shown in Figure.3.22 using the mesh obtained at 3GHz, in other words, the average mesh size at 75MHz is 0.0025λ.

The mock-up aircraft is decomposed into 53 PEC domains and 25 composite domains with 3,723,921 surface unknowns in total. For the dielectrics composite material on 10 antennae and 25 sub-domains from the aircraft, the recently developed

Table 3.9: Problem Configuration

Region	Material Type	No. of Domains	No. of Surface DoFs	Sub-domain Solver
aircraft	P.E.C.	53	3,098,568	H-MLFMM
aircraft	dielectric	25	504,336	GCFIE+H-MLFMM
antenna	PEC+dielectric	10	121,017	GCFIE+H-MLFMM

generalized combined field integral equation (GCFIE) [39] is adopted as the sub-domain solver. Note that H-MLFMM concept is also implemented in the GCFIE solver as well. Detailed configuration of domains are listed in Table.3.9.

The simulation is carried out under the MS-DDM scheme[40] using $1. \times 10^{-3}$ as sub-domain convergence tolerance as $1. \times 10^{-2}$ for the global residual. The real part of the electric current is plotted in Figure.3.23 in log scale from $1. \times 10^{-6}$ to $1. \times 10^{-1}$. Figure.3.24 demonstrates the current distribution in the vicinity of the aircraft more closely. Note that the dielectric radome is not shown in this figure to demonstrate the current distribution on the Vivaldi array installed on the nose of the aircraft.

One of the most concerned issue in this EMC problem is the interference inflict to other 9 antennae due to the radiation of the monopole antenna. Table.3.10 shows the S21 received by the other 9 antennae. Note that the S21 from the first antenna unit is sampled and presented for monopole array and Vivaldi array. The second column of Table.3.10 gives the designed working frequency for each of these antennae.

The computational statistics are presented in terms of sub-domain solver and coupling, respectively. In Table.3.11, peak memory requirement for the sub-domain

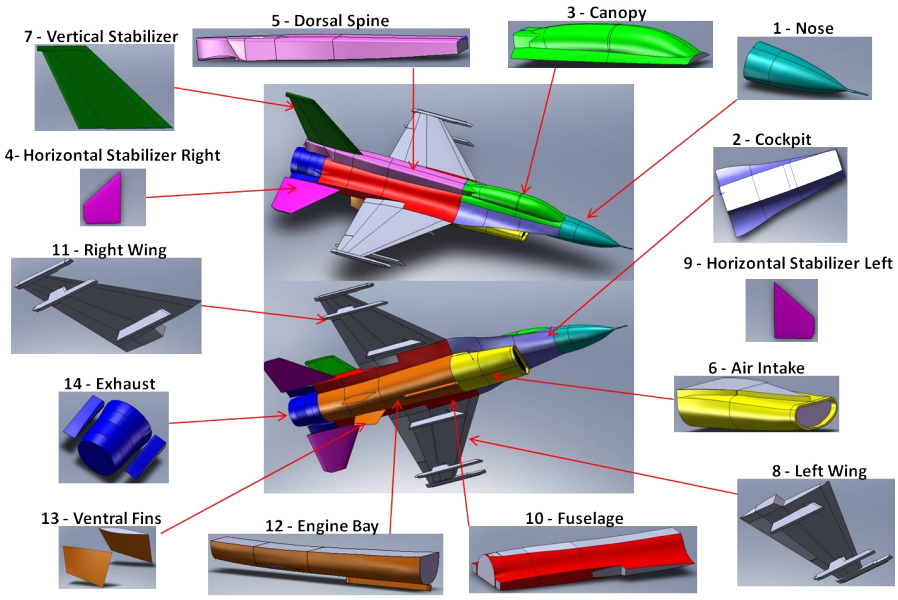

Figure 3.22: Mock-up aircraft partition

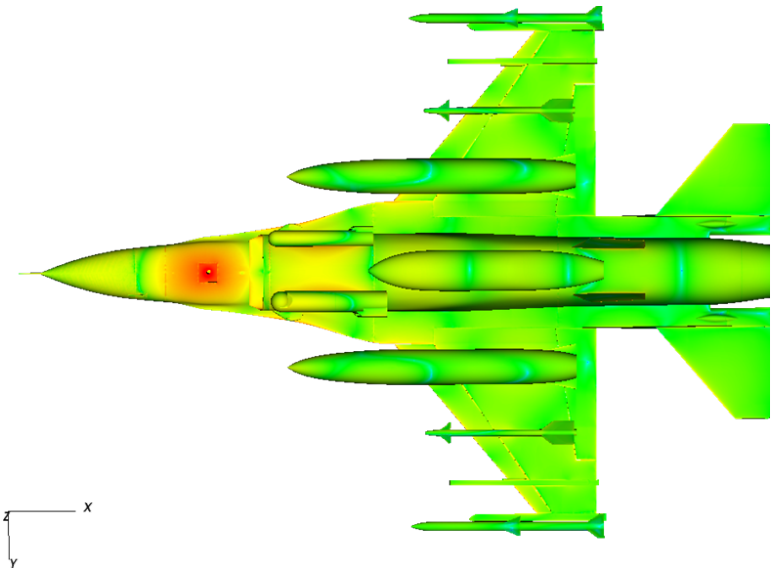

Figure 3.23: Real part of current for EMC simulation at 75MHz in log scale

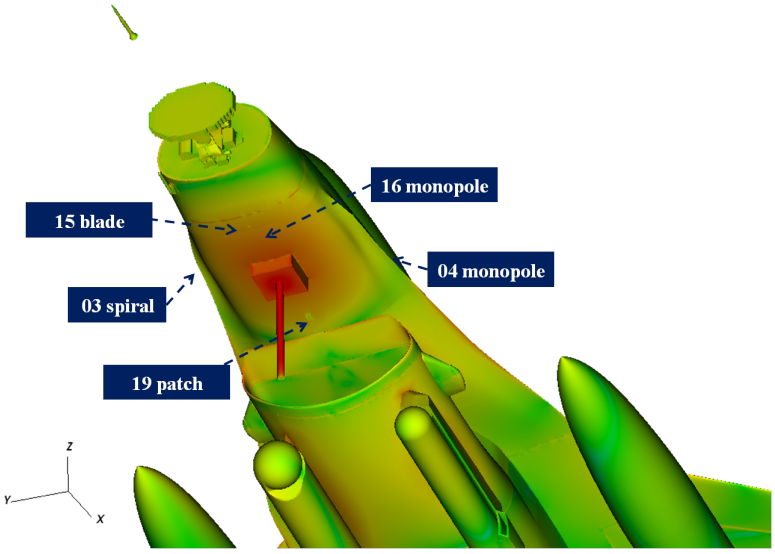

Figure 3.24: Real part of current for EMC simulation at 75MHz in log scale

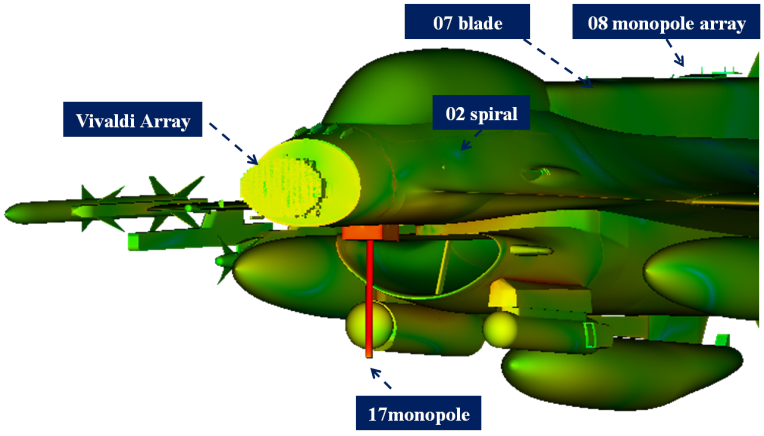

Figure 3.25: Real part of current for EMC simulation at 75MHz in log scale

Table 3.10: S21 Results

Antenna type	Designed frequency(MHz)	S21 (dB)
02spiral	10,000	1.00×10^{-5}
03spiral	9,000	1.26×10^{-5}
04monopole	1,089	5.57×10^{-5}
07blade	1,600	1.38×10^{-5}
08monopole array	1,575	2.55×10^{-5}
15blade	2,000	1.65×10^{-5}
16monopole	18,000	3.90×10^{-5}
19patch	4,250	1.34×10^{-4}
Vivaldi array	10,000	9.50×10^{-7}

Table 3.11: Computational Statistics for Sub-domain Solvers

	1^{st} iteration	non-1^{st} iteratoin
Peak memory	43 GB	43 GB
CPU time per MS-DDM iteration	150 hr	11 hr
Hard disk	380 GB	380 GB

solvers in both 1^{st} iteration and non-1^{st} are presented. Note that 1^{st} iteration consumes significantly more CPU time due to the skeletonalization process. The iterations afterwards can recycle the skeleton data without re-evaluating the skeleton.

Table 3.12: Memory requirement comparison of MLFMM and H-MLFMM

Sub-domain	No. of DoFs	MLFMM	H-MLFMM
CenterFuselage	467,955	1,699 GB	43 GB
AftFuselage	337,368	863 GB	30 GB
IntakeFrame	205,431	644 GB	19 GB

To demonstrate the performance of H-MLFMM, we digest 3 of the most computationally intensive sub-domains and list the memory requirements using convention MLFMM and H-MLFMM in Table.3.12.

3.7 Conclusion

In this chapter, we propose the H-MLFMM algorithm for surface integral equation method for solving low frequency and multi-scale electromagnetic problems. H-MLFMM alleviates the sub-wavelength breakdown problem of conventional MLFMM by compressing the near field matrix and near to far mapping matrices via their skeleton DoFs, respectively. Particularly, Huygens' principle is exploited to expedite the skeletonalization process in an error controllable fashion. Additionally, we employ the ACA algorithm to further reduce the needed computational resources. Numerical results demonstrate that H-MLFMM is error controllable and robust within a wide range of spectrum.

Chapter 4: Multi-trace Integral Equation Discontinuous Galerkin Method

A discontinuous Galerkin surface integral equation method (IEDG)[41] is proposed for electromagnetic responses from composite targets. Conventional surface integral equation methods typically employ div-conforming basis functions, e.g, RWG basis functions, for both trial and testing functions. Consequently, the algorithms are closely associated with the discretization scheme, making the mixing of multiple types of basis functions difficult. Some work has been done in this attempt. [42] develops a meshless scheme for solving surface integral equations. [43] proposed a *generalized method of moment* based on the *partition of unity* approach. Formulations of both of these methods entails the evaluation of strongly singular and hyper-singular integrals[44][45][46][47][48]. It should be pointed out that as electric current and magnetic current belongs to the div-conforming functions space, this is the tightest function space to solve for the solution. Basis functions from function spaces that include div-conforming space as a sub-space, e.g., L^2 functions space [49], can also be employed.

Discontinuous Galerkin methods [50][51] proposed another appealing approach to solve partial differential equations on finite non-conformal discretizations. It was

later on extended from time-domain Maxwell equations to frequency-domain equations[52][53]. The requirement of basis functions are greatly relaxed since the tangential continuity of electric and magnetic field are weakly enforced[52]. The IEDG algorithm is inspired by this methodology and allows the conventional combined field integral equation (CFIE) to be implemented with square-integrable L^2 basis function. Since the L^2 basis functions are defined locally, non-conformal mesh can be employed to discretize the target based on the local geometrical features. Moreover, basis functions of different orders can be applied to different elements based on the same mesh. In other words, IEDG is highly flexible for *hp*-refinement. Not only does IEDG brings about the aforementioned flexibility to the problem setup stage, it also allows the magnetic field integral equation (MFIE) to be tested in such a way that dual pairing principle is obeyed.

The electromagnetic problems demonstrated in the previous chapters mainly involves free space Green's function after applying surface equivalence principle to the original problem. Another class of widely encountered problems involves the analysis of EM responses from a target in the presence of a infinite PEC or PMC ground plane. In this chapter, we applied the image theory to the Green's functions of IEDG formulation to account for the infinite ground plane effect. First, we will briefly introduce the IEDG formulation. The IEDG formulation with infinite PEC ground plane effect will be presented. Numerical experiments from both scattering and radiation problem demonstrates the effectiveness of the algorithm.

4.1 General Galerkin Weak Statement

Here we start by inheriting the notation and operator definition from Chapter 2. The surface of the target is first discretized by a union of non-overlapping elements $S_i, i = 1, ..., N$ and $\partial\Omega_s = S_1 \bigcup S_2 \cdots \bigcup S_N$. Physics points out that the smoothness requirement for electric current $\mathbf{J}$ should be normal continuous. Consequently, the trial function needs to be div-conforming at most [54]. IEDG relaxes this requirement by elevating the function space of $\mathbf{J}$ from div-conforming to L^2 space, i.e., $\mathbf{J}(\mathbf{r}) = \sum_{m=1}^{N} \mathbf{j}_m(\mathbf{r})$, where $\mathbf{j}_m(\mathbf{r})$ is the local basis function adopted by each element. Consequently, each basis function is completely defined on one single element. No continuity requirement is enforced in the basis function definition, allowing non-conformal discretization on $\partial\Omega_s$. The normal continuity requirement will be considered later on in the form of a penalty term. Next we define the contour boundaries between two adjacent elements S_1 and S_2 are depicted in Figure.4.1, where C_{21} is the contour line on S_2 with outpointing unit vector $\hat{t}_{21}$ and C_{12} is the contour on S_1 with outpointing unit vector $\hat{t}_{12}$.

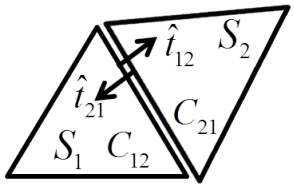

Figure 4.1: Illustration of the boundary value problem

4.1.1 Electric Field Integral Equation and Penalty Terms

The conventional EFIE resulted in the following equation on each element after $\partial\Omega_s$ is discretized in to N elements:

$$\mathbf{e}_m^{inc} = -\sum_n \pi_t \mathcal{L}(\mathbf{j}_n) \quad on\ S_m \tag{4.1}$$

Penalty methods replaces this constraint problem by a unconstrained problems by defining a surface residual term associated with equation(4.1) element m as:

$$\mathcal{R}_m^{(1)} = \mathbf{e}_m^{inc} + \sum_n \pi_t \mathcal{L}(\mathbf{j}_n) \qquad \text{on } S_m \tag{4.2}$$

Physically this residual term can be interpreted as the error tangential electric field on S_m. Based on the proper dual pairing theorem, $\mathcal{R}_m^{(1)}$ should be tested by a div-conforming test function $\mathbf{v}_m \in W_m$, which is the same functions space used to expand $\mathbf{j}_m$. The surface penalty term for any given $\mathbf{m}$ reads,

$$\langle \mathbf{v}_m, \mathcal{R}_m^{(1)} \rangle_{S_m} = \langle \mathbf{v}_m, \mathbf{e}_m^{inc} \rangle_{S_m} + \langle \mathbf{v}_m \sum_n \pi_t \mathcal{L}(\mathbf{j}_n) \rangle_{S_m} \tag{4.3}$$

where the reaction integral is defined as

$$\langle \mathbf{v}, \mathbf{u} \rangle_{S_m} = \int_{S_m} (\mathbf{v} \cdot \mathbf{u}) dS \tag{4.4}$$

We further expand equation(4.3) using the vector potential and scalar potential form as follows,

$$\begin{aligned} \langle \mathbf{v}, \mathbf{u} \rangle_{S_m} = \langle \mathbf{v}_m, \mathbf{e}_m^{inc} \rangle_{S_m} + \imath k \sum_n \langle \mathbf{v}_m, \pi_t(\Phi_A(\mathbf{j}_n)) \rangle_{S_m} \\ - \frac{1}{\imath k} \sum_n \langle \mathbf{v}_m, \pi_t(\bigtriangledown \bigtriangledown \cdot \Phi_A(\mathbf{j}_n)) \rangle_{S_m} \end{aligned} \tag{4.5}$$

where $\Phi_A(\mathbf{f})(\mathbf{r}) = \int_{\partial\Omega} \mathbf{f}(\mathbf{r}') G(\mathbf{r}, \mathbf{r}') d\mathbf{r}'$.

Instead of evaluating the last term of equation(4.5), which involves a hyper-singular integral, a common practice is to perform integration by parts and reduce the order of singularity as follows,

$$\begin{aligned}
&\sum_n \langle \mathbf{v}_m, \pi_t(\bigtriangledown \bigtriangledown \cdot \Phi_A(\mathbf{j}_n))\rangle_{S_m} \\
=&-\sum_n \langle \bigtriangledown \cdot \mathbf{v}_m, \Phi_F(\bigtriangledown' \cdot \mathbf{j}_n)\rangle_{S_m} \\
&+\sum_n \langle \hat{t}_m \cdot \mathbf{v}_m, \Phi_F(\bigtriangledown' \cdot \mathbf{j}_n)\rangle_{C_m} \\
&+\sum_{C_n} \langle \bigtriangledown \cdot \mathbf{v}_m, \Phi_F(\hat{\mathbf{t}}_n \cdot \mathbf{j}_n)\rangle_{S_m} \\
&+\sum_{C_n} \langle \hat{t}_m \cdot \mathbf{v}_m, \Phi_F(\hat{\mathbf{t}}_n \cdot \mathbf{j}_n)\rangle_{C_m}
\end{aligned} \tag{4.6}$$

where C_m denotes all the line contours of elements S_m and the single layer scalar potential is defined as $\Phi_F(\mathbf{f}(\mathbf{r})) = \int_S \mathbf{f}(\mathbf{r}')G(\mathbf{r},\mathbf{r}')dS$

4.1.2 Magnetic Field Integral Equation

Apply the Galerkin scheme to the MFIE in chapter 2, a residual can be defined for each current on element S_m,

$$\mathcal{R}_m^{(2)} := \eta(\mathbf{j}_m^{inc} + \frac{1}{2}\mathbf{j}_m + \sum_n \pi^{\times}\mathcal{K}(\mathbf{j}_n)) \qquad \text{on } S_m \tag{4.7}$$

where η denotes the relative wave impedance. This residual can be interpreted as the error electric field on S_m after the introduction of relative wave impedance. This residual is then tested with div-conforming testing function $\mathbf{v}_m$ in $\mathbf{W}_m$, forming the following reaction term,

$$\begin{aligned}
\langle \mathbf{v}, \mathcal{R}_m^2 \rangle_{S_m} =& \langle \mathbf{v}_m, \eta \mathbf{j}^{inc} \rangle_{S_m} + \frac{1}{2}\langle \mathbf{v}_m, \eta \mathbf{j}_m \rangle_{S_m} \\
& \langle \mathbf{v}_m, \eta \sum_n \pi^{\times}\mathcal{K}(\mathbf{j}_n)\rangle_{S_m}
\end{aligned} \tag{4.8}$$

It is worth pointing out that $\mathcal{R}_m^{(2)}$ carries the physical implication of error electric current, it should be expanded by $\lambda_m \in H(div_{\partial\Omega}, \partial\Omega)$ and paired with basis functions from $H(curl_{\partial\Omega}, \partial\Omega)$. Traditional implementation employ both λ_m for both $\mathbf{j}_m$ and $\mathbf{m}_m$, a seemingly proper testing would render $\mathcal{R}_m^{(2)}$ tested by $\hat{n}_m \times \lambda_m$ and unfortunately this results in singular or almost singular matrix system with inferior condition number. A common practice is to adopt λ_m as testing function to circumvent this numerical issue, which violates the dual-pairing principle. There has been basis functions, e.g., Buffa-Christiansen (BC) basis [55], [56] proposed to alleviate this issue. It is worth pointing out that the BC basis is based on the concept of dual grid and barycentric dual grids[57][58]. Multi-trace IEDG formulation elevates the function space of both trial and testing function to L^2 space, which includes both div-conforming and curl-conforming basis as sub-spaces, it naturally satisfy the dual-pairing principle . Improvement in MFIE solution accuracy has been reported in [41].

4.1.3 Boundary Contour Integral Penalty Term

The L^2 trial function adopted by IEDG does not enforce normal continuity across the boundaries of adjacent elements, electric charges could accumulate at these element boundaries. The discontinuity across the boundaries results in a residual $\mathcal{R}^{(3)}$ on the contour as follows,

$$\mathcal{R}_m^{(3)} = \sum_{C_{mn}} \frac{1}{ik} (\hat{\mathbf{t}}_{mn} \cdot \mathbf{j}_m + \hat{\mathbf{t}}_{nm} \cdot \mathbf{j}_n) \tag{4.9}$$

Note that a scaling factor $\frac{1}{ik}$ is adopted based on the current continuity equation. $\mathcal{R}_m^{(3)}$ is paired with testing function associated with the contour as a penalty term,

$$\begin{aligned}&\langle \hat{\mathbf{t}}_m \cdot \mathbf{v}_m, \mathcal{R}_{C_m}^{(3)} \rangle_{C_m} \\ &= \beta \langle \hat{\mathbf{t}}_m \cdot \mathbf{v}_m, \sum_{C_{mn}} \frac{1}{ik} (\hat{\mathbf{t}}_{mn} \cdot \mathbf{j}_m + \hat{\mathbf{t}}_{nm} \cdot \mathbf{j}_n) \rangle \end{aligned} \tag{4.10}$$

An additional augmentation $\mathcal{P}_{C_{mn}}$ is proposed to due to the error charges from discontinuity of normal component across the contour.

$$\mathcal{P}_{C_{mn}} = \frac{1}{ik} \int_{C_{mn}} (\hat{\mathbf{t}}_{mn} \cdot \mathbf{j}_m + \hat{\mathbf{t}}_{nm} \cdot \mathbf{j}_n)(\mathbf{r}') G(\mathbf{r}, \mathbf{r}') d\mathbf{r}' \tag{4.11}$$

where $G(\mathbf{r}, \mathbf{r}')$ is the free space Green's function. Physically it can be interpreted as the electric potential induced by the error charges accumulated at the boundaries of the elements. The objective is to minimize the measurable energy due to the error charges, consequently this error electric potential should be paired with charges to form energy term $\rho\phi$, namely,

$$\begin{aligned}&\langle \hat{\mathbf{t}}_m \cdot \mathbf{v}_m, \mathcal{R}_{C_m}^{(4)} \rangle_{C_m} \\ &\langle \hat{\mathbf{t}}_m \cdot \mathbf{v}_m, \sum_{C_{mn}} \frac{1}{ik} \int_{C_{mn}} (\hat{\mathbf{t}}_{mn} \cdot \mathbf{j}_m + \hat{\mathbf{t}}_{nm} \cdot \mathbf{j}_n)(\mathbf{r}') G(\mathbf{r}, \mathbf{r}') d\mathbf{r}' \rangle_{C_m} \end{aligned} \tag{4.12}$$

4.1.4 Galerkin Weak Formulation

A linear combination of the weighted residuals from equation(4.3), equation(4.7), equation(4.9), equation(4.12) results in

$$c_1 \langle \mathbf{v}, \mathcal{R}^{(1)} \rangle_{\partial\Omega} + c_2 \langle \mathbf{v}, \mathcal{R}^{(2)} \rangle_{\partial\Omega} + c_3 \langle \mathbf{v}, \mathcal{R}^{(3)} \rangle_C + c_4 \langle \mathbf{v}, \mathcal{R}^{(4)} \rangle_C = 0 \tag{4.13}$$

In general, the coefficient c_1,c_2,c_3,c_4 are determined based on the accuracy, stability and convenience. Inspired by the conventional CFIE combination, c_1 and c_2 are both

chosen to be $\frac{1}{2}$ to combat internal resonances. c_4 is chosen to be $\frac{-1}{2}$ and it is more out of convenience consideration such that the problematic double contour integral term can be canceled out. c_3 has been demonstrated to be crucial to the stability of the algorithm. Herein $c_3 = \frac{1}{10}h^{-1}$ is adopted and more details are available in [41].

4.2 Multi-trace IEDG for composite targets

Numerical solutions of EM response from composite metallic and dielectric structures has attracted tremendous interests from both research and engineering community. Many formulations has been proposed in terms of surface integral equations. A comprehensive study of the existing surface integral equation methods can be found in [59]. We proposed a non-overlapping surface integral equation domain decomposition method in [39]. As shown in 4.14, the original electromagnetic scattering problem

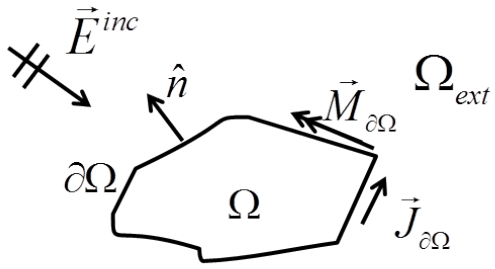

Figure 4.2: An electromagnetic scattering problem from composite targets

from a composite target is decomposed into interior sub-domain and exterior sub-domain, so-called generalized combined field integral equation (G-CFIE) and local electric and magnetic traces are applied to these two domains, respectively. Robin

type transmission conditions (TCs) [60] are prescribed across the surface of the exterior and interior sub-domains. One of the most attractive features of this G-CFIE is that it decouples the interior problem, which corresponds to the Maxwell's equation solution of the interior region, from that of the exterior problem, which is the solution in the free-space. The communication between two regions are achieved by the Robin Type transmission conditions that is capable of enforcing the continuity for both electric and magnetic field. So the performance of this formulation is insensitive to the permittivity and permeability of the interior region. Also, non-conformal mesh is supported and this provide unprecedented flexibility and modularity for problems such as antenna array simulation. More details of this work can be found at [39].

4.2.1 Residual Definition

We denote the exterior and interior region by using superscripts - and +, they tags the trace operators from the sub-region surface $\partial\Omega_m$ from Ω_m. The surface normal $\hat{n}^+$ points from Ω_m to the exterior region Ω_{ext} while $\hat{n}^-$ points from the interior region Ω_{ext} to Ω_m. We introduce two surface trace operators on $\partial\Omega$, the tangential component trace operator $\pi_\tau(\bullet)$ and twisted tangential trace operator $\gamma_\tau(\bullet)$, defined as follows:

$$\gamma_\tau = \hat{n} \times u|_{\partial\Omega} \tag{4.14}$$

$$\pi_\tau = \hat{n} \times (u \times \hat{n})|_{\partial\Omega} \tag{4.15}$$

By letting the observation point r approaches $\partial\Gamma_m^+$, the scattered electric field $e_m^s(j_m^+, e_m^+ \times \hat{n}_m^+)$ and scattered magnetic field $j_m^s(j_m^+, e_m^+ \times \hat{n}_m^+)$ can be represented as follows with

the scaled surface current $j_m^s = \eta_0 \hat{n}^+ \times H_m^s$ on $\partial\Omega_m^+$:

$$
\begin{aligned}
&e_m^s(j_m^+, e_m^+ \times \hat{n}_m^+) \\
&= \pi_\tau(\mathcal{L}_{k_0}(j_m^+; \partial\Omega_m^+)) + \frac{1}{2} e_m^+ - \pi_\tau(\bar{\mathcal{K}}_{k_0}(e_m^+ \times \hat{n}_m^+; \partial\Omega_m^+)) \quad \text{on } \partial\Omega_m^+ \qquad (4.16) \\
&j_m^s(j_m^+, e_m^+ \times \hat{n}_m^+) \\
&= \gamma_\tau(\mathcal{L}_{k_0}(e_m^+ \times \hat{n}^+; \partial\Omega_m^+)) + \frac{1}{2} j_m^+ + \gamma_\tau(\bar{\mathcal{K}}_{k_0}(j_m^+; \partial\Omega_m^+)) \quad \text{on } \partial\Omega_m^+ \qquad (4.17)
\end{aligned}
$$

where $\bar{\mathcal{K}}$ stands for the principle value of $\mathcal{K}$. Subsequently, we can define two residuals by invoking the EFIE and MFIE, respectively:

$$\mathcal{R}_1 = \frac{1}{2} e^+ - \pi_\tau \mathcal{L}_{k_0}(j_m^+; \partial\Omega_m^+)) + \pi_\tau \mathcal{K}_{k_0}(e_m^+ \times \hat{n}_m^+; \partial\Omega_m^+)) - e^{INC} \qquad (4.18)$$

$$\mathcal{R}_2 = \frac{1}{2} j^+ - \gamma_\tau \mathcal{L}_{k_0}(e_m^+ \times \hat{n}^+; \partial\Omega_m^+)) - \gamma_\tau \mathcal{K}_{k_0}(j_m^+; \partial\Omega_m^+)) - j^{INC} \qquad (4.19)$$

To satisfy the continuity of tangential electric and magnetic field across the two regions, Robin type transmission conditions are prescribed and the third residual can be defined as:

$$\mathcal{R}_3 = e_m^+ - j_m^+ - e_m^- - j_m^- \qquad (4.20)$$

These residuals can be defined similarly in the interior domain as:

$$\mathcal{R}_4 = \frac{1}{2} e^- - \pi_\tau \mathcal{L}_{k_0}(j_m^-; \partial\Omega_m^-)) + \pi_\tau \mathcal{K}_{k_0}(e_m^- \times \hat{n}_m^-; \partial\Omega_m^-)) \qquad (4.21)$$

$$\mathcal{R}_5 = \frac{1}{2} j^- - \gamma_\tau \mathcal{L}_{k_0}(e_m^- \times \hat{n}^-; \partial\Omega_m^-)) - \gamma_\tau \mathcal{K}_{k_0}(j_m^-; \partial\Omega_m^+)) \qquad (4.22)$$

$$\mathcal{R}_6 = e_m^- - \eta^- j_m^- - e_m^+ - \eta^- j_m^+ \qquad (4.23)$$

where η^- is the wave impedance in the interior sub-domain.

These residuals are tested with $\lambda^+ \in H(div_{\partial\Omega^+}, \partial\Omega^+)$, $\lambda^- \in H(div_{\partial\Omega^-}, \partial\Omega^-)$, $w^+ \in H(curl_{\partial\Omega^+}, \partial\Omega^+)$, $w^- \in H(curl_{\partial\Omega^-}, \partial\Omega^-)$ to arrive at the following sesquilinear

form :

$$
\begin{aligned}
&(1-\alpha) < w^+, \mathcal{R}_1 > +\alpha < w^+, \mathcal{R}_2 > -\alpha < \lambda^+, \mathcal{R}_1 > -(1-\alpha) < \lambda^+, \mathcal{R}_2 > \\
&+ (1-\alpha) < w^-, \mathcal{R}_4 > +\alpha < w^-, \mathcal{R}_5 > -\alpha < \lambda^-, \mathcal{R}_4 > -(1-\alpha) < \lambda^-, \mathcal{R}_5 > \\
&+ \frac{1}{2} < w^-, R_6 > + \frac{1}{2} < \lambda^-, R_6 > + \frac{1}{2} < w^+, R_3 > + \frac{1}{2} < \lambda^+, R_3 >= 0
\end{aligned} \tag{4.24}
$$

where $\alpha \in R, \alpha \in [0,1]$ is needed to push the resonance frequency to be a complex number and thus immune from internal resonance for real frequencies. We adopt $\alpha = 0.5$ unless otherwise specified.

4.2.2 Finite Dimensional Discretization

For the exterior, these three residuals can be linearly combined and weighted to give rise to the following linear equations:

$$-\alpha\mathcal{R}_1 - (1-\alpha)\mathcal{R}_2 + \frac{1}{2}\mathcal{R}_3 = 0 \tag{4.25}$$

$$(1-\alpha)\mathcal{R}_1 + \alpha\mathcal{R}_2 + \frac{1}{2}\mathcal{R}_3 = 0 \tag{4.26}$$

The original surface $\partial\Omega_m$ is discretized using triangulations denoted by $T^{\pm}$. The electric current $j_m^{\pm}$ and magnetic current $m_m^{\pm}$ are expanded in each element using half-RWG elements. Test equation(4.25) with λ^+ and equation(4.26) with w^+, the multi-trace matrix system can be casted as follows:

$$
\begin{pmatrix}
\mathcal{G}_+^{jj} & \mathcal{G}_+^{jm} & \mathcal{N}_{+-}^{jj} & \mathcal{N}_{+-}^{jm} \\
\mathcal{G}_+^{mj} & \mathcal{G}_+^{mm} & \mathcal{N}_{+-}^{mj} & \mathcal{N}_{+-}^{mm} \\
\mathcal{N}_{-+}^{jj} & \mathcal{N}_{-+}^{jm} & \mathcal{G}_-^{jj} & \mathcal{G}_-^{jm} \\
\mathcal{N}_{-+}^{mj} & \mathcal{N}_{-+}^{mm} & \mathcal{G}_-^{mj} & \mathcal{G}_-^{mm}
\end{pmatrix}
\cdot
\begin{pmatrix}
j^+ \\ m^+ \\ j^- \\ m^-
\end{pmatrix}
=
\begin{pmatrix}
b_+^j \\ b_+^m \\ b_-^j \\ b_-^m
\end{pmatrix}
\tag{4.27}
$$

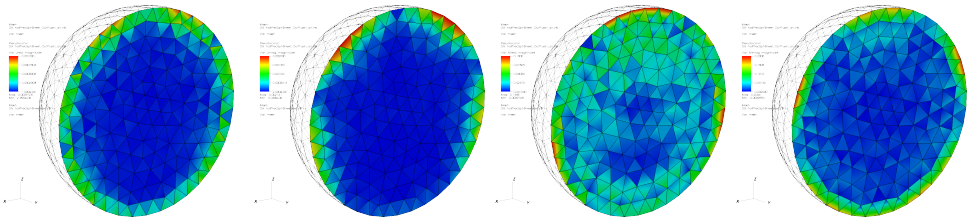

(a) $Re(j_m^+ + j_m^-)$ (b) $Im(j_m^+ + j_m^-)$ (c) $Re(m_m^+ + m_m^-)$ (d) $Im(m_m^+ + m_m^-)$

Figure 4.3: Error j and m on dielectric interface using $j_m^{\pm} = span\{\lambda'\}$ and $m_m^{\pm} = span\{\lambda'\}$

where the matrix entries are essentially

$\mathcal{G}_+^{jj}$	$\alpha < \lambda_j^+, \pi_\tau \mathcal{L}(j^+) > \ +(1-\alpha) < \lambda_j^+, \gamma_\tau \mathcal{K}(j^+) - \frac{1}{2} j^+ > \ + \frac{1}{2} < \lambda_j^+, j^+ >$
$\mathcal{G}_+^{jm}$	$(1-\alpha) < \lambda_j^+, \gamma_\tau \mathcal{L}(m^+) > \ -\alpha < \lambda_j^+, \pi_\tau \mathcal{K}(m^+) + \frac{1}{2} \hat{n}^+ \times m^+ > \ - \frac{1}{2} < \lambda_j^+, \hat{n}^+ \times m^+ >$
$\mathcal{N}_{+-}^{jj}$	$\frac{1}{2} < \lambda_j^+, j^- >$
$\mathcal{N}_{+-}^{jm}$	$\frac{1}{2} < \lambda_j^+, \hat{n}^- \times m^- >$
b_+^j	$\alpha < \lambda_j^+, e^{INC} > +(1-\alpha) < \lambda_j^+, j^{INC} >$
$\mathcal{G}_+^{mj}$	$-(1-\alpha) < \hat{n}^+ \times \lambda_m^+, \pi_\tau \mathcal{L}(j^+) > \ -\alpha < \hat{n}^+ \times \lambda_m^+, \gamma_\tau \mathcal{K}(j^+) - \frac{1}{2} j^+ > \ + \frac{1}{2} < \hat{n}^+ \times \lambda_m^+, j^+ >$
$\mathcal{G}_+^{mm}$	$-\alpha < \hat{n}^+ \times \lambda_m^+, \gamma_\tau \mathcal{L}(m^+) > \ +(1-\alpha) < \hat{n}^+ \times \lambda_m^+, \pi_\tau \mathcal{K}(m^+) + \frac{1}{2} \hat{n}^+ \times m^+ > \ - \frac{1}{2} < \hat{n}^+ \times \lambda_m^+, \hat{n}^+ \times m^+ >$
$\mathcal{N}_{+-}^{mj}$	$\frac{1}{2} < \hat{n}^+ \times \lambda_m, j^- >$
$\mathcal{N}_{+-}^{mm}$	$+\frac{1}{2} < \hat{n}^+ \times \lambda_m^+, \hat{n}^- \times m^- >$
b_+^m	$-\alpha < \hat{n}^+ \times \lambda_m, j^{INC} > -(1-\alpha) < \hat{n}^+ \times \lambda_m, e^{INC} >$

4.3 Multi-trace IEDG with Enhanced Enforcement of Transmission Conditions

For some highly resonant structures, e.g., antenna and frequency selective surface, etc., we observed that the G-CFIE formulation elucidated in the previous section produces less accurate result. Further investigation reveals that this is highly related with the energy loss, i.e., the transmission conditions that satisfy the continuity between the tangential electric and magnetic field on $\partial\Omega_m$ is not well enforced, especially at the interface of PEC and dielectrics.

4.3.1 Issues with the Enforcement of Transmission Conditions

For a PEC hemisphere shell example shown in Figure.4.3a to Figure.4.3d, we observed obvious large electric error current and large magnetic error current on the interface. This is particularly obvious on the ring where PEC and dielectric interface.

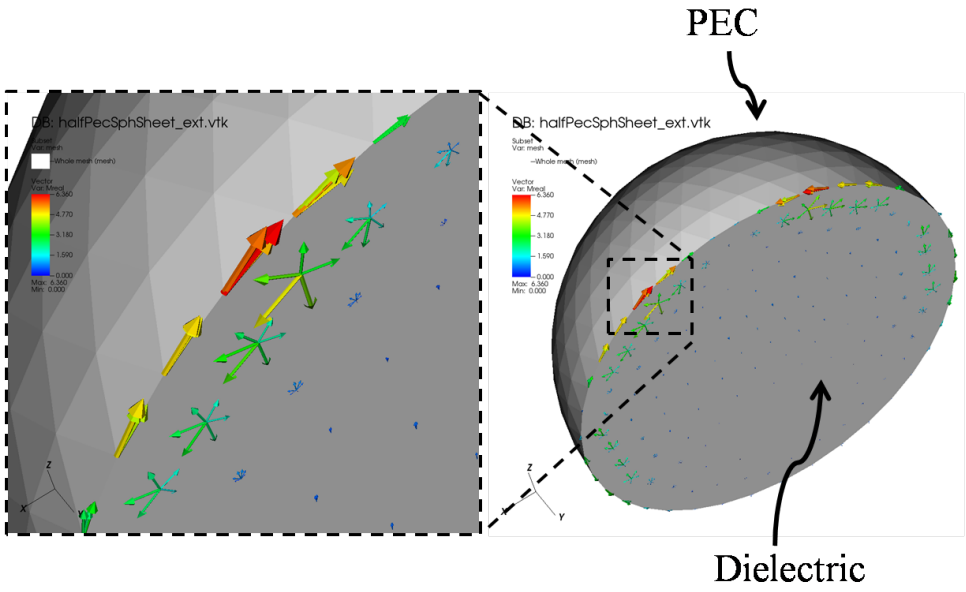

Figure 4.4: Real part of magnetic current along the PEC-dielectric interface

Recall that the transmission conditions only apply on the dielectric part of the surface, no transmission conditions are enforced on the PEC side. Observe Figure. 4.4 and strong magnetic currents that flows tangentially along the PEC-dielectric interface is observed. This suggests that the basis functions for magnetic currents should be able to effectively represent this tangential component. However, as is shown on Figure.4.5, the magnetic current $m_m^{\pm} = span\{\lambda'\}$ on the PEC-dielectric

interface, where λ_i' is defined as:

$$\lambda_i' = \begin{cases} \frac{(\vec{r}-\vec{r}_i)l_i}{2A} & \vec{r} \in T \\ 0 & \text{elsewhere} \end{cases}$$

where $\vec{r}$ is the evaluation point, T is the triangulation that serves as the support of λ_i', l_i is the length of the edge associated with λ_i' and A is the area of the triangle. Assume edge $r_1 r_2$ is on the PEC-dielectric interface, it can be observed that λ_0' is dominated by components that flow normal to the edge. A more intuitive explanation involve the

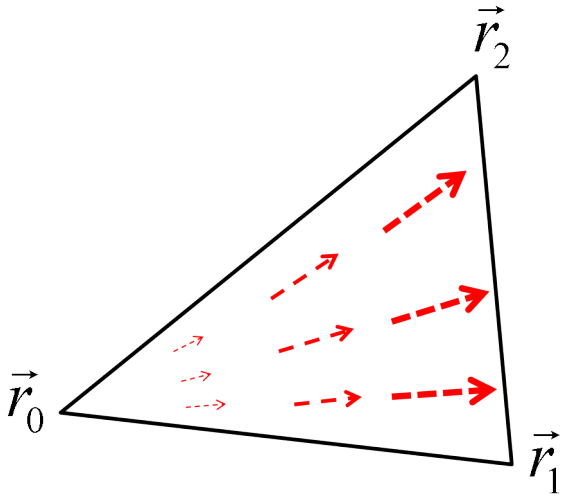

Figure 4.5: Current pattern of λ_0'

relationship between the basis function for electric current and electric field revisit the Robin type transmission conditions in $\mathcal{R}_3$ and $\mathcal{R}_6$, physically electric field $e^{\pm}$ should be normal to magnetic field $h^{\pm}$, thus electric current $j^{\pm} = \hat{n} \times h^{\pm}$ should be somewhat parallel to $e^{\pm}$. However, conventional implementation expand the electric current $j^{\pm}$ and magnetic current $m^{\pm}$ in terms of the same type of basis function, e.g., div-conforming RWG basis for conformal G-CFIE case or half-RWG basis for

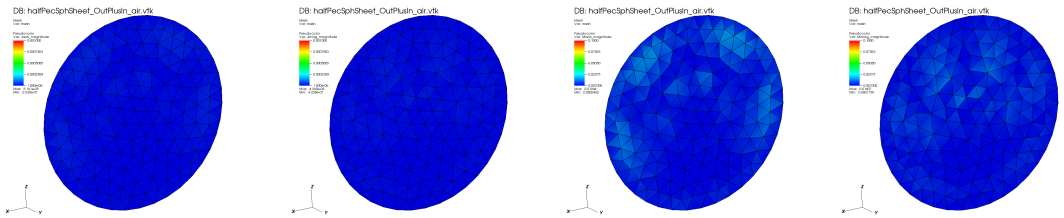

(a) $Re(j_m^+ + j_m^-)$ (b) $Im(j_m^+ + j_m^-)$ (c) $Re(m_m^+ + m_m^-)$ (d) $Im(m_m^+ + m_m^-)$

Figure 4.6: Error j and m on dielectric interface using $j_m^\pm = span\{\lambda'\}$ and $m_m^\pm = span\{\hat{n}^\pm \times \lambda'\}$

multi-trace IEDG formulation. This implies that the electric field $e^\pm = \hat{n} \times m^\pm$ is expanded in terms of rotated RWG basis and this contradicts the physics.

4.3.2 Proposed Solution

To correct this discrepancy, we propose to expand $j_m^\pm \in X_m^\pm$ and $m_m^\pm \in \hat{n}^\pm \times X_m^\pm$, such that $j^\pm$ and $e^\pm$ parallel each other in terms of basis functions definition. Note that equation(4.26) carries the physical quantity of electric current and it should be paired with electric field $e_m^\pm = \hat{n}^\pm \times m^\pm$, so it should be tested by λ' as well. Consequently, all the residuals are well tested, especially the transmission conditions in $\mathcal{R}_3$ and $\mathcal{R}_6$. Here we give the proposed sesquilinear form :

$$\begin{aligned}
&(1-\alpha) < \lambda^+, \mathcal{R}_1 > +\alpha < \lambda^+, \mathcal{R}_2 > -\alpha < \lambda^+, \mathcal{R}_1 > -(1-\alpha) < \lambda^+, \mathcal{R}_2 > \\
&+ (1-\alpha) < \lambda^+, \mathcal{R}_4 > +\alpha < \lambda^+, \mathcal{R}_5 > -\alpha < \lambda^-, \mathcal{R}_4 > -(1-\alpha) < \lambda^-, \mathcal{R}_5 > \\
&+ \frac{1}{2} < \lambda^-, R_6 > + \frac{1}{2} < \lambda^+, R_3 >= 0
\end{aligned} \tag{4.28}$$

$X_m^\pm = \lambda'$

Our first attempt employed conventional half-RWG basis λ' as $X_m^\pm$. Numerical results in Figure.4.6a through Figure.4.6d demonstrates that the error j and m is

reduced by 2 to 3 orders of magnitude. However, loss of accuracy is observed for a dielectric coated PEC sphere example as is shown in Figure.4.7. This is due to the fact that $\bigtriangledown \cdot (\hat{n}^{\pm} \times \lambda') = 0$, recall that integration by part is performed in equation(4.6), adoption of divergence free basis function for $m_m^{\pm}$ set terms involving $\bigtriangledown \cdot \mathbf{v}_m$ to zero, consequently leads to loss of interpolative accuracy.

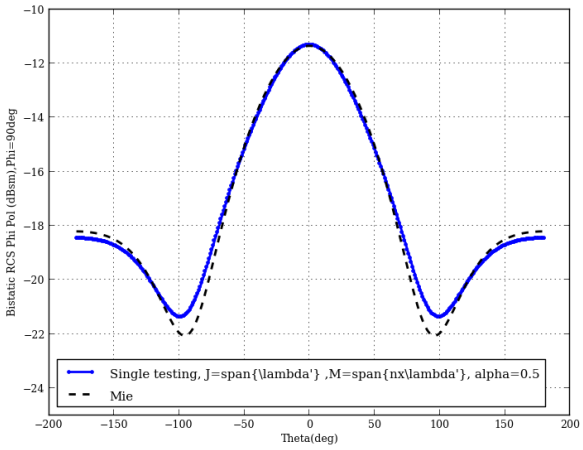

Figure 4.7: Far field comparison with MIE series

$X_m^{\pm} = LB \times \hat{n}^{\pm}$

For a triangle element, each edge relates to one λ' basis and they span a subset of the full linear space, but unfortunately $\bigtriangledown \cdot (\hat{n}^{\pm} \times \lambda') = 0$ and this leads to loss of solution accuracy. Herein we propose $X_m^{\pm} = span\{LB \times \hat{n}^{\pm}\}$, where LB stands for linear basis and they originates from the 6 basis defined on edges from the definition of $H1curl$ basis [61]. Originally, each one of the 6 basis function has support on both triangles that share the same edge, they are split into two independent basis that has

support only in the corresponding triangle patch in the IEDG scheme. Now the 6 basis within each triangle span the full linear space and the definition of the basis function together with its divergence and curl are given as follows,

$$
\begin{aligned}
c_1 &= v \bigtriangledown w - w \bigtriangledown v & \bigtriangledown \cdot c_1 &= 0 & \bigtriangledown \times c_1 &= -\frac{2}{Ly'^2}\hat{n} \\
c_2 &= v \bigtriangledown w + w \bigtriangledown v & \bigtriangledown \cdot c_2 &= 2\frac{x'_2 - L}{y'^2_2} & \bigtriangledown \times c_2 &= 0 \\
c_3 &= w \bigtriangledown u - u \bigtriangledown w & \bigtriangledown \cdot c_3 &= 0 & \bigtriangledown \times c_3 &= -\frac{2}{Ly'^2}\hat{n} \\
c_4 &= w \bigtriangledown u + u \bigtriangledown w & \bigtriangledown \cdot c_4 &= -2\frac{y'^2_2 + x'_2(x'_2 - L)}{L^2 y'^2_2} & \bigtriangledown \times c_4 &= 0 \\
c_5 &= u \bigtriangledown v - v \bigtriangledown u & \bigtriangledown \cdot c_5 &= 0 & \bigtriangledown \times c_5 &= -\frac{2}{Ly'^2}\hat{n} \\
c_6 &= u \bigtriangledown v + v \bigtriangledown u & \bigtriangledown \cdot c_6 &= 2\frac{x'_2 - L}{y'^2_2} & \bigtriangledown \times c_6 &= 0
\end{aligned} \tag{4.29}
$$

where u, v, w are the barycentric coordinate of the evaluating point. $L = |r_1 - r_3|$ where r_1, r_2, r_3 are the 3 vertices of a triangle following the right hand rule. x'_2 and y'_2 is the coordinate of r_2 in the normalized system. The divergence of the rotated basis, i.e., $LB \times \hat{n}^{\pm}_m$ can be found by invoking the vector identity.

$$
\bigtriangledown \cdot (c_i \times \hat{n}^{\pm}_m) = \hat{n}^{\pm}_m \cdot \bigtriangledown \times c_i \tag{4.30}
$$

4.3.3 Numerical Results

In this section we validate the proposed multi-trace IEDG formulation by calculating both canonical and more complicate examples. Both the far field accuracy and near field error currents are investigated.

Dielectric Coated PEC Sphere

We employ the proposed method to calculate the dielectric coated PEC sphere calculated in Figure.4.7, the far field result is compared again MIE series results in

Figure.4.8, excellent agreements have been observed. Having established the accuracy

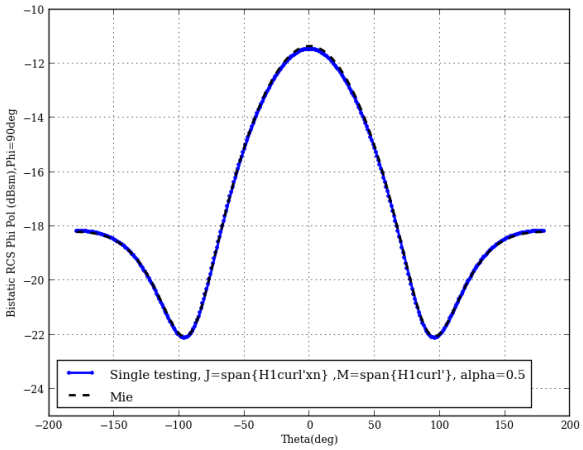

Figure 4.8: Far field comparison against MIE series

of the method, we examine the near field error j and m currents. Compared with Figure.4.3a to Figure.4.3d, the error currents shown from Figure.4.9a to Figure.4.9d are successfully reduced by 2 to 3 orders of magnitude.

Slot Example

Highly resonant structures such as frequency selective surfaces (FSS) contains complicated geometrical structures including the hybrid of PEC and dielectric structures. The multi-trace IEDG formulation proposed are employed herein to calculate a slot example to demonstrate the improvement in performance. The geometry of the slot example is shown in Figure.4.10 together with the incident wave setup.

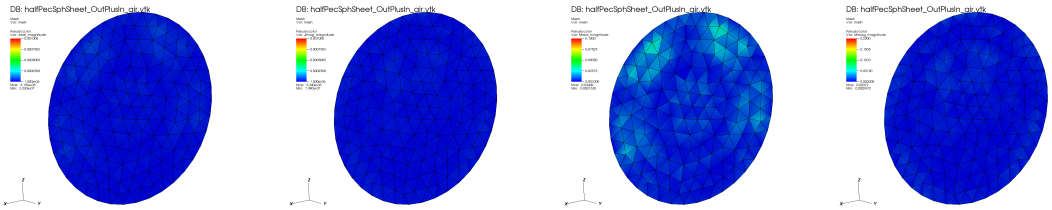

(a) $Re(j_m^+ + j_m^-)$ (b) $Im(j_m^+ + j_m^-)$ (c) $Re(m_m^+ + m_m^-)$ (d) $Im(m_m^+ + m_m^-)$

Figure 4.9: Error j and m on dielectric interface using $j_m^{\pm} = span\{LB \times \hat{n}_m^{\pm}\}$ and $m_m^{\pm} = span\{LB\}$

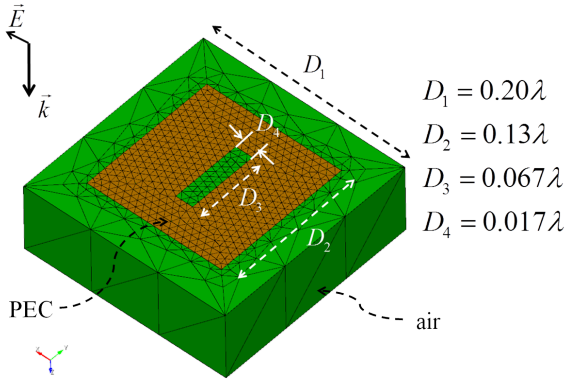

Figure 4.10: Geometry of a small slot example

The far field result of the proposed method corresponds to the black curve in Figure.4.11, it demonstrates improved accuracy against the existing multi-trace IEDG result in blue curve where $X_m^{\pm} = \lambda'$.

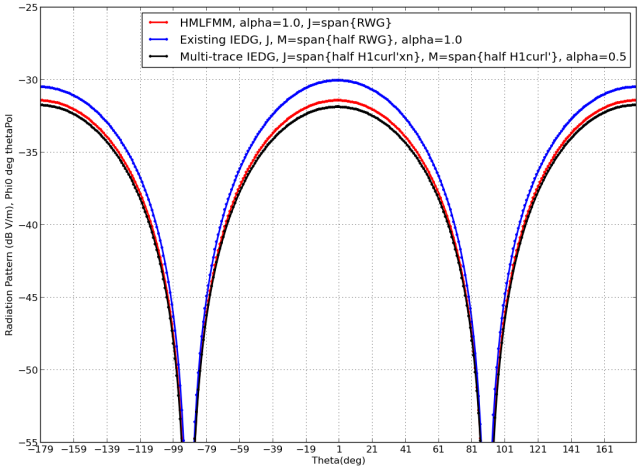

Figure 4.11: Far field comparison of the small slot example

Comparing with Figure.4.12, where strong error current has been observed close to the interface of PEC and air slot, especially in the vicinity of corners. Figure.4.13 shows error currents that are 2 to 3 orders lower in terms of magnitude.

We define the normalized energy loss as follows:

$$P_{loss} = -\frac{Re[\frac{1}{2}\int_{\partial\Omega}(\vec{J}^* \times \vec{M}) \cdot \hat{n} dS]}{Re[\frac{1}{2}\int_{\partial\Omega_{xsec}}(\vec{E}^{inc} \times \left(\vec{H}^{inc}\right)^*) \cdot \hat{n} dS]} \times 100\% \tag{4.31}$$

where $\partial\Omega_{xsec}$ denotes the cross section of the target with respective to the incident wave. Note that $P_{loss} > 0$ indicates energy loss, $P_{loss} < 0$ indicates energy gain. The normalized energy loss for the case shown in Figure.4.12 is 4.15% or $-13.8dB$, the

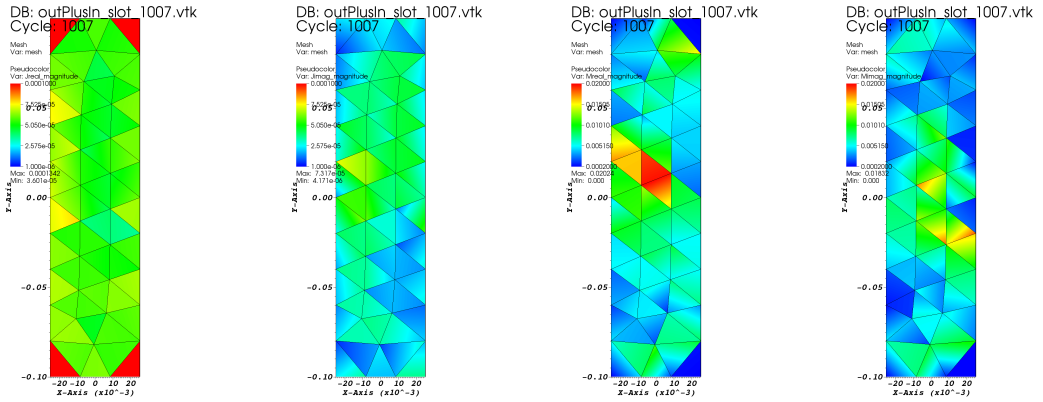

(a) $Re(j_m^+ + j_m^-)$ (b) $Im(j_m^+ + j_m^-)$ (c) $Re(m_m^+ + m_m^-)$ (d) $Im(m_m^+ + m_m^-)$

Figure 4.12: Error j and m in slot using $j_m^\pm = span\{\lambda'\}$ and $m_m^\pm = span\{\lambda'\}$

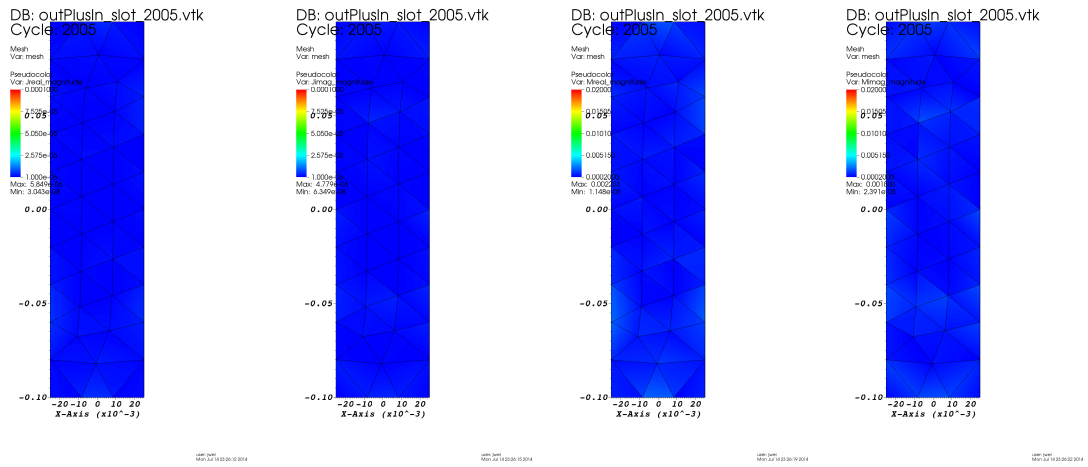

(a) $Re(j_m^+ + j_m^-)$ (b) $Im(j_m^+ + j_m^-)$ (c) $Re(m_m^+ + m_m^-)$ (d) $Im(m_m^+ + m_m^-)$

Figure 4.13: Error j and m in slot using $j_m^\pm = span\{LB \times \hat{n}_m^\pm\}$ and $m_m^\pm = span\{LB\}$

new formulation with enhanced enforcement of transmission conditions reduce the energy loss to 0.42% or $-23.7dB$.

4.4 Multi-trace IEDG with Infinite PEC Ground Plane

In practical applications, antenna structures are usually radiating in complex environment, including infinite ground plane. In this section, IEDG formulation is extended to incorporate the infinite PEC ground plane effect. Numerical examples involving both scattering and radiation problems are conducted to demonstrate the effect of the infinite ground plane.

4.4.1 Boundary Value Problem

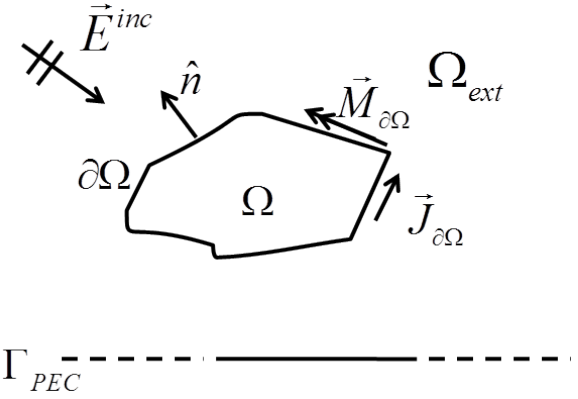

Figure 4.14: Illustration of the boundary value problem with infinite PEC ground plane

As illustrated in Figure.4.14, the boundary value problem can be considered as follows,

$$\begin{cases} \bigtriangledown \times \bigtriangledown \times \vec{E}^{scat} - k_o^2 \vec{E}^{sca} = 0 & \text{in } \Omega_{ext} \\ \pi_t(\vec{E}^{inc} + \vec{E}^{sca}) = \pi_t \vec{E}_\Omega & \text{on } \partial\Omega \\ \pi^\times(\bigtriangledown \times \vec{E}^{inc} + \bigtriangledown \times \vec{E}^{sca}) = \pi^\times \bigtriangledown \times \vec{E}_\Omega & \text{on } \partial\Omega \\ \pi_t(\vec{E}^{inc} + \vec{E}^{sca}) = 0 & \text{on } \Gamma_{PEC} \\ \lim_{|\vec{r}|\to\infty} |\vec{r}|(\bigtriangledown \times \vec{E}^{sca} + ik_0 \hat{r} \times \vec{E}^{sca}) = 0 \end{cases} \tag{4.32}$$

The aforementioned boundary value statement can be updated by introducing another set of imaginary sources $\vec{J}_{\partial\Omega'}$ and $\vec{M}_{\partial\Omega'}$ on the imaged equivalence surface $\partial\Omega'$, as demonstrated in Figure.4.15.

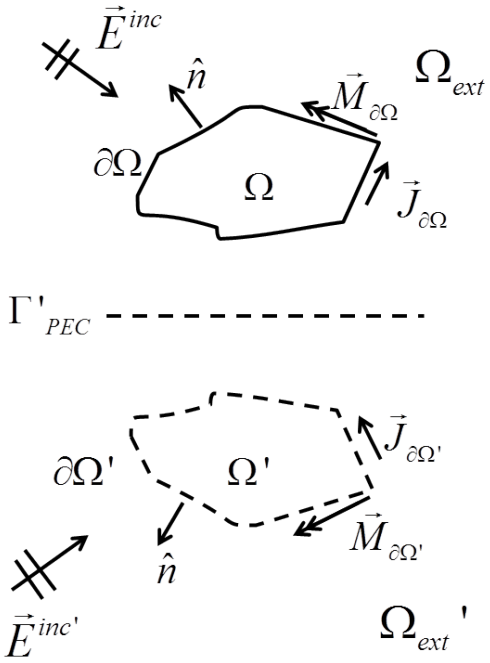

Figure 4.15: Illustration of the updated boundary value problem with infinite PEC ground plane

4.4.2 Multi-trace IEDG with Infinite PEC Ground Plane

Note that any external excitation source, including the source that is infinitely far away and generates the plane waves, should be imaged according to the image theory.

$$\begin{cases} \bigtriangledown \times \bigtriangledown \times \vec{E}^{scat} - k_o^2 \vec{E}^{sca} = 0 & \text{in } \Omega_{ext} \\ \pi_t(\vec{E}^{inc} + \vec{E}^{sca}) = \pi_t \vec{E}_\Omega & \text{on } \partial\Omega \\ \pi^\times(\bigtriangledown \times \vec{E}^{inc} + \bigtriangledown \times \vec{E}^{inc'} + \bigtriangledown \times \vec{E}^{sca}) = \pi^\times \bigtriangledown \times \vec{E}_\Omega & \text{on } \partial\Omega \\ \pi_t(\vec{E}^{inc} + \vec{E}^{inc'} + \vec{E}^{sca}) = 0 & \text{on } \Gamma'_{PEC} \\ \lim_{|\vec{r}|\to\infty} |\vec{r}|(\bigtriangledown \times \vec{E}^{sca} + ik_0 \hat{r} \times \vec{E}^{sca}) = 0 \end{cases} \tag{4.33}$$

Considering the fact that the scattering field $\vec{E}^{sca} = \mathcal{L}(\vec{J}_{\partial\Omega}) - \mathcal{K}(\vec{M}_{\partial\Omega}) + \mathcal{L}(\vec{J}_{\partial\Omega'}) - \mathcal{L}(\vec{K}_{\partial\Omega'})$. Subsequently, the fourth condition can be satisfied separately by the incident wave and equivalent sources after invoking the Stratton-Chu representation in terms of the electric current $\vec{J}_{\partial\Omega}$, $\vec{J}_{\partial\Omega'}$ and $\vec{M}_{\partial\Omega}$, $\vec{M}_{\partial\Omega'}$, provided that the imaged sources satisfy the image theory.

$$\pi_t(\vec{E}^{inc} + \vec{E}^{inc'})|_{\Gamma'_{PEC}} = 0 \tag{4.34}$$

$$\pi_t(\mathcal{L}(\vec{J}_{\partial\Omega}) - \mathcal{K}(\vec{M}_{\partial\Omega}) + \mathcal{L}(\vec{J}_{\partial\Omega'}) - \mathcal{L}(\vec{K}_{\partial\Omega'}))|_{\Gamma'_{PEC}} = 0 \tag{4.35}$$

Consequently, the IEDG formulation from last section can be employed with the additional image sources for the problems in the presence of infinite PEC ground plane.

For the scenario that the part of the geometry is touching or below the ground plane surface as demonstrated in Figure.4.16. For the currents that resides below the infinite PEC ground plane, the electromagnetic field identically zero everywhere below the ground plane, this part of the currents will be dropped. Also, for the equivalent electric current resides right on the ground plane will cancel out with its image. While the magnetic current will also be zero since the total tangential electric

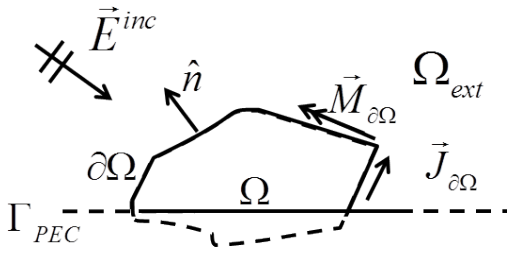

Figure 4.16: Illustration of the problem with part of the geometry below the infinite PEC ground plane

field on the ground plane surface is zero. The equivalent problem with these currents removed is demonstrated in Figure.4.17

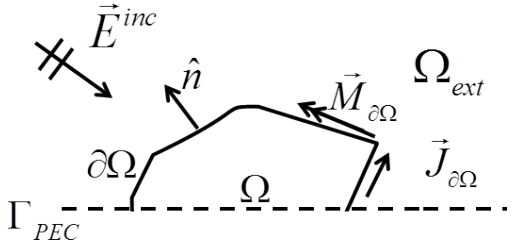

Figure 4.17: Illustration of the equivalent problem with part of the geometry below the infinite PEC ground plane

4.5 Numerical Results

4.5.1 Tank example

In this example a mock-up PEC tank resides on a infinite PEC ground is impinged upon by a plane wave at 2GHz as demonstrated in Figure.4.18. After discretization, the free standing tank gives rise to 1,027,554 DoFs. The free standing tank consumes 14.6 GB RAM while the tank on the ground plane examples consumes 28.8 GB

memory. This is consistent with the $O(N)$ complexity of conventional MLFMM, which is adopted to accelerate the IEDG. Strong electric field has been observed at

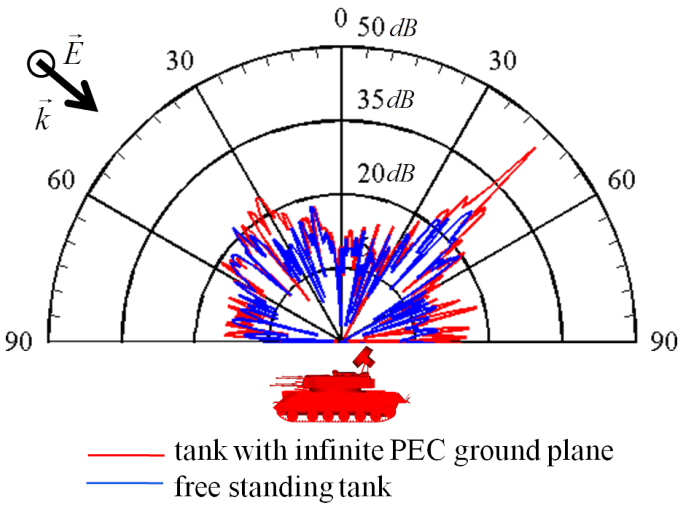

Figure 4.18: Total far field electric field result for the tank example with and without infinite PEC ground plane

the reflection direction as expected. In the near field result, strong electric current is observed in Figure.4.22 compared with the free standing tank in Figure.4.20.

4.5.2 Monopole Antenna

For this monopole antenna at 75MHz, we employed the multi-solver domain decomposition method (MS-DDM) [40] to solve for this radiation problem. First order Robin type transmission condition [40] is enforced as the field continuity condition. The interior domain is modeled by FEM while the exterior surface modeled by IEDG is used to terminate the solution region. This model is simulated with and without the infinite PEC ground plane. Note that the length of the original PEC base from the monopole antenna is only 0.0875λ. Total electric far field from both simulations

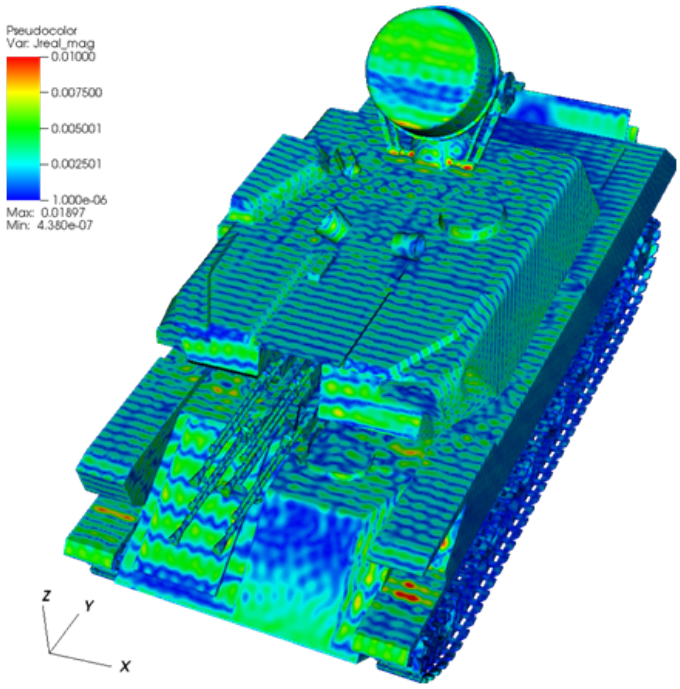

Figure 4.19: Top view of the real part of the electric current on a free standing tank without infinite PEC ground plane

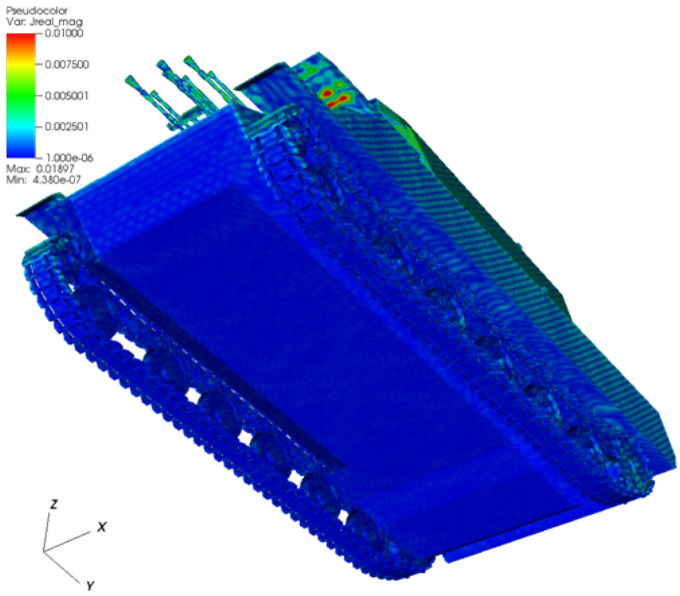

Figure 4.20: Bottom view of the real part of the electric current on a free standing tank without infinite PEC ground plane

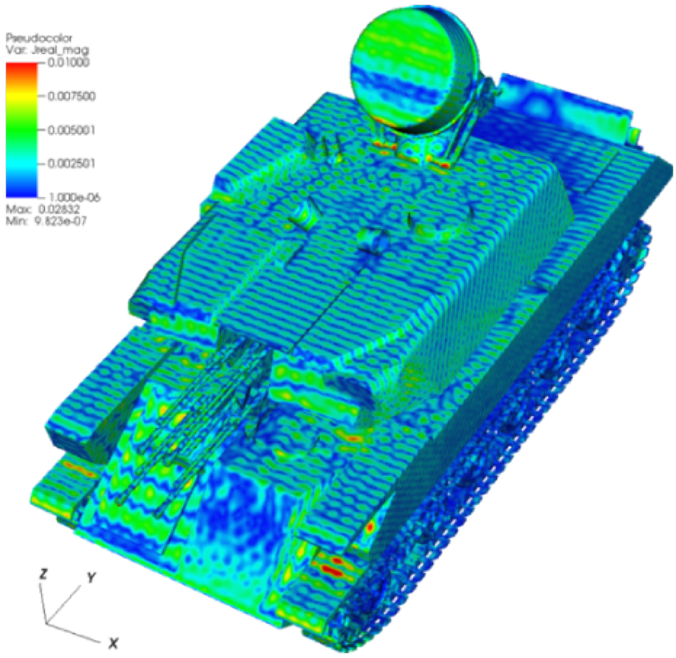

Figure 4.21: Top view of the real part of the electric current on a tank in the presence of the infinite PEC ground plane

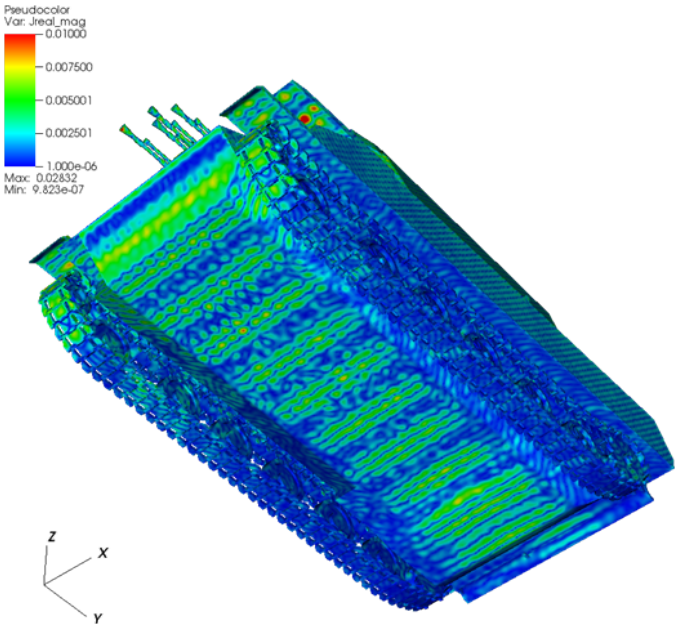

Figure 4.22: Bottom view of the real part of the electric current on a tank in the presence of the infinite PEC ground plane

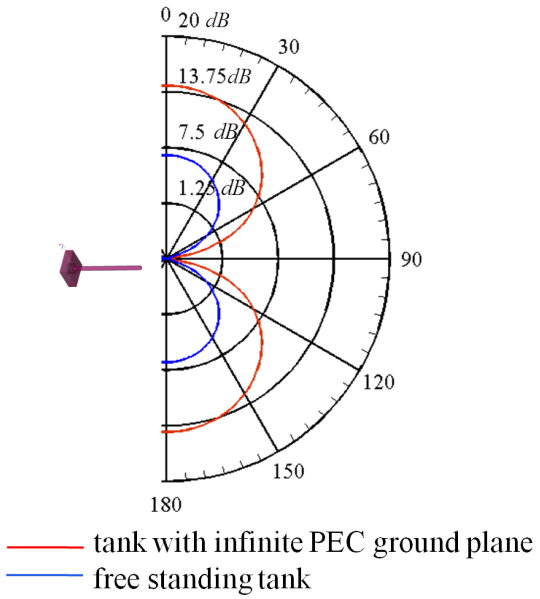

Figure 4.23: Radiation pattern for the monopole antenna with and without infinite PEC ground plane

is compared and plotted in Figure.4.23, maximum far field in the broad size is enhance from 6.6 dB to 13.9 dB after the installation of infinite PEC ground plane. On the other hand, the S_{11} of the monopole antenna drops from -2.4 dB in the free standing case to -17.5 dB with the infinite PEC ground plane. Compared with the free standing case shown in Figure.4.24, stronger electric current is observed after the installation of ground plane as shown in Figure.4.25.

4.5.3 NGC Wideband Antenna Array

In this example, we employed the multi-trace IEDG with infinite ground plane in the MS-DDM scheme and solve for a real life antenna array problem. The multi-trace IEDG with infinite ground plane serves as the truncation boundary for the FEM-DDM solver. Good agreements between numerical simulation and measurement results are

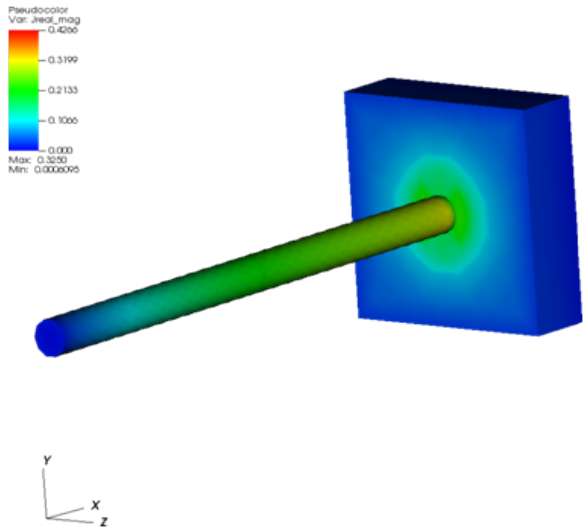

Figure 4.24: Top view of the real part of the electric current on the free standing monopole antenna

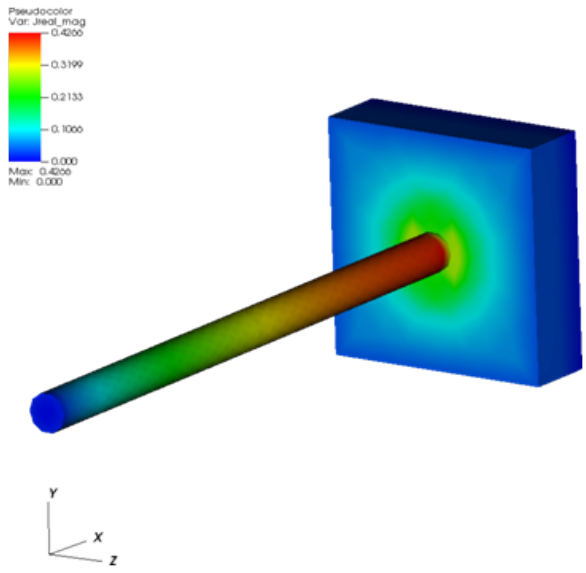

Figure 4.25: Top view of the real part of the electric current on the monopole antenna mounted on infinite PEC ground

observed. The geometry of the 8 by 8 antenna array is depicted in Figure.4.26. Each antenna unit contains two ports and the port excited in this study is demonstrated in Figure.4.26. The frequency range of this antenna array is from 500MHz to 4GHz, we simulate the antenna at 3.0GHz with infinite ground plane prescribed on XOY plane.

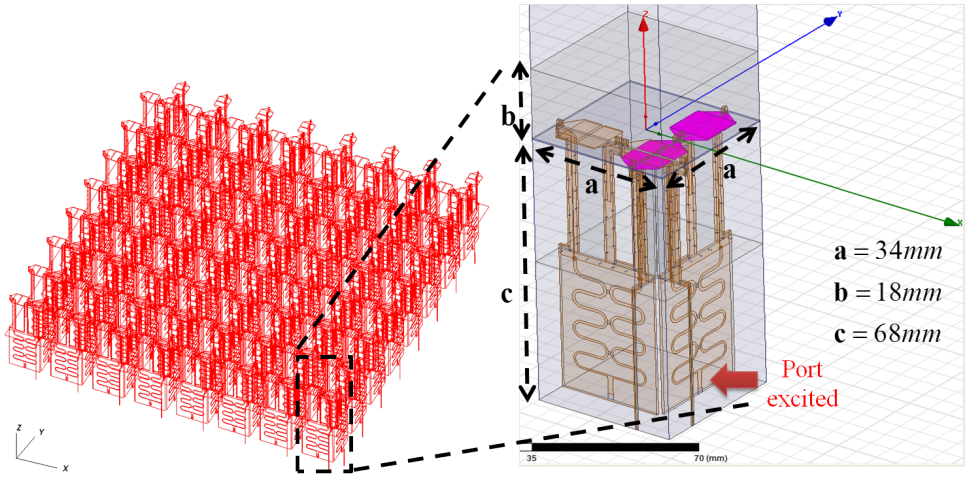

Figure 4.26: NGC 8x8 antenna array

We excite the array element based on purely array factor such that it scans 60^o in positive Y direction. S_{11} distribution for the array is plotted in Figure.4.27

A 3D view of the theta polarization far field is provided in Figure.4.28. Figure.4.29 shows the 2D far field on E plane, where the maximum radiation direction points at 51^o instead of 60^o due to the mutual coupling between elements.

This shift of maximum radiation direction is also observed in measurement results shown in Figure.4.30.

It should be pointed out that the measurement is the result from the antenna array with finite, but reasonably large ground plane. We modeled the finite ground

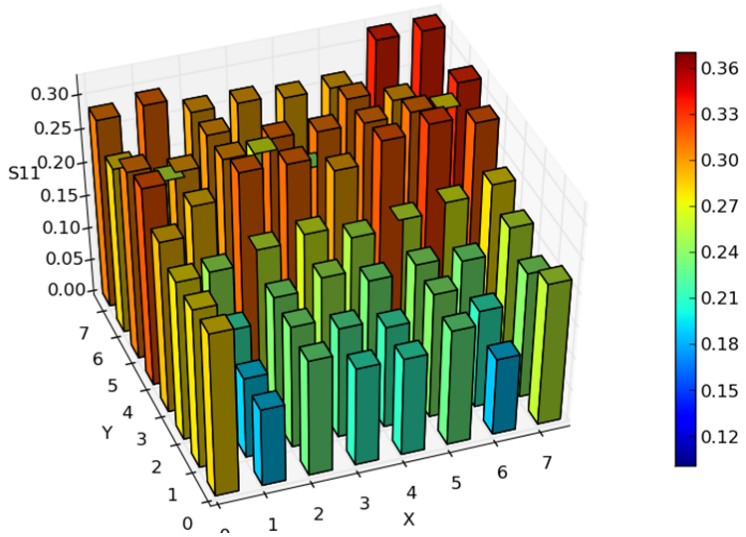

Figure 4.27: S_{11} distribution of NGC 8x8 antenna array scanning 60^o toward positive Y direction

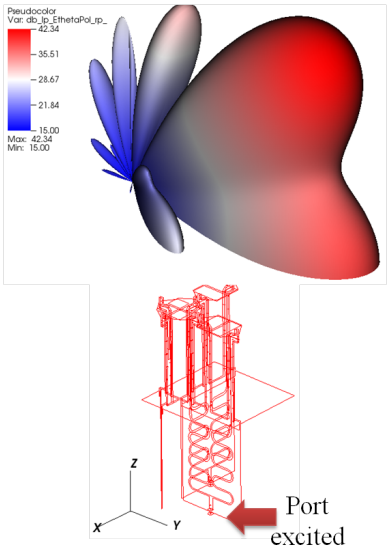

Figure 4.28: 3D far field of theta polarization, NGC 8x8 antenna array scanning 60^o toward positive Y direction

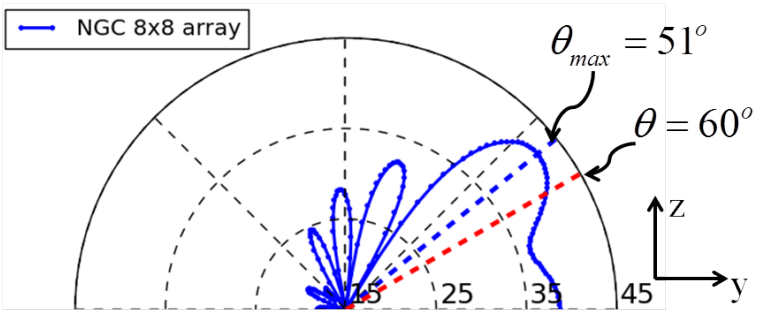

Figure 4.29: Far field of theta polarization on E plane, NGC 8x8 antenna array scanning 60^o toward positive Y direction

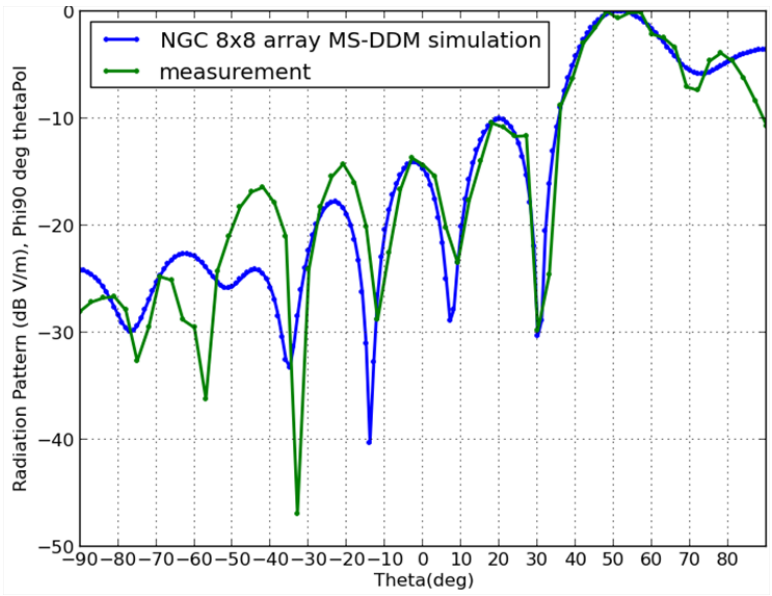

Figure 4.30: Comparison of normalized far field on E plane with measurement, NGC 8x8 antenna array scanning 60^o toward positive Y direction

plane based on the actual size of the ground plane applied in the measurement and the E plane far field results are compared against measurement result in Figure.4.31, good agreements has been observed.

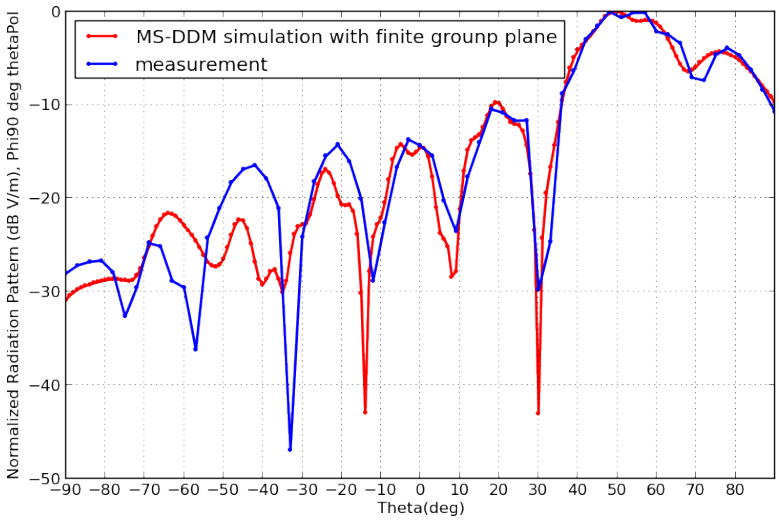

Figure 4.31: Comparison of far field on E plane with finite ground plane, NGC 8x8 antenna array scanning 60^o toward positive Y direction

4.6 Conclusion

An novel IEDG method with enhanced enforcement of transmission conditions is proposed, together with the IEDG algorithm scheme, this makes it possible to solve surface integral equation without relying on the conformal mesh and basis functions with inter-element continuity. Various basis functions with different definitions and orders can be chosen flexibly to form a robust surface integral equation solver for multi-scale structures. IEDG algorithm allows local mesh refinement and greatly facilitates wideband analysis. This algorithm is enhanced by improved enforcement

of the transmission conditions for highly resonant structures. Lastly, ground plane capability is incorporated with this IEDG algorithm and good agreements with measurements have been observed.

Chapter 5: Conclusion

Surface integral equation methods have been quite attractive for solving electromagnetic wave scattering and radiation problems since only the surface of the target needs to be discretized, and subsequently requiring much less number of unknowns by orders of magnitude compared to the volume discretization counterparts. Quite a number of methods and algorithms have been proposed to accelerate SIE solution, yet the multi-scale and low frequency nature of some problems still pose serious challenges due to the sub-wavelength breakdown problem resulted from the dense mesh either in local or global scale. Consequently, multiple meshes based on multiple frequency bands are usually needed for a wide-band analysis. Unfortunately, meshing and discretization of real-life models often pose difficulties that requires tremendous amount of human intervention. The capability to recycle the mesh obtained at higher frequencies, where mesh with good quality can be obtained with less effort, for lower frequencies greatly alleviates this meshing problem. The first part of this dissertation focuses on solving the multi-scale and low frequency problem using direct and iterative methods.

Firstly, a hierarchical direct solver algorithm is developed to solve integral equations in 3D electromagnetic wave scattering from non-penetrable targets. The proposed algorithm utilizes the skeletonalization process to effectively compress the rank-deficient off-diagonal blocks, which correspond to the couplings between groups. Huygen's surfaces are also introduced to account for the far field couplings efficiently, and thus further accelerate the algorithm. It has been demonstrated that the condition number of the system matrix would still affect the solution errors of direct solvers. Despite the limitations, for problems of small or medium electrical sizes, the multi-level version of the proposed algorithm features $O(N^{1.3})$ and $O(N)$ complexity for memory consumption and $O(N^{1.8})$ and $O(N^{1.5})$ for CPU times for fixed mesh size and for h-refinement scenarios, respectively.

Secondly, we propose an iterative solver oriented H-MLFMM algorithm for solving low frequency and multi-scale electromagnetic problems. H-MLFMM alleviates the sub-wavelength breakdown problem of conventional MLFMM by compressing the near field matrix and near to far mapping matrices via their skeleton DoFs, respectively. Particularly, Huygens' principle is exploited to expedite the skeletonalization process in an error controllable fashion. Numerical results demonstrate that H-MLFMM is error controllable and robust within a wide range of spectrum. It should be pointed out that rather than accelerating the matrix vector multiplication of the original problem, it could be a promising topic to extract the skeleton unknowns and directly employ them as the new basis for the original problem, thus reducing the size of the problem and potential improve the condition number of the system.

For the composite targets, an novel IEDG method with enhanced enforcement of transmission conditions is proposed, together with the existing IEDG algorithm

scheme, this makes it possible to solve surface integral equation without relying on the conformal mesh and basis functions with inter-element continuity. Various basis functions with different definitions and orders can be chosen flexibly to form a robust surface integral equation solver for multi-scale structures. IEDG algorithm allows local mesh refinement and greatly facilitates wide-band analysis. This algorithm is enhanced by improved enforcement of the transmission conditions for highly resonant structures. Lastly, ground plane capability is incorporated with this IEDG algorithm and good agreements with measurements have been observed. The skeletonalization based direct solver and H-MLFMM can be extended to this novel IEDG to alleviate the multi-scale and low frequency problems encountered in composite targets.

Bibliography

[1] E. Bleszynski, M. Bleszynski, and T. Jaroszewicz. AIM: Adaptive in tegral method for solving large-scale electromagnetic scattering and radiation problems. *Radio Sci.*, 31:1225–1252, 1996.

[2] V. Rokhlin. Diagonal forms of translation operators for the Helmholtz equation in three dimensions. *Appl. Computat. Harmon. Analy.*, 1:82–93, 1993.

[3] S. Velamparambil, W. C. Chew, and J. Song. 10 million unknowns: Is it that big? *IEEE Trans. Antennas Propag.*, 45:43–58, 2003.

[4] L. Gurel and O. Ergul. Fast and accurate solutions of extremely large integral-equation problems discretised with tens of millions of unknowns. *Electron. Lett.*, 9:499–500, 2007.

[5] R.F. Harrington. *Field Computation by Moment Methods*. MacMillan, New York, 1968.

[6] M. Stephason and J.F. Lee. Preconditioned electrical field integral equation using calderon identities and dual loop/star basis functions. *IEEE Trans. Antennas Propag.*, 57:1274–1279, 2009.

[7] R. J. Adams, Y. Xu, X. Xu, S. D. Gedney, and F. X. Canning. Modular fast direct electromagnetic analysis using local-global solution modes. *IEEE Trans. Antennas Propag.*, 56:2427–2441, 2008.

[8] E. Darve. The fast multipole method i: Error analysis and asymptotic complexity. *SIAM J. Numer. Anal.*, 38:98–128, 2000.

[9] M. Nilsson. Stability of the high frequency fast multipole method for helmholtz equation in three dimensions. *BIT Numer. Math.*, 44:773–791, 2004.

[10] J. S. Zhao and W. C. Chew. Three-dimensional multilevel fast multipole algorithm from static to electrodynamic. *Microwave and Optical Technology Letters*, 26:43–48, 2000.

[11] J. S. Zhao and W. C. Chew. Integral equation solution of maxwells equations from zero frequency to microwave frequency. *IEEE Trans.Antennas Propag.*, 48:1635–1645, 2000.

[12] M. Vikram, H. Huang, B. Shanker, and T. Van. A novel wideband fmm for fast integral equation solution of multiscale problems in electromagnetics. *IEEE Trans.Antennas Propag.*, 57:2094–2104, 2009.

[13] J. Huang, V. Rokhlin, and S. Wandzura. Accelerating fast multipole methods for the helmholtz equation at low frequencies. *IEEE Computat. Sci. Eng.*, 5:32–38, 1998.

[14] K. Zhao, M. N. Vouvakis, and J.F. Lee. The adaptive cross-approximation algorithm for accelerated method of moments computations of emc problems. *IEEE Trans. Electromagnetic Compatibility*, 47:763–773, 2005.

[15] J.M.Tamayo, A.Heldring, and J.M.Rius. Multilevel adaptive cross approximation (mlaca). In *Antennas and Propagation Society International Symposium*, 2009.

[16] A. Heldring, J.M. Rius, J.M. Tamayo, J. Parron, and E. Ubeda. Fast direct solution of method of moments linear system. *IEEE Trans.Antennas Propag.*, 55:3220–3228, 2007.

[17] J. Parrn, J. M. Rius, and J. R. Mosig. Application of the multilevel decomposition algorithm to the frequency analysis of large microstrip antenna arrays. *IEEE Trans. Magn.*, 38:721–724, 2002.

[18] J. Shaeffer. Direct solver of electrically large integral equations for problem sizes to 1m unknowns. *IEEE Trans.Antennas Propag.*, 56:2306–2313, 2008.

[19] P.G. Martinsson and V. Rokhlin. A fast direct solver for boundary integral equations in two dimensions. *Journal of Computational Physics*, 205:1–23, 2005.

[20] Z.Peng, X.C.Wang, and J.F.Lee. Integral equation domain decomposition method for solving electromagnetic wave scattering from non-penetrable objects. *IEEE Trans.Antennas Propag.*, 59:3328–3338, 2011.

[21] A. Heldring, J.M. Rius, J.M. Tamayo, J. Parron, and E. Ubeda. Fast direct solution of method of moments linear system. *IEEE Trans. Antennas Propag.*, 55:3220–3228, 2007.

[22] E. Winebrand and A. Boag. Non-uniform grid based fast direct solver for quasi-planar scatterers. In *Proc. of the IEEE AP-S International Symposium*, 2007.

[23] A. Boag. Compression of the method of moments matrices using the non-uniform grid approach. In *International Conference on Electromagnetics in Advanced Applications*, 2007.

[24] W. Chai and D. Jiao. Dense matrix inversion of linear complexity for integral-equation-based large-scale 3-d capacitance extraction. *IEEE Trans. Microw. Theory Tech.*, 59:2404–2421, 2011.

[25] M. Li, C. Li, C.J. Ong, and W. Tang. A novel multilevel matrix compression method for analysis of electromagnetic scattering from pec targets. *IEEE Trans.Antennas Propag.*, 60:1390–1399, 2012.

[26] L. Greengard, D. Gueyffier, P.G. Martinsson, and V. Rokhlin. Fast direct solvers for integral equations in complex three-dimensional domains. *Acta Numerica*, 18:243–275, 2009.

[27] P.G. Martinsson V. Rokhlin H. Cheng, Z. Gimbutas. On the compression of low rank matrices. *SIAM J. Sci. Comput.*, 26:1389–1404, 2005.

[28] S. Seo J.F. Lee M. Vouvakis, K. Zhao. M. vouvakis and k. zhao and s. seo and j.f. lee. *Journal of Computational Physics*, 225:975–994, 2007.

[29] S. M. Rao, D. R. Wilton, and A. W. Glisson. Electromagnetic scattering by surfaces of arbitrary shape. *IEEE Trans.Antennas Propag.*, 3:409–418, 1982.

[30] R.F. Harrington. *Field Computation by Moment Methods*. MacMillan., New York, 1968.

[31] M.Stephason and J.F.Lee. Preconditioned electrical field integral equation using calderon identities and dual loop/star basis functions. *IEEE Trans.Antennas Propag.*, 57:1274–1279, 2009.

[32] W.C.Chew C.C.Lu. A multilevel algorithm for solving a boudary integral equation of wave scattering. *Microwave and Optical Technology Letters*, 7:456–461, 1994.

[33] J.L.Rodriguez, J.M.Taboada, M.G.Araujo, F.O.Basteiro, L.Landesa, and I.G. Tunon. On the use of the singular value decomposition in the fast multiple method. *IEEE Trans.Antennas Propag.*, 56:2325–2334, 2008.

[34] J.G. Wei, Z. Peng, and J.F. Lee. A fast direct matrix solver for surface integral equation methods for electromagnetic wave scattering from non-penetratable targets. *Radio Sci.*, 2012.

[35] J.G. Wei, Z. Peng, and J.F. Lee. A fast direct matrix solver for surface integral equation methods for electromagnetic wave problems in r3. In *The 27th International Review of Progress in Applied Computational Electromagnetics*, 2011.

[36] M. Bebendorf and S. Rjasanow. Adaptive low-rank approximation of collocation matrices. *Computing*, 70:1–24, 2003.

[37] A.Bjorc. Numerics of gram-schmidt orthogonalization. 197:297–316, 1994.

[38] Y.Saad. Gmres: A generalized minimal residual algorithm for solving nonsymmetric linear systems. *J. Sci. Stat. Comp.*, 7:856–869, 1986.

[39] Z. Peng, Kheng-Hwee Lim, and Jin-Fa Lee. Computations of electromagnetic wave scattering from penetrable composite targets using a surface integral equation method with multiple traces. *IEEE Trans.Antennas Propag.*, 61:256–270, 2013.

[40] Wang X.C, Z.Peng, K.H. Lim, and J.F.Lee. Multisolver domain decomposition method for modeling emc effects of multiple antennas on a large air platform. *IEEE Trans. Electromagn. Compat.*, 54:375–388, 2011.

[41] Z. Peng, K.H Lim, and J-F Lee. A discontinuous galerkin surface integral equation method for electromagnetic wave scattering from non-penetrable targets. *IEEE Trans.Antennas Propag.*, to be published.

[42] M.S. Tong and W.C. Chew. A novel meshless scheme for solving surface integral equations with flat integral domains. *IEEE Trans.Antennas Propag.*, 60:3285–3293, 2012.

[43] N. Nair and B. Shanker. Generalized method of moments: A novel discretization technique for integral equations. *IEEE Trans.Antennas Propag.*, 59:2280–2293, 2011.

[44] F. Vipiana and D.R. Wilton. Numerical evaluation via singularity cancellation schemes of near-singular integrals involving the gradient of helmholtz-type potentials. *IEEE Trans.Antennas Propag.*, 61:1255–1265, 2013.

[45] A.G.Polimeridis, J.M.Tamayo, J.M.Rius, and J.R. Moisg. Fast and accurate computation of hypersingular integrals in galerkin surface integral equation formulations via the direct evaluation method. *IEEE Trans.Antennas Propag.*, 59:2329–2340, 2011.

[46] P.W. Fink, D.R. Wilton, and M.A. Khayat. Simple and efficient numerical evaluation of near-hypersingular integrals. *IEEE Trans.Antennas Wireless Lett.*, 7:469–472, 2008.

[47] M.S. Tong and W.C. Chew. Super-hyper singularity treatment for solving 3d electric field integral equations. *Micro. Opt. Technol. Lett.*, 49:1383–1388, 2007.

[48] L.F. Canino, J.J. Ottusch, M.A. Stalzer, J.L. Visher, and S.M. Wandzura. Numerical solution of the helmholtz equation in 2d and 3d using a high-order nystrm discretization. *J. Comput. Phys.*, 146:627–663, 1998.

[49] P. Monk. *Finite Element Methods for Maxwell's Equations*. Clarendon Press, Oxford, 2003.

[50] B. Cockburn, G.E. Karniadakis, and C.W. Shu. *Discontinuous Galerkin Methods: Theory, Computation and Applications*. Springer-Verlag Telos, Germany, 2000.

[51] J. Hesthaven and T. Warburton. *Nodal Discontinuous Galerkin Methods*. Springer-Verlag, New York, 2008.

[52] A. Buffa, H. Paul, and P. Ilaria. Discontinuous galerkin computation of the maxwell eigenvalues on simplicial meshes. *J. Comput. Appl. Math.*, 204:317–333, 2007.

[53] H. Paul, P. Ilaria, and D. Schtzau. An a posteriori error indicator for discontinuous galerkin discretizations of h (curl)-elliptic partial differential equations. *IMA J. Numer. Anal*, 27:122–150, 2007.

[54] P. Monk. *Finite Element Methods for Maxwell's Equation*. Numerical Mathematics and Scientific Computation, New York, 2003.

[55] F.P. Andriulli, K.Cools, H.Bagci, F.Olyslager, A. Buffa, S. Christiansen, and E. Michielssen. A multiplicative calderon preconditioner for the electric field integral equation. *IEEE Trans.Antennas Propag.*, 56:2398–2412, 2008.

[56] M.Stephanson and J.F. Lee. Preconditioned electric field integral equation using calderon identities and dual loop/star basis functions. *IEEE Trans.Antennas Propag.*, 57:1274 – 1279, 2009.

[57] F.L. Teixeira. Geometric aspects of the simplicial discretization of maxwell's equations. *Prog. Electromagn. Res.*, 32:171–188, 2001.

[58] F.L. Teixeira and W.C. Chew. "lattice electromagnetic theory from a topological viewpoint. *J. Math Phys.*, 40:169–187, 1999.

[59] X.Q. Sheng, J.M. Jin, J.M. Song, W.C. Chew, and Cai-Cheng Lu. Solution of combined-field integral equation using multilevel fast multipole algorithm for scattering by homogeneous bodies. *IEEE Trans.Antennas Propag.*, 46:1718–1726, 1998.

[60] Z.Peng, V.Rawat, and J.F.Lee. One way domain decomposition method with second order transmission conditions for solving electromagnetic wave problems. *J. Comput. Phys.*, 229:1181–1197, 2010.

[61] S.V.Polstyanko and J.F. Lee. H1(curl) tangential vector finite element method for modeling anisotropic optical fibers. *J. Lightwave Technol.*, 13:2290 – 2295, 1995.